Coupling of an Immersed Boundary Finite Volume Solver with an Aerothermodynamic Library for Atmospheric Entry Applications

MSc Thesis

A. O. Başkaya

Technische Universiteit Delft

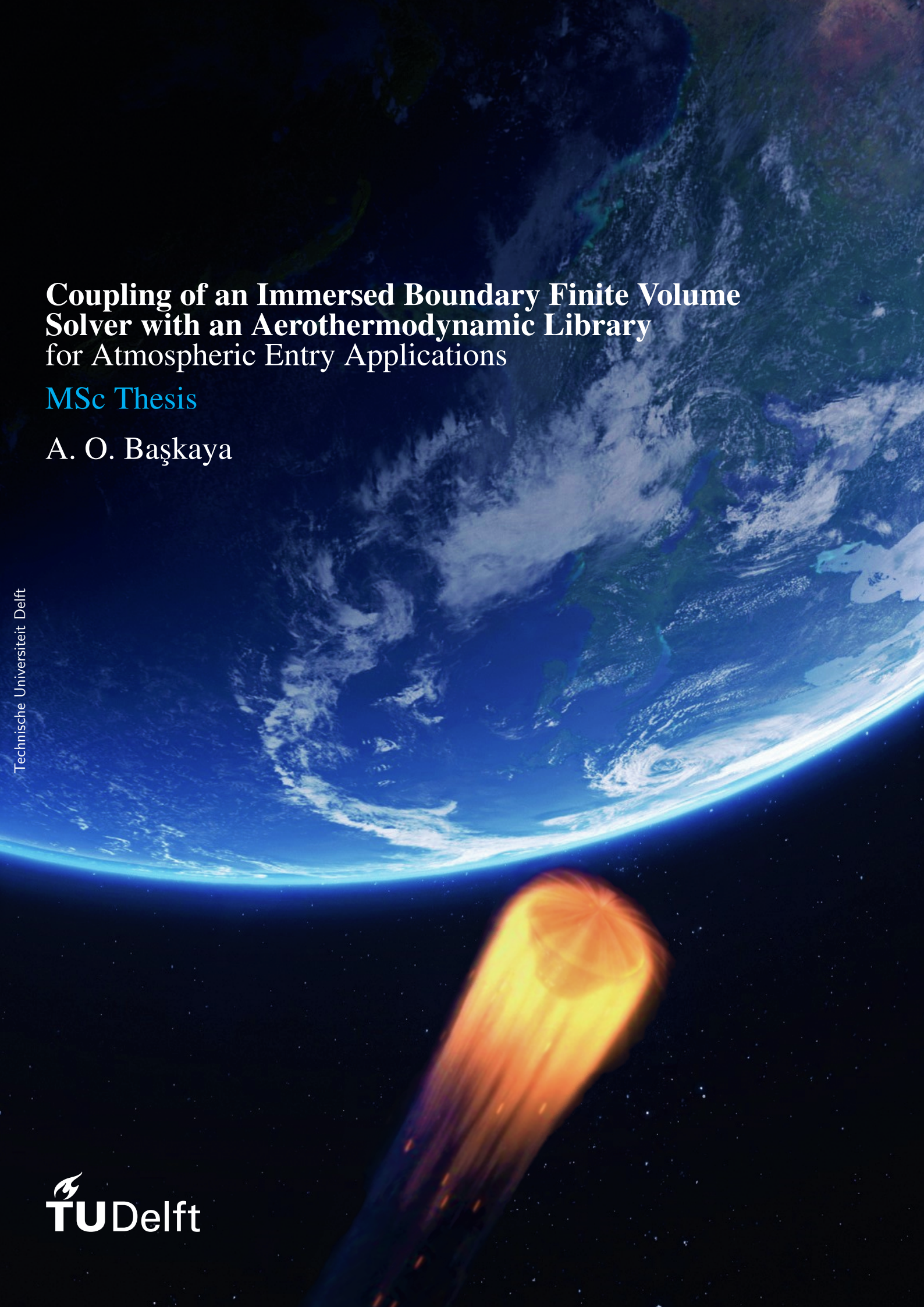

TU Delft

Coupling of an Immersed Boundary Finite Volume Solver with an Aerothermodynamic Library for Atmospheric Entry Applications

MSc Thesis

by

A. O. Başkaya

to obtain the degree of Master of Science
at the Delft University of Technology,
to be defended publicly on Friday September 25, 2020 at 14:00.

Student number:	4893271	
Project duration:	January 20, 2020 – September 25, 2020	
Thesis committee:	Prof. Dr. S. Hickel,	TU Delft, supervisor
	Prof. Dr. T. Magin,	VKI, supervisor
	Prof. Dr. G. Eitelberg,	TU Delft
	Dr. ir. B. W. van Oudheusden,	TU Delft
	Dr. ir. L. Walpot,	ESA

An electronic version of this thesis is available at http://repository.tudelft.nl/.

TU Delft

Cover image courtesy of Domenico Sellaro and NASA.

I'm burning through the sky, yeah,
Two hundred degrees, that's why they call me Mister Fahrenheit,
I'm travelling at the speed of light,
I wanna make a supersonic man out of you.

—Freddie Mercury, *Don't Stop Me Now*

Abstract

Atmospheric entry is a crucial phase in planetary exploration missions. During entry, the vehicle experiences severe heating at hypersonic speeds. To ensure the survival of the payload, this heating needs to be mitigated using thermal protection systems. Ablative shielding materials dissipate the incoming heat largely by surface reactions leading to material decomposition. Accurate simulations of this flow environment are critical for the efficient design of spacecraft. The main difficulties in this analysis are due to strong shock waves and thermochemical nonequilibrium in the flow field, giving rise to chemical reactions and the excitation of the internal energy modes of the fluid particles. Under these conditions, an accurate assessment of the flow field requires detailed models for evaluating the physicochemical properties of the reacting fluid, and its interaction with the heat shield at the vehicle surface.

This thesis considered the coupling of a high-fidelity flow solver with an aerothermodynamic library designed specifically for atmospheric entry applications. The flow solver is a Cartesian grid immersed boundary finite volume code capable of performing high-order accurate simulations. The coupling procedure with the external library involved four modules to extend the applicability of the flow solver to atmospheric entry flight regimes. The first one provides an accurate set of thermodynamic properties acquired from a tailored database for relevant species. The second module supplies transport properties through a rigorous calculation respecting kinetic theory as opposed to simplified models. The third module deals with the finite-rate chemical reactions occurring in the flow. The last module enables the consideration of catalytic and ablative surface reactions as boundary conditions for the flow solver. Thermal nonequilibrium is implemented to consider two temperatures for the conservation of translational-rotational and the vibrational-electronic energies. Gas-surface interactions are implemented for the first time in a conservative immersed interface method. Various test cases have been simulated for the verification and validation of each of these implementations. Good agreement with reference results are obtained. The increase in the computational cost is justified by the significant improvements in the results and the wide range of conditions made accessible for investigation. A novel framework is established, with which flow simulations that are state-of-the-art both in terms of numerical accuracy and fluid physicochemistry can be performed.

Acknowledgements

Many months have passed since I began this project at TU Delft in collaboration with VKI. Throughout that time, I was fortunate to have the guidance of some great individuals without whom this thesis would not have become what it is today. First and foremost, I would like to thank Prof. Stefan Hickel for his supervision over the project, and also for his interest and belief in its potential. I sincerely appreciate his trust in me, which allowed me to reach out and fall at times, to learn to rise back up. I would like to thank Prof. Thierry Magin for his constructively critical review of my work and for the insight he has bestowed upon me regarding topics often beyond the expertise of common aerodynamicists. As with his initial proposal for this project, I am truly grateful for all his support in helping me shape my academic career. I could not thank Dr. Alessandro Turchi enough for all his thoughtful suggestions and erudite advice, not just on this study, but about the nature of research and academics itself. I would like to send him my sincerest gratitude as, even at times of scholastic despair, he has helped me realize the reasons to be proud of my work.

From Delft, I would like to thank Marc Cruellas Bordes for his friendship, which serendipitously lead to the inception of this project. Cheers to my most tenaciously resilient teammate Orçun for all that we have went through over these years. And to my friend and fellow classmate through this journey, Haris Shahzad, I cannot thank you enough for being the good listener and the kind soul you are.

As for the ever so welcoming VKI family, I would like to thank my friend and colleague Michele Capriati for sharing his knowledge and experience with me. I also fondly recall my sporadic, yet stimulating discussions with Koen Devesse. I thank my utterly frolic flatmates Anıl and Deniz, and my dearest landlady Claire for keeping me sane during these challenging days and nights, in the midst of a pandemic.

Lastly, but with utmost affection, I am eternally grateful for the countless encouragements and good wishes I have received from my longest friends, family and loved ones. I apologize from you, for all the times you needed me on Earth, while I was busy burning up in the atmosphere.

I dedicate this thesis to the warm memory of my grandfather. It could not have been done without you, but it is done without you. *Dedeciğim için kuşlar şakısın.*

A. O. Başkaya
Brussels, September 2020

Contents

Nomenclature

Acronyms

CEA	Chemical Equilibrium with Applications
CFD	Computational Fluid Dynamics
DES	Detached-Eddy Simulation
DLR	German Aerospace Center
DNS	Direct Numerical Simulation
DPLR	Data-Parallel Line Relaxation
DSMC	Direct Simulation Monte Carlo
EDL	Entry, Descent and Landing
ESA	European Space Agency
GSI	Gas-Surface Interactions
HLLC	Harten Lax and van Leer Contact
LES	Large-Eddy Simulation
LST	Linear Stability Theory
MSL	Mars Science Laboratory
MUTATION++	MUlticomponent Thermodynamics And Transport properties for IONized gases in C++
NASA	National Aeronautics and Space Administration
ODE	Ordinary Differential Equation
PANT	Passive Nose Tip Technology
PICA	Phenolic Impregnated Carbon Ablator
RANS	Reynolds-Averaged Navier-Stokes
RRHO	Rigid-Rotor Harmonic-Oscillator
STL	STereoLithography / Standard Tessellation Language
STS	State-to-State
TPS	Thermal Protection System
VKI	von Karman Institute for Fluid Dynamics
WENO	Weighted Essentially Non-Oscillatory

Roman Symbols

a	speed of sound	$[\,\mathrm{m/s}\,]$
c_p	specific heat at constant pressure	$[\,\mathrm{J/kgK}\,]$
c_v	specific heat at constant volume	$[\,\mathrm{J/kgK}\,]$
D_{im}	average diffusion coefficient	$[\,\mathrm{m^2/s}\,]$
e	specific energy	$[\,\mathrm{J/kg}\,]$
E	total energy	$[\,\mathrm{J/kg}\,]$

$\mathbb{F}$	force	$[\,\mathrm{N}\,]$
g	Gibbs free energy	$[\,\mathrm{J/kg}\,]$
h	specific enthalpy	$[\,\mathrm{J/kg}\,]$
h_P	Planck's constant	$[\,\mathrm{m^2kg/s}\,]$
$\mathbf{J}_i$	diffusive flux	$[\,\mathrm{kg/m^2s}\,]$
k_B	Boltzmann constant	$[\,\mathrm{J/K}\,]$
$\dot{m}$	mass flux	$[\,\mathrm{kg/m^2s}\,]$
M	Mach number	$[\,-\,]$
M	molar mass	$[\,\mathrm{kg/mol}\,]$
n	number density	$[\,\mathrm{m^{-3}}\,]$
$\mathbf{n}$	surface normal vector	$[\,-\,]$
N_A	Avogadro number	$[\,\mathrm{mol^{-1}}\,]$
p	pressure	$[\,\mathrm{Pa}\,]$
$\mathbf{q}$	heat flux	$[\,\mathrm{J/m^2s}\,]$
r	distance from wall	$[\,\mathrm{m}\,]$
$\hat{r}$	distance between particles	$[\,\mathrm{m}\,]$
R	mixture gas constant	$[\,\mathrm{J/kg\ K}\,]$
$\mathcal{R}$	universal gas constant	$[\,\mathrm{J/mol\ K}\,]$
s	specific entropy	$[\,\mathrm{J/kgK}\,]$
$\dot{s}$	recession rate	$[\,\mathrm{m/s}\,]$
t	time	$[\,\mathrm{s}\,]$
T	temperature	$[\,\mathrm{K}\,]$
$\mathbf{u}$	velocity	$[\,\mathrm{m/s}\,]$
v	surface normal speed	$[\,\mathrm{m/s}\,]$
V	volume	$[\,\mathrm{m^3}\,]$
$\mathcal{V}$	diffusion velocity	$[\,\mathrm{m/s}\,]$
x	mole fraction	$[\,-\,]$
y	mass fraction	$[\,-\,]$

Greek Symbols

ϵ_s	emissivity	$[\,-\,]$
γ	ratio of specific heats	$[\,-\,]$
λ	thermal conductivity	$[\,\mathrm{W/mK}\,]$
μ	dynamic (shear) viscosity	$[\,\mathrm{Pa\,s}\,]$
ν	stoichiometric coefficient	$[\,-\,]$
$\dot{\omega}$	chemical source term	$[\,\mathrm{kg/m^3s}\,]$
$\dot{\Omega}$	source term for energy exchange between modes	$[\,\mathrm{kg/m^3s}\,]$
ρ	density	$[\,\mathrm{kg/m^3}\,]$
σ	Stefan-Boltzmann constant	$[\,\mathrm{W/m^{-2}K^{-4}}\,]$
$\overline{\overline{\boldsymbol{\tau}}}$	stress tensor	$[\,\mathrm{Pa}\,]$

Sub- and Superscripts

c	charred material
†	transpose
E	electronic mode
eq	flow in chemical equilibrium
fr	chemically frozen flow
g	pyrolysis
i	species index
I	internal modes
r	reaction index
R	rotational mode
s	solid
T	translational mode
v	virgin material
V	vibrational mode
w	wall

List of Figures

List of Tables

1 Introduction

Humanity has always been driven by the urge to discover what is unknown. For millennia, the challenge of exploring the uncharted vastness of the cosmos stood mysteriously out of reach. The unrelenting curiosity of the brightest minds of our species brought forth the dawn of the space age, and with it, we set sail on our most daunting endeavor yet. In this expedition, development of innovative technological advancements is pivotal. To that end, this thesis ultimately aims to contribute to the understanding of atmospheric entry phenomena for future space exploration missions.

1.1. Space Exploration Challenges

The desire for exploring space is stimulated by the ceaseless curiosity of humankind. Among its many benefits to the progress of our civilization, discoveries made in this manner help us to understand the nature of our solar system and beyond, as we continue our search for extraterrestrial minerals, organisms, and habitable environments. Space exploration missions have many different scientific objectives, such as reconnaissance and environmental characterization. Some of these objectives can be accomplished by flyby or orbiter missions. However, sample retrieval or human crew transportation is essential for a more detailed planetary exploration. These types of missions are enabled by the use of probes or spacecraft. In these missions, the vehicle goes through an entry, descent and landing (EDL) sequence, as it arrives at its destination, whether it is back on Earth or on another celestial body.

On 12$^{\text{th}}$ April 1961, Vostok 1 made the first crewed spaceflight and re-entry into Earth's atmosphere. Nearly two decades later, Space Shuttle missions demonstrated the EDL sequence as they carried crew into orbit and back. During an ordinary return in one of these missions, the spacecraft attained speeds up to about 7.8 km/s, and while doing so, it experienced convective and radiative heating, due to the strong bow shock forming upstream [3]. Convective heating is due to conduction and the chemical reactions of the particles that collide with the vehicle surface. Radiative heating refers to the energy transfer by radiation emitted from these excited particles. To mitigate the heat from penetrating into the hull of the spacecraft, thermal protection systems (TPS) were installed around the vehicle [36]. Among the two types of TPS, Space Shuttle employed reusable TPS in-line with its goals of reutilization in multiple missions. Reusable heat shields are commonly made of silicon-carbide materials, which host high emissivities at high temperatures, enabling them to effectively re-radiate energy from the heated surface to the ambient flow. However, this type of TPS can only endure relatively low speed entries, often experienced following suborbital flights. For applications beyond these limits, such as for the Apollo missions, ablative TPS are selected instead. Ablative heat shields are constructed to absorb the heat by means of physicochemical reactions leading to material decomposition and mass loss. Since an ablative heat shield is consumed during entry, it is intended for a single use. Application ranges of these TPS and associated onset of high temperature effects are indicated for certain representative vehicles in Fig. (1.1).

On 7 December 1995, the Galileo probe descended into the Jovian atmosphere at a velocity of 47.4 km/s. To prevent the on-board measurement systems from overheating (i.e. reaching above 70-80 °C), the probe had a fully dense carbon-phenolic forebody heat shield. During entry, ablation sensors installed inside the heat shield measured the degradation of the TPS material as shown in Fig. (1.2).

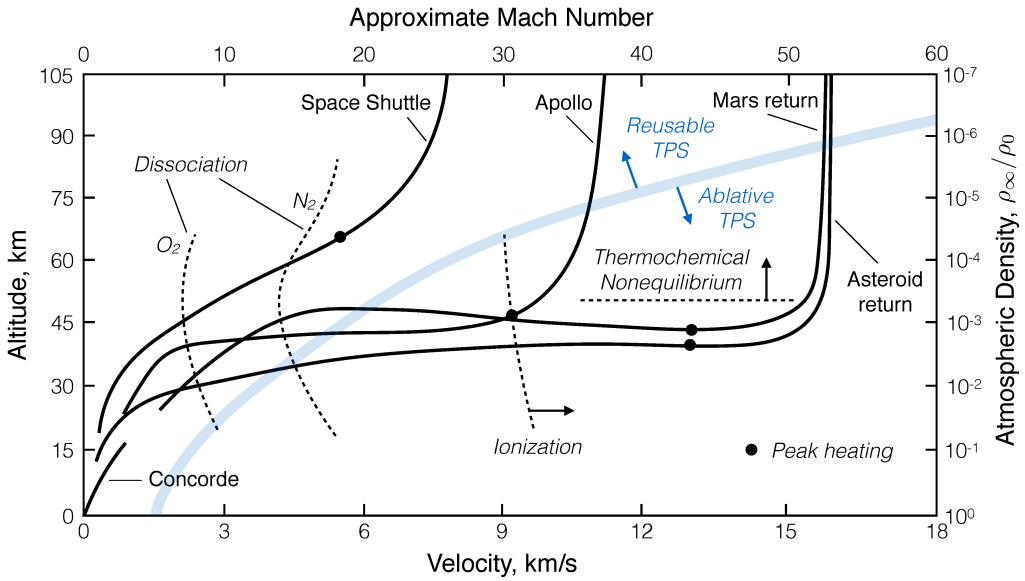

Figure 1.1: Re-entry trajectories for notable vehicles through flight regimes of Earth's atmosphere [117].

It can be seen that the designed TPS thickness underestimated the heat load along the shoulder, and overestimated it at the stagnation point of the probe. The penetration at the shoulder was critical and almost lead to the premature demise of the probe. The surplus material mass at the stagnation point increased the fraction of vehicle mass devoted to the TPS.

The amounts of mass fractions occupied by the TPS of some notable past entry vehicles are compiled in Fig. (1.3). It can be concurred that a significant fraction of mass is dedicated to the protection of entry vehicles, as the heat load increases. Reducing the amount of mass occupied by the heat shield is crucial in allowing lighter launch weights and more room for scientific payloads. So much so that TPS selection has been a mission enabler in the case of the Stardust spacecraft, which made a close flyby of the Wild-2 comet in 2004 [68]. As the sample return capsule came back with the cometary findings, it performed the fastest unmanned Earth entry at 12.9 km/s, and survived the landing. The capsule was protected by the lightweight phenolic impregnated carbon ablator (PICA), which only had a density of around 240 kg/m^3. PICA-like materials have continued being developed, such as ASTERM by Astrium for the European Space Agency (ESA) and PICA-X by the National Aeronautics and Space Administration (NASA) for Space-X.

During the last few years, exploration efforts continued to progress with multiple projects by ESA and NASA, targeting the Moon, Mars and return to Earth. Early in 2015, ESA's Intermediate eXperimental Vehicle (IXV) successfully demonstrated its EDL capabilities by an autonomous low orbit entry. In 2016, a Mars landing attempt was made by the Schiaparelli EDL demonstrator within the ExoMars project of ESA, which gathered valuable data [41], even though it suffered problems related to its on-board computer and crashed on the surface. On a smaller scale, yet with great ambitions, QARMAN (Qubesat for Aerothermodynamic Research and Measurements on AblatioN) has been extensively developed by the von Karman Institute for Fluid Dynamics (VKI) for performing re-entry measurements within the cubesat platform [112], and it has been successfully deployed to orbit from the International Space Station (ISS) on February 19th, 2020.

As future missions gradually begin to aim towards sending humans to the Moon or Mars to construct more long-lasting settlements, vehicle size is bound to increase to accommodate larger cargo capacities and life support facilities that enable crewed space flights. Larger vehicle sizes present a plethora of challenges due to more extreme heating conditions, heavier TPS, boundary layer transition and turbulent heating augmentation. The requirements become even more demanding for novel entry systems, hosting inflatable [33, 58] or deployable [22, 131] heat shields. A profound understanding of atmospheric entry phenomena is indispensable in the design of these vehicles.

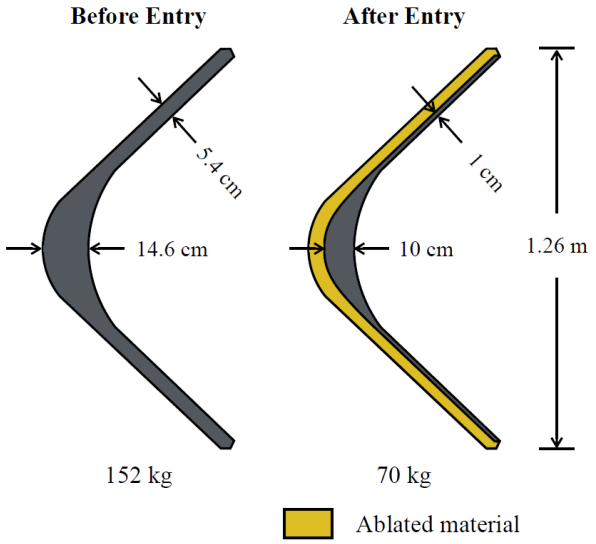

Figure 1.2: Amount of surface recession according to the ablation sensors on the Galileo probe's heat shield [117].

1.2. Atmospheric Entry Phenomena

The challenges in the prediction of TPS sizing present in historical entry missions is due to several complexities in its analysis. Most of these issues were identified by Gnoffo [46] at the turn of the century, yet many of them still persist today with large uncertainties in their assessment. Principally, hypersonic speeds are encountered ubiquitously during atmospheric entry. These flight regimes are classified to speeds of several times the speed of sound, usually above Mach 5, resulting in strong shocks sufficient enough to envelope the vehicle in high-temperature effects, which are discussed in this section. First hypersonic flight demonstrations go back more than seven decades ago, where the German A4–V-2 rocket reached velocities up to 1.6 km/s. Following this, the Bumper program in the United States demonstrated a multi-stage rocket launch on February 24$^{\text{th}}$, 1949. After the completion of the first stage, hosting a recovered German A4–V-2 rocket from the second world war, the second stage went on to reach a speed of 2.3 km/s at an altitude of 390 km [3]. These became the first human-made objects to achieve hypersonic flight, and since then, humankind has been in a "relentless pursuit" to understand the fascinating nature of this flight regime [69].

As it gradually became clear at the time, all hypersonic design processes were dominated by severe aerodynamic heating. Throughout the evolution of aerodynamic design, more streamlined geometries were preferred to minimize drag. However, when applied to hypersonic flight regimes, this idea resulted in insurmountable surface temperatures due to the attached shock wave and boundary layer interaction. The blunt body concept proposed by Allen [3] alleviated this issue by detaching the shock wave away from the vehicle, allowing a thicker shock layer for the flow to cool down before reaching the boundary layer. This design was rapidly adapted to all future entry missions.

The shock standoff distance is often a robust indicator of the characteristics of a blunt vehicle. Gnoffo et al. [47] have shown the effects of Mach number and chemical reactions on stability. Essentially, higher reaction rates release more species into the flow, and increase the density jump across the bow shock. This causes the shock to lie closer to the body. As the standoff distance decreases, the location of the line where sonic conditions are achieved and the pressure distribution along the surface begin to change [18]. These effects influence the stability of the vehicle.

Figure 1.4 presents a general overview of various entry phenomena occurring beyond the shock wave. In the relaxation region downstream of the shock, the highly compressed and energized flow can reach temperatures of thousands of degrees, sufficient to excite the internal states of the gaseous species, dissociate or even ionize the gas. Air at 1 atm pressure becomes vibrationally excited around 800 K, then O_2 begins to dissociate at 2500 K and completely dissociates around 4000 K, as N_2 begins to dissociate. N_2 is almost fully dissociated at 9000 K, then further collisional excitation leads to ionization of these atomic species and the formation of plasma. These new species are said to be in

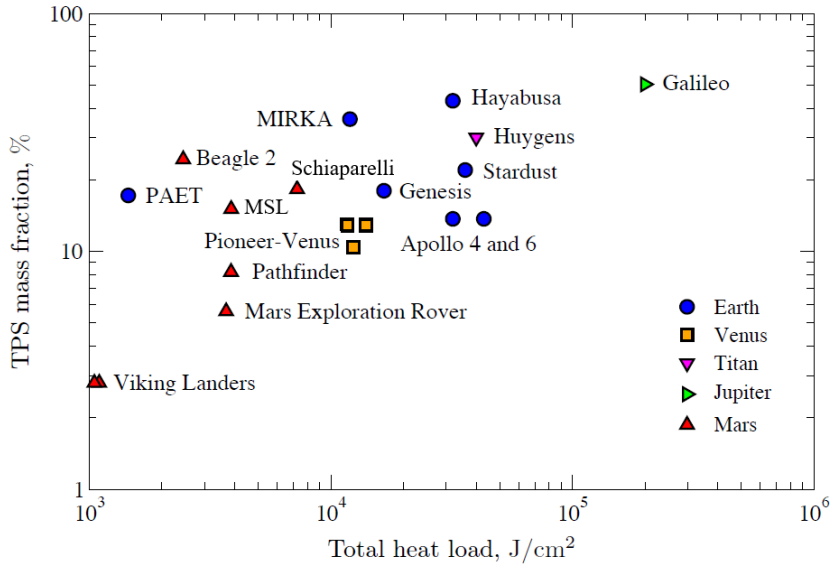

Figure 1.3: Percentage of vehicle mass dedicated to TPS for several missions. Compiled initially by Scoggins [117] from the guide of Davies and Arcadi [32]. Updated for MSL [39, 42] and Schiaparelli [109] missions.

thermal and chemical nonequilibrium, that is, the species are thermally and chemically disturbed from their states of equilibrium. When the internal energy modes of an atom or a molecule, such as rotational, vibrational, or electronic modes are excited in addition to the translational energy mode at high enthalpy conditions, thermal nonequilibrium may occur. This leads to several temperature definitions in the gas, corresponding to distinct thermal baths for internal degrees of freedom. Chemical nonequilibrium refers to a state where forward and backward reaction rates are not balanced, so that the concentrations of reactants and products differ from their equilibrium values. In lower speed applications, thermochemical equilibrium conditions prevail as the characteristic time in which the chemical reactions occur is much quicker than the characteristic time it takes for a flow element to traverse the flow field. However, these two time scales are on the same order when the flow travels at hypersonic speeds. Thus, after a strong bow shock, the flow is in thermochemical nonequilibrium. For a blunt body, the nonequilibrium flow accelerated further at the shoulder of the vehicle may reach a state of frozen flow, where the chemical reaction rates are practically zero. As the flow travels downstream, equilibrium is achieved at freestream conditions. These phenomena are referred to as high-temperature effects, and they are studied under the field of aerothermodynamics. At these high temperatures, the thermodynamic properties of the fluid, for example the specific heats, are not constant and may depend on temperature, pressure, and the chemical composition of the mixture. Accurate assessment of these effects is crucial in determining the flow properties.

As the high temperature flow approaches the surface of the vehicle, dissociated species from the shock layer begin to interact with the surface material. This is investigated under the study of gas-surface interactions (GSI). Within the chemically reacting boundary layer, the heat flux onto the vehicle not only depends on conduction due to thermal gradients, but also on diffusion of species. Atoms impinging on the surface react with each other or with the surface species to undergo recombination reactions, which are exothermic in nature and release further heat to the surrounding. At re-entry temperatures, the surface acts as a catalyst for the ambient species, and accelerates the chemical process by reducing the overall potential energy level that must be reached to surpass the activation energy barrier imposed by the governing Arrhenius relations. Particularly in Earth reentries, ascribed to the abundance of nitrogen and oxygen in the Earth's atmosphere, the common molecules that arise due to catalytic recombination reactions are N_2, O_2 and NO.

The chemical reactions occurring at the surface between the gas phase species and the solid phase material, depend on the characteristics of the material, and differs for reusable and ablative TPS. For re-usable TPS materials, such as ceramics, this heterogeneous catalysis is the main form of heat transfer towards the vehicle. At higher re-entry speeds, corresponding to temperatures easily surpassing 2000 K,

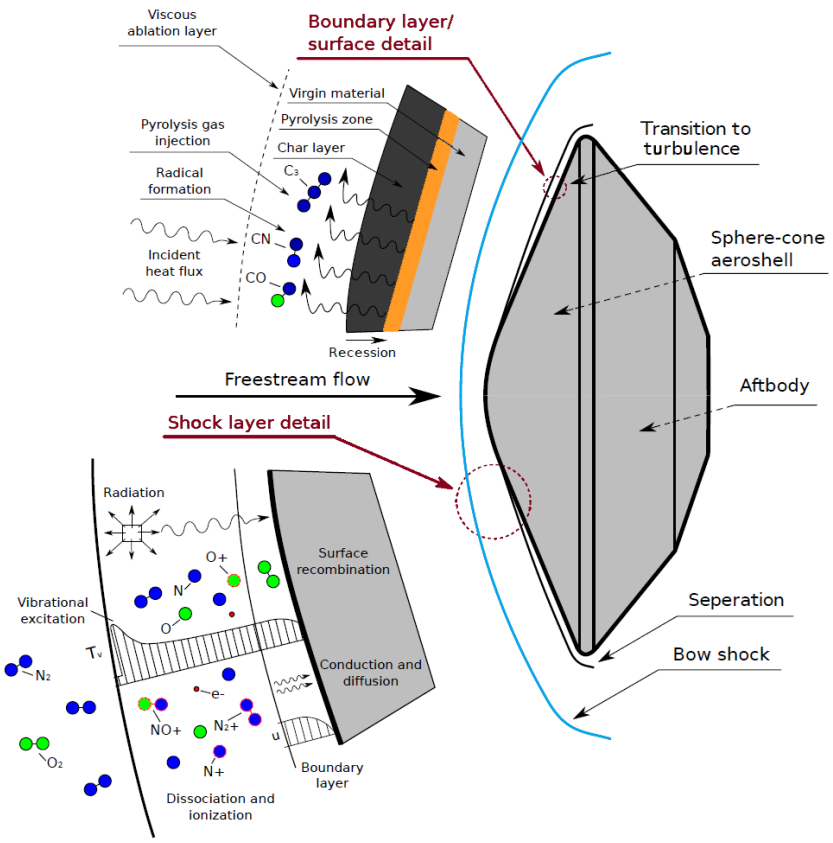

Figure 1.4: Illustration indicating common atmospheric entry phenomena. Adapted from Potter [110].

re-usable TPS materials become insufficient, and ablative materials are chosen instead. These usually carbon-based materials experience ablative surface reactions characterized by oxidation, nitridation, and sublimation, which transform the thermal load into mass loss, by means of chemical and physical decomposition. Initially, the pre-entry TPS is in its *virgin* form prior to experiencing ablation. Charring ablative materials which are impregnated with a resin, such as carbon-phenolic, undergo in-depth decomposition caused by the presence of heat moving deeper into the virgin material to trigger pyrolysis reactions. This process releases gaseous species into the ambient flow, while leaving some amount of carbon as residue, creating the so-called pyrolysis and char layers within the material. Furthermore, when a cork-phenolic TPS [108, 112] is considered, the pyrolysis gas composition becomes even more complex, since the cork itself pyrolyzes in addition to the resin, introducing additional species into the boundary layer. Modeling pyrolysis is crucial as the additional species introduced into the flow inhibit the participation of ambient species in surface reactions, which lowers the convective heat flux [2]. Additionally, the endothermic nature of these reactions and the blowing due to the outgassing of these pyrolysis products further aid in mitigating the heat load.

Ablation permits the extraction of species from the TPS material, and in turn causes surface erosion and recession. The recessing surface continuously depletes during entry, and alters the aerodynamic shape of the vehicle. Under severe loadings, mechanical degradation in the form of spallation may even occur, where pieces of material break off and eject downstream. Tracking the amount of recession is critical not only for estimating the thickness of the TPS, but also to predict its unsteady behavior during flight as it can lead to abrupt changes in aerodynamic characteristics, and may induce transition to turbulence.

As with many applications in aerospace, analyzing the effect of turbulence is decisive in entry flight. As the entry vehicle continues its descent through the atmosphere, it maintains significant speeds, while the ambient air becomes denser, leading to Reynolds numbers on the order of several millions. Turbulent flows are naturally encountered in the wake of entry vehicles and around the shoulder of the leading cone before reaching forward gradually. Laminar to turbulent transition in the attached boundary layer can be triggered due to surface irregularities such as roughness or shape change in the

case of ablative TPS. Since the flow properties around the surface are not uniform, recession of the material does not necessarily preserve the initial geometry. As the flow becomes turbulent due to these variations, heat transfer and consequently the ablation rate is enhanced. Larger heat and mass transfer in turn modifies the shape again, constructing a cycle of cause and effect, which persists throughout the entry sequence [132]. Investigation of this phenomenon dates back to the Passive Nose Tip Technology (PANT) program [136] conducted in 1975 by Aerotherm, where the impact of irregular shape changes due to nonuniform surface recession on transition and shock locations is discussed.

Among other factors present also in lower speed flights, such as freestream disturbances, transition in entry flows is additionally influenced by the surface state, chemical reactions, and blowing of pyrolysis gases. As concurred from experiments conducted on a slender cone subjected to high enthalpy flow of air, nitrogen and carbon dioxide separately, carbon dioxide bolstered a larger transition Reynolds number [43]. This delay in transition has been associated with the vibrational relaxation of CO_2, which dampens the growth of instabilities in the flow. This effect may become important in entry missions, where the atmosphere composition is primarily comprised of CO_2, as in the case of Mars. As for the influence of chemistry, Miró-Miró et al. [86] suggests that chemical reactions affect transition in two competing ways. Including the reactions in the simulations was shown to stabilize the flow. In contrast, the cooling due to chemical reactions in the boundary layer lowers the viscosity and destabilizes the flow. This is further supported by Candler [18], where it is stated that exothermic reactions increase the rate of instability growth, while the endothermic reactions have the opposite effect. Consequently, Knisely and Zhong [64] have suggested that conventional transition prediction tools, such as the e^n method, may lead to inaccurate results under thermochemical nonequilibrium. In a recent comprehensive review [87], transition location was identified to be highly sensitive to the modeling of transport properties. Due to simplified approaches used for modeling diffusion and viscosity with the underlying outdated collisional data, the transition location was estimated approximately 38% earlier than anticipated. These results help to demonstrate the major role of physicochemical phenomena in flow stability.

A more recent example highlighting the impact of transition to turbulence is the Mars Science Laboratory (MSL) mission's Curiosity rover entry, which landed on the surface of Mars on August 6^{th}, 2012. It hosted a heat shield constructed from a tiled PICA arrangement specifically designed for this expedition. The heat shield was instrumented with thermocouples and ablation sensors to track its behavior. Comparison of flight data and the design predictions are shown in Fig. (1.5) for two measurement points. It can be clearly seen from the peak temperatures that the initial predictions overestimated the leeside region and underestimated the stagnation region. An initial assessment by Bose et al. [13], suspects that the discrepancies between the measurements and the predictions are due to several assumptions regarding the onset of turbulence. First, chemical equilibrium assumption imposing full recombination at the surface lead to an overestimation of recession. This was accompanied by the assumption of a fully turbulent flow over the heat shield. In reality, transition to turbulence was occurring, as it was later identified from the sudden increases in the rates of temperature rise. It is estimated that various uncertainties similar to these lead to around 40% overestimation of MSL's TPS thickness [13]. The design concerns are not limited to these considerations, as Schneider [115] has determined from his review of historical missions, the two main design concerns regarding transition are related to the heat shield face and the reattachment of the shear layer on the afterbody. The former concern endangers the back side of the vehicle, which is often only mildly insulated for mass efficiency. Hence, accurate estimation of transition and the proceeding turbulent heating is of great importance for the efficient design, aerodynamic performance and stability of an entry vehicle.

Predicting transition in hypersonic flows is a formidable task as foundations of turbulence theory are mostly established on incompressible flows, where only the velocity fluctuations are considered. This approach remains valid even for certain supersonic flows, but becomes insufficient at hypersonic speeds, when fluctuations in density become significant. Fundamental studies on linear stability of boundary layers have been performed by Mack [70] in 1984, and it remains an active research topic today [64, 87, 90]. An elaborate analysis on the onset of transition and boundary layer stability is beyond the scope of this thesis, yet the review given here is motivated by the possible extensions of this work in future studies.

At very high entry speeds, radiation becomes a significant medium of heat emanating both towards and away from the body. A proper assessment of radiation generally requires the use of a separate radiation tool. In this thesis, such a module is not considered. It is suggested that radiative heating is negligible below entry speeds of roughly 12 km/s [36], however this is not always true, for example for

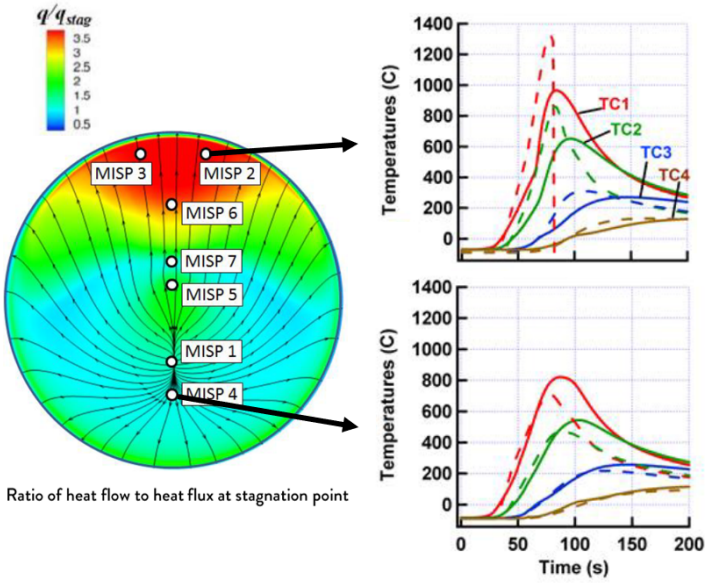

Figure 1.5: Comparison of flight data (solid lines) with design predictions (dashed lines). MISP stands for the integrated sensor plugs and TCs are the thermocouples. Adapted from Bose et al. [13].

the Apollo command module, as this limit naturally depends on the vehicle size, entry trajectory, and atmospheric conditions. Depending on the planet's atmosphere, different species may play an important role, as it was observed in the entry of the Huygens probe into Titan's atmosphere, on January 14$^{\text{th}}$, 2005. A large presence of CN, a highly radiative species, was detected in the shock layer. For this case, Magin et al. [73] have pointed out that assuming thermal equilibrium overestimates the radiative heating by 2 to 15 times of that computed by an accurate nonequilibrium model. On the other hand, during the entry of Stardust, at a relevant trajectory point studied by Martin et al. [80], total radiative heat flux was merely 1% of convective heat flux. Although Stardust's entry speed was higher than Apollo's in this case, it had much smaller capsule dimensions. Hence, case studies must assess whether convective or radiative heating is dominant, or of the same order.

The preceding complexities in the entry environment around the vehicle pose difficulties in its analysis. Experimental techniques are indispensable for validation purposes, however, ground testing is often inadequate in replicating high-enthalpy flows for large durations [9, 20] and maintaining low freestream turbulence levels typical of hypersonic flight [13, 111]. Hence, computational fluid dynamics (CFD) simulations are of the essence. These simulations aid in accurate sizing of the TPS to prevent erroneous estimations that might lead to catastrophic failures [45] and to avoid over-conservative designs with large safety margins.

1.3. State-of-the-Art Aerothermodynamic CFD Tools

The computational tools available today that are capable of exercising the aforementioned phenomena to some degree of comprehensiveness, have their origins in the heritage formulations developed in the 80s [100] and are often restricted by limitations in favor of efficiency or robustness. Commercially available codes generally lack the fidelity of specialized codes due to fundamental differences in their infrastructure [75]. In this section, finite-volume based state-of-the-art academic aerothermodynamic CFD tools and some extensively validated space agency codes will be reviewed.

The first tool considered here is the well-established Data-Parallel Line Relaxation (DPLR) code developed at the NASA Ames Research Center [138]. DPLR is a fully three-dimensional third-order accurate solver operating on structured grids with support for parallelization. It incorporates finite-rate chemistry reactions, thermochemical nonequilibrium, accurate transport properties and ionized mixtures. It also provides surface boundary conditions enabling loose coupling with material response solvers. Data-parallel line relaxation is essentially a method, developed by Wright, Candler, and Bose [137], for the solution of the linear system of equations constructed by an implicit time integration scheme. It considers a line-relaxation problem in which the solution is computed along normal lines

away from the surface through a series of relaxation steps. A low dissipation Steger-Warming flux-splitting approach for the convective terms and central differencing for the diffusive terms is available. This method was shown to be especially robust and efficient in high Reynolds number flows with highly stretched grids [20]. A recent example by Wise et al. [135] considers the Mars 2020 entry capsule in an environment simulated by DPLR coupled with a radiation code. A super-catalytic surface boundary condition assuming full recombination at the surface is employed. This assumption forgoes establishing a mass balance to take into account the diffusion of species at the surface, and generally yields an unnaturally high surface heat flux. The forebody is modeled as fully turbulent with the algebraic Baldwin-Lomax model and the flow over the back shell is assumed to be laminar. These approximations are the artifacts of the over-confident design philosophy discussed in Section 1.2. The surface chemistry effects and turbulent heating is amplified as a more optimal estimation requires a more involved analysis. A finite-rate surface chemistry boundary condition for DPLR has been developed by Maclean et al. [71]. This module includes mass and energy balances under the steady-state ablation assumption and can also compute mass blowing due to pyrolysis.

A similarly advanced CFD tool is the US3D code developed jointly by the University of Minnesota and NASA Ames Research Center as an unstructured extension of DPLR's thermochemical framework with additional features [19]. It applies the data-parallel line-relaxation method as in DPLR along surface normal directions, but switches to a point-implicit method when such lines cannot be formed. US3D is capable of employing numerical fluxes of varying degrees of accuracy up to sixth-order. Independent grids for flow and material response can be considered with deforming shapes. Among many cases, US3D has been used in the simulation of the full-scale Space Shuttle Orbiter by Candler et al. [20]. Standard five species air with Park's two-temperature model [100] is used. A partially catalytic radiative equilibrium surface boundary condition is selected. In agreement with flight data, large regions of turbulent heating were identified due to wing protuberances, elevon gaps, and body flaps. With regard to surface reactions, US3D hosts classical equilibrium ablation models as well as the finite-rate chemistry model for air-carbon ablation from Zhluktov and Abe [140]. For a sphere-cone geometry, Candler et al. [21] reported good agreement with similar DPLR solutions. No energy balance was employed at the surface, instead the wall temperature was computed without any surface reactions, then the values were shifted to approximate an ablating surface. Important results of this study pointed out the large differences in species mass fluxes between the two ablation models. Even though the finite-rate chemistry model demonstrated good performance, some relevant reactions which were omitted by Zhluktov and Abe have shown to undermine the accuracy of the model predictions.

Another contemporary solver is the LeMANS code developed by the University of Michigan. LeMANS is an unstructured three-dimensional Navier-Stokes solver for simulating hypersonic nonequilibrium aerothermodynamic flows [114]. It provides second order spatial accuracy and employs a modified Steger-Warming flux vector splitting scheme for discretizing fluxes through cells. For integration in time, a point or line implicit method can be selected. Chemical source terms are obtained from a standard finite-rate chemistry model for reacting air from the work of Park [100], which is compatible with the implemented two-temperature model. Vibrational energy is calculated under the harmonic oscillator assumption.

This code has been used in several cases within the last decade. One example is the case where LeMANS is coupled to a material response code [77]. For the two-dimensional ablative solution, the material response code did not operate in the same domain and was called separately to request the wall temperature, mass blowing rates and the species compositions. The ablation rates were interpolated from thermochemical tables generated by ACE-SNL for carbon in air, which were put together by Aerotherm in 1969. There was an attempt to recess the surface, according to these mass blowing rates. However, the unstructured mesh began to deteriorate as it moved and was misaligned with the shock, which resulted in an accumulating error on the solution. This example underlines the fundamental difficulty for body-conformal grids to operate with strong shocks and recessing boundaries.

Stardust entry has been investigated multiple times through LeMANS. Some of these analyses by Martin et al. [79, 80] consider ablation in an uncoupled approach. An ablative solution calculated only at the stagnation point by external tools is used to scale a radiative equilibrium solution of the surface. In another analysis where a stronger coupling to a material response code is presented [2], pyrolysis gas is assumed to be in chemical equilibrium or frozen. The equilibrium solution produced lower surface heat fluxes as pyrolysis species reacted with and depleted the available oxygen and nitrogen atoms, inhibiting the surface reactions. However, the coupled material response was not able to resolve the

sharp shoulder of the Stardust geometry as it was a one-dimensional code. Hence, the solutions were restricted to the forebody of the capsule.

Lastly, one of the most recent works using LeMANS by Holloway et al. [56] considered a double cone configuration under hypersonic flow conditions. The double cone configuration forms an attached shock at the leading edge and a detached shock downstream due to the second cone. Effects of equilibrium, nonequilibrium and frozen flow on the separation of the boundary layer due to the shock-shock interaction are compared. It was seen that separation location was influenced in all the different thermochemistry models, and separation was delayed when the model approached equilibrium. In this analysis, surface reactions are neglected as only isothermal and radiative equilibrium wall boundary conditions are employed. In all the aforementioned simulations, effects of radiation were neglected.

As hypersonic boundary layers are highly complex due to inherent high temperature effects, nonequilibrium, and unsteadiness, common Reynolds-averaged Navier-Stokes (RANS) simulations, as in the preceding examples, are often not suitable for accurately resolving the fine structures in this regime. High-fidelity CFD techniques are required, which aim to resolve the energy cascade in turbulence to some extent. The most rigorous option is to use direct numerical simulation (DNS) to resolve all the scales. As identified by an early review by Roy and Blottner [111], high-fidelity simulations have generally lacked the implementation of accurate thermochemistry models. Some examples are given here to assess the validity of this concern in recent studies.

Dubief et al. [35] have used DNS for the solution of the Stefan problem, a problem in which a moving boundary experiences phase change, with a simple ablation model based on a Stefan condition with no regard to chemical reactions. Crocker [31] extended this technique with an energy based immersed boundary method to simulate conjugate heat transfer and phase change. This method has been coupled to a finite-volume, high-fidelity, reacting low Mach number flow solver NGA-ARTS, developed jointly by Stanford University, Cornell University and CalTech. Although time-accurate ablation with shape change has been analyzed in detail, ablation is approximated only by macroscopic recession and no chemical reaction mechanism is employed. Due to excessive computational costs with DNS, only low Reynolds number flows are considered.

Another application where ablative simulations are carried out is the investigation of nozzle throats of solid rocket motors, for example, of Ariane boosters. The ablation of the nozzle walls alters the design geometry by increasing the throat section. Reductions in efficiency and thrust may be observed compared to the nominal design. Cabrit et al. [16] have performed DNS on this topic for a subsonic case assumed to be in chemical equilibrium. Ablation with pyrolysis was imposed through a simple mass balance boundary condition only considering oxidation for a stationary isothermal wall at relatively low temperatures.

The previous high-fidelity simulations have not considered any discontinuities in the flow due to compressibility effects, such as strong shocks characteristic of hypersonic speeds. Moreover, thermodynamic and transport properties were mostly calculated using classical mechanics. For a more appropriate hypersonic analysis, Mortensen and Zhong [90] have developed a thermochemical nonequilibrium code with a finite-rate chemistry ablative boundary condition. The code uses a shock-fitting technique based on fifth order finite differences and an explicit Euler scheme for advancing in time. The shock is treated as a boundary, where Rankine-Hugoniot relations provide the jump conditions. In their analysis, 11 nonionizing species have been considered, where chemical reaction rates are taken from Park [100], transport coefficients are found through simplified mixture rules and diffusion is expressed by Fick's law based on a constant Schmidt number. The simplified surface mass and energy balances are considered only for graphite with aims of extrapolating the results to more complex materials. The authors have validated their code based on the spherical test cases of PANT and have applied it to the DNS of Mach 16 flow over a blunt cone. By comparing with a frozen case, it was identified that reactive terms have significantly augmented the instabilities in the boundary layer. In a further analysis employing a similar methodology with linear stability theory (LST) [91], addition of carbon species have resulted in a marginal stabilization, while blowing was destabilizing. Some earlier findings were confirmed through comparison with similar studies in a more detailed review by Zhong and Wang [141].

Groskopf et al. [51] have considered a rigorous approach where a DNS solution has been complimented by a direct simulation Monte Carlo (DSMC) solver to account for the rarefaction effects, that is, when the continuum assumption breaks down. The compromise here was that no GSI is considered as the computational cost would have become insurmountable. To reduce such computational burden in similar works, hybrid approaches such as detached-eddy simulations (DES) have been suggested, where

the main idea was to solve the separated or "detached" regions with large-eddy simulations (LES) and switch to RANS simulations inside the boundary layer [124]. A reactive flow application with this hybrid approach is applied in the investigation of scramjet combustion by Fulton et al. [44]. The authors have used the well-known k-ω turbulence model and hybridized it with a simple subgrid-scale (SGS) model, which assumed that the subgrid fluctuations did not affect the chemical reaction rates according to the laminar chemistry assumption. Salazar et al. [113] have applied DES to a 0.25 meter diameter version of NASA's Orion Multi-Purpose Crew Vehicle at Mach 8 freestream test conditions. No reactions are considered, and transport properties are obtained from simplified mixture rules: diffusivity from constant Schmidt number, viscosity from Wilke's law, and thermal conductivity from constant Prandtl number. US3D has also been used to simulate the same geometry with DES at Mach 6 by Brock et al. [14]. Both works present good agreement with experiments and attribute this accuracy to a better evaluation of the unsteady effects which are lost in RANS simulations. They further note that the largest disagreement in their simulations occurred as the turbulent boundary layer is suppressed to laminar flow after the shoulder of the capsule, which then transitions again along the back shell. Since DES employs turbulence models in the boundary layer, transition was not predicted accurately.

One exceptionally promising approach is proposed by Schrooyen [116], where the flow and material simulations are strongly coupled such that they are solved in the same domain based on a volume-averaging theory applied to the governing equations. A high-order discontinuous Galerkin formulation is used, which benefits from the advantages of finite volume and finite element methods. The solver was able to consider volumetric ablation in addition to surface ablation. Although relatively mild temperatures and speeds are considered for this initial work, inclusion of strong shock for studying hypersonic conditions were planned. With these capabilities, the aim was to consider direct simulations of laminar to turbulent transition in an ablative environment.

To recapitulate on this brief review, state-of-the-art aerothermodynamic CFD tools are either limited by turbulence modeling assumptions of steady flow solutions, or by overwhelming computational requirements of direct simulations. In general, simplified thermochemical and transport models are adopted, which indeed confirms the remark of Roy and Blottner. The addition of detailed aspects such as accurate finite-rate chemistry, detailed multicomponent transport systems or GSI, entails reducing the complexity either by means of neglecting compressibility effects, or by selecting lower order numerical schemes. Furthermore, almost all contemporary solvers for aerothermodynamic flow simulations employ body-conformal grids, which often require painstakingly time-consuming manual grid generation procedures. One historical example notes that it took approximately a month for an experienced user to generate a multi-block structured grid with NASA's LAURA solver [48]. Grid generation is still seen as one of the greatest obstructions on the way of efficient CFD-based design of hypersonic vehicles [9]. In light of these different approaches, it was seen that achieving high-fidelity flow solutions with accurate physicochemical models is of great interest in the atmospheric entry community. Having this capability on a Cartesian grid solver, which can efficiently capture strong shocks and accommodate a surface undergoing gas-surface interactions is another great advantage. These features overcome many of the fundamental deficiencies in the surveyed contemporary analysis tools.

The main motivation behind this study is to lay down the foundations for a novel coupling framework, which can perform high-fidelity flow simulations with accurate physicochemical models on efficiently generated grids. As the initial step in this effort, this work concerns itself with the implementation, verification and validation of the extended capabilities of this analysis tool. To that end, a high-order finite volume scheme with a Cartesian grid immersed boundary method is applied to hypersonic flows in entry conditions. Accurate thermodynamic and transport properties are incorporated through the coupling of an external library. Effects of GSI are also included through a unique implementation in the immersed boundary method. Hence, a distinctive state-of-the-art approach in aerothermodynamic CFD research is proposed.

1.4. Thesis Objectives and Outline

The main objective of this thesis is the development of a novel aerothermodynamic flow analysis tool for better thermal protection system design, by coupling a high-fidelity flow solver with an accurate thermodynamic and transport properties library. The flow solver in consideration is called INCA, which is a Cartesian grid immersed boundary finite-volume code written in modern Fortran. INCA is capable of performing high-order accurate simulations, LES, and DNS. The external code is the MUlticom-

ponent Thermodynamics And Transport properties for IONized gases library in C++ (Mutation^{++}) developed by Scoggins et al. [118, 120] at VKI. Mutation^{++} provides a repository for detailed evaluation of thermodynamics, transport properties, chemical kinetics and gas-surface interactions, where latest advancements are externally made available. This novelty obviates the need for manually searching and preparing the most up-to-date data and algorithms, which are often hard-coded into common CFD tools. Mutation^{++} operates independently from the numerical methods being employed in the main aerodynamic solver. Due to its open-source availability, Mutation^{++} also serves to build a compendium, that incentivizes collaboration between different research groups and enables post-release support for further development. Notably, Mutation^{++} has been utilized in the aforementioned work of Schrooyen [116], and there are ongoing efforts at VKI to couple it with US3D as well.

As concluded from the literature review, accurate thermochemistry, transport properties and surface reactions are mostly simplified and hard-coded in high-fidelity flow solvers. Incorporation of these accurate physicochemical models in a high-fidelity framework with efficient grid generation capabilities can enable safer and more effective design of future space exploration vehicles. As atmospheric entry flow regimes have not been investigated with INCA prior to this study, the capabilities and limitations of the standalone solver in these regimes were unknown. To identify these characteristics, a research question is proposed as the following:

> *How well can a general-purpose flow solver predict atmospheric entry environments, first with its baseline models and after accurate physicochemical implementations?*

This will be assessed by comparing both standalone INCA and INCA with Mutation^{++} under the same case studies. Agreement of both distributions with the results in literature will be compared. The outcome will evaluate the applicability of the current models in INCA and determine if the Mutation^{++} implementation is able to enhance or enable the analysis of relevant flow problems.

Undoubtedly, this comparison must also take into account the overall efficiency of these simulations. One of the main concerns in such a framework is the computational overhead that these accurate models produce as they are being requested from an external library. Hence, the equally important second research question motivating this study asks:

> *What is the trade-off between accuracy and computational efficiency, when developing a high-fidelity aerothermodynamic flow analysis tool for the prediction of atmospheric entry environments?*

In other words, is the benefit gained from accurate physicochemical model implementations justified for the computational cost that they entail? Answers to these questions are sought by coupling INCA with Mutation^{++} to have an innovative contribution to the Mutation^{++} community, and to extend INCA's high-fidelity flow simulation capabilities to atmospheric entry flows.

The coupling procedure involves a step-by-step implementation of all four of the modules within Mutation^{++}. First, the thermodynamics module provides species and mixture properties such as chemical equilibrium compositions, energies, enthalpies, and specific heats for the closure of the governing equations. Instead of INCA's combustion-oriented database, Mutation^{++} provides the necessary properties compiled specifically for entry applications. In addition to being able to compute chemical nonequilibrium, Mutation^{++} introduces thermal nonequilibrium by complementing the additional conservation equations supplied by INCA. The second module provides the transport properties, namely, the diffusivity, viscosity and thermal conductivity of a mixture, which essentially regulate the transport of mass, momentum and energy in a fluid domain, respectively. Mutation^{++} supplies accurate kinetic theory data and robust solution of transport systems, instead of the simplified mixture rules previously used within INCA. The third module considers the chemical reactions taking place in the mixture. This module computes the amount of species and energy being consumed or produced by a reaction. Mutation^{++} allows for an efficient evaluation of these quantities, which provide closure to the chemical source terms. The fourth and final module of Mutation^{++} is a unique implementation providing the computation of gas-surface interactions for catalytic and ablative reactions as wall boundary conditions [7, 120]. This module solves the mass and energy balances at an interface and computes the amount of mass blowing as the material ablates. Once the coupling is completed, relevant test cases are considered to validate each of the implemented modules. Since this thesis was concerned with the verification and validation of these implementations to determine the foreseeable potential of this framework, high-order WENO schemes are selected to efficiently test these new additions under various flow conditions. LES or

DNS test cases were naturally impractical within the scope of this thesis due to the many uncertainties surrounding the solver's capabilities under these flow regimes. Such studies are planned as a successor to this work and are discussed at the end of this report.

Following this introduction, the working principles of these modules are elucidated in Chapter 2. Numerical aspects of the flow solver and the coupling strategy are discussed in Chapter 3. Finally, results for relevant test cases are presented in Chapter 4 and are followed by conclusive remarks in Chapter 5.

2

Physicochemical Modeling

Modeling high-enthalpy flows demands multidisciplinary expertise in various fields of science. The modules within a flow solver, which provide closure to the governing equations of the flow, can be summarized by the four pillars of aerothermodynamic modeling: thermodynamics, transport properties, chemical kinetics and gas-surface interactions. These are presented in this chapter.

2.1. Governing Equations

The Navier-Stokes equations that govern the fundamental principles of mass, momentum and energy conservation within a flow field, can be derived either with the classical control volume approach in a macroscopic sense [3] or from kinetic theory of gases in the framework of the Chapman-Enskog theory applied to the multi-species Boltzmann equation in a mesoscopic sense [55]. In this section, they are presented in their conservative differential forms for a reacting multicomponent gas in thermal equilibrium. Thermal nonequilibrium is addressed in Section 2.2.2, Section 2.2.3, and Section 2.5.

Mass Conservation

Global mass conservation of the system is ensured by

$$\frac{\partial \rho}{\partial t} + \boldsymbol{\nabla} \cdot (\rho \mathbf{u}) = 0 \,, \tag{2.1}$$

where ρ is the mixture density and $\mathbf{u}$ is the mixture average velocity.

For each distinct species in the mixture, a species continuity equation needs to be solved. For a chemically reacting mixture, the species continuity equation for the i^{th} species can be written as

$$\frac{\partial \rho_i}{\partial t} + \boldsymbol{\nabla} \cdot (\rho_i \mathbf{u} + \mathbf{J}_i) = \dot{\omega}_i \,, \tag{2.2}$$

where ρ_i is the partial density of the species, $\mathbf{J}_i = \rho_i \boldsymbol{\mathcal{V}}_i$ is the diffusion flux of the species with the species diffusion velocity $\boldsymbol{\mathcal{V}}_i$ and $\dot{\omega}_i$ is the source term associated with the production or consumption of species due to chemical reactions. Note that $\sum_i \dot{\omega}_i = 0$, since chemical reactions inherently conserve mass and by definition $\sum_i \rho_i = \rho$. Hence, as the global continuity equation must be retrieved by summing up all the species continuity equations, the sum of the diffusion fluxes vanish, such that $\sum_i \mathbf{J}_i = 0$.

Momentum Conservation

Conservation of momentum within the system is ensured by Newton's second law of motion as

$$\frac{\partial \rho \mathbf{u}}{\partial t} + \boldsymbol{\nabla} \cdot (\rho \mathbf{u} \otimes \mathbf{u}) + \boldsymbol{\nabla} p = \boldsymbol{\nabla} \cdot \overline{\overline{\boldsymbol{\tau}}} + \mathbb{F}_{ext} \,, \tag{2.3}$$

where p is the mixture pressure, $\overline{\overline{\boldsymbol{\tau}}}$ is the viscous stress tensor and $\mathbb{F}_{ext}$ refers to the external body forces arising due to gravitational or electromagnetic fields, which are negligible under the conditions studied in this context.

Energy Conservation

Conservation of total energy in the system is given by

$$\frac{\partial \rho E}{\partial t} + \boldsymbol{\nabla} \cdot \left[(\rho E + p)\, \mathbf{u} \right] + \boldsymbol{\nabla} \cdot \mathbf{q} = \boldsymbol{\nabla} \cdot \left(\overline{\overline{\boldsymbol{\tau}}} \cdot \mathbf{u} \right) + \dot{\Omega}_{rad} + E_{ext} \,, \tag{2.4}$$

where $E = e + u^2/2$ is the specific total energy, which is the sum of the thermodynamic internal energy e and the kinetic energy, $\mathbf{q}$ is the total heat flux, $\dot{\Omega}_{rad}$ is the radiative source term, and E_{ext} includes the work done by the external body forces $\mathbb{F}_{ext}$. Contribution from radiation and external forces are neglected for the cases considered in this study.

2.2. Thermodynamics

The closure of the governing equations for high temperature reacting flows requires the evaluation of the thermodynamic properties of the fluid. Unlike common applications in aerodynamics, assuming that these properties are constant or only temperature dependent is no longer valid at these flight regimes. Mixture properties are obtained from the summation of species properties weighted by the chemical compositions. The species properties depend on the thermochemical state of the system, and are accordingly obtained from statistical thermodynamics and empirical data. The following expressions for the mixture state are valid under the assumption of thermal equilibrium.

2.2.1. Mixture Properties

Mixture properties are based on the contribution of each species. Chemical composition of a mixture weighs these contributions and can be described by a set of intensive variables. From their definitions, mole fraction x_i is the number of moles of species i per mole of mixture, and the mass fraction $y_i = \rho_i/\rho$ is the mass of species i per unit mass of mixture, such that, respectively summing up these variables for all species gives unity. Conversions between these variables can be obtained from

$$y_i = x_i \frac{M_i}{M} \,, \tag{2.5}$$

where the average molar mass of a mixture M can be computed from the species molar mass M_i with either of the preceding variables as

$$M = \sum_i x_i M_i \quad \text{or} \quad \frac{1}{M} = \sum_i \frac{y_i}{M_i} \,, \tag{2.6}$$

where the summations are over all species.

In Fig. (2.1), variation of equilibrium mass fractions at 0.5 atm with respect to temperature of two commonly used mixtures in the aerothermodynamic community is plotted. The first one considers the 5-species air mixture with N, O, NO, N_2, O_2, while the second 11-species mixture also considers the charged counterparts and free electrons. It can be seen that mass fractions of free electrons, N^+, and O^+ become significant approximately after 10 000 K, and keep rising for higher temperatures. Among all the cases studied in this study, these temperature ranges have been avoided and the effects of ionization have been neglected in accordance with the compared results from literature in Chapter 4. Indeed, Mutation^{++} is equipped with the necessary means to include ionized mixtures by providing suitable relations to calculate transport properties and chemical reactions for charged interactions. This is just another feature enabled implicitly by this coupling, but not tackled within the scope of this study.

The Mutation^{++} library employs the ideal gas assumption, which considers the intermolecular forces to be negligible and allows for the use of the following equation of state

$$p = \rho R T \,, \tag{2.7}$$

where p is the pressure, ρ is the density, $R = \mathcal{R}/M$ is the mixture gas constant with the universal gas constant $\mathcal{R}$, and T is the temperature for the overall mixture. These mixture properties are obtained according to their constituent species as

$$p = \sum_i p_i \,, \quad \rho = \sum_i \rho_i \,, \quad R = \sum_i y_i R_i \,, \tag{2.8}$$

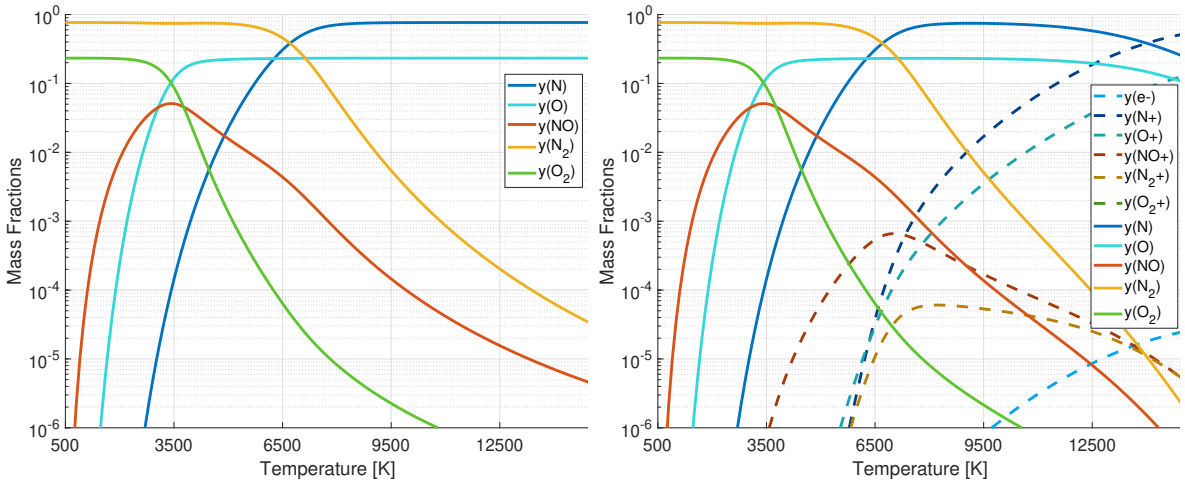

(a) **(b)**

Figure 2.1: Species mass fractions at equilibrium for 0.5 atm from Mutation^{++} for (a) 5-species air and (b) 11-species air including ionization.

where from Dalton's law $p_i = x_i p$ is the partial pressure that would exist if the species i were to solely inhabit the same volume of mixture at the same temperature, ρ_i is the species density given by the mass of the species per unit volume of the mixture, and $R_i = \mathcal{R}/M_i$ is the specific gas constant for the species. These species quantities can also be related through the ideal gas law as

$$p_i = \rho_i R_i T \,. \tag{2.9}$$

Knowing the mixture pressure and density, then the specific energy e for the mixture can be obtained by

$$e = h - \frac{p}{\rho} \,, \tag{2.10}$$

provided that the specific enthalpy h is given through its species counterpart h_i by

$$h = \sum_i y_i h_i(T) \,. \tag{2.11}$$

Computation of the species terms will be discussed in Section 2.2.2 and Section 2.2.3. Similarly, the mixture entropy s of an ideal gas can be obtained from

$$s = \sum_i y_i \left[s_i(p,T) - R_i \ln x_i \right] \,, \tag{2.12}$$

where s_i is the specific entropy for species i and the additional term is associated with mixing.

An important property for the calculation of the equilibrium constants, that will be presented in Section 2.4, is the Gibbs free energy. It is a parameter used to describe the spontaneity in the occurrence of a chemical reaction, and for a species i it is defined as

$$g_i(p,T) = h_i - T s_i \,, \tag{2.13}$$

for a mixture this yields

$$g = \sum_i y_i \left(g_i - R_i \ln x_i \right) \,. \tag{2.14}$$

Specific heats at constant pressure c_p and constant volume c_v of the mixture are defined as

$$c_p = \left(\frac{\partial h}{\partial T} \right)_p \,, \tag{2.15}$$

$$c_v = \left(\frac{\partial e}{\partial T} \right)_v \,. \tag{2.16}$$

Writing these expressions in terms of the species contributions as in Eq. (2.11) yields

$$c_p = \sum_i \left[y_i \left(\frac{\partial h_i}{\partial T} \right)_p + h_i \left(\frac{\partial y_i}{\partial T} \right)_p \right] , \tag{2.17}$$

$$c_v = \sum_i \left[y_i \left(\frac{\partial e_i}{\partial T} \right)_v + e_i \left(\frac{\partial y_i}{\partial T} \right)_v \right] , \tag{2.18}$$

where the first terms in both equations are in fact the specific heats of species $c_{p,i} = (\partial h_i/\partial T)_p$ and $c_{v,i} = (\partial e_i/\partial T)_v$. These equations are valid for a chemically reacting mixture in equilibrium. In the case of frozen flow, where the chemical time scales are practically zero or much smaller than the flow time scales, the derivatives in the second terms vanish, and the remaining first terms are referred to as the frozen specific heats. Then, equations for chemical equilibrium can be rewritten as

$$c_p = c_{p,fr} + \sum_i h_i \left(\frac{\partial y_i}{\partial T} \right)_p , \tag{2.19}$$

$$c_v = c_{v,fr} + \sum_i e_i \left(\frac{\partial y_i}{\partial T} \right)_v , \tag{2.20}$$

where the specific heats are given as the combination of a frozen component attributed to a fixed composition, and a chemically reactive term associated with the variation of the composition with respect to temperature.

An additional variable commonly required is the speed of sound, which is defined as

$$a^2 = \left(\frac{\partial p}{\partial \rho} \right)_s , \tag{2.21}$$

and takes on the following form for a flow in equilibrium

$$a_{eq}^2 = \gamma_{eq} RT \frac{1 + \left(\frac{1}{p} \right) \left(\frac{\partial e}{\partial v} \right)_T}{1 - \rho \left(\frac{\partial h}{\partial p} \right)_T} , \tag{2.22}$$

which reduces to the familiar expression for a frozen flow given by

$$a_{fr}^2 = \gamma_{fr} RT , \tag{2.23}$$

where $\gamma_{eq} = c_{p,eq}/c_{v,eq}$ and $\gamma_{fr} = c_{p,fr}/c_{v,fr}$ are the ratios of specific heats at equilibrium and frozen conditions, respectively [4]. For flows at one of these limiting conditions, the choice of the expression to use is trivial. This is not the case when nonequilibrium prevails. In this study, the frozen speed of sound has been chosen to be consistent with the chemical nonequilibrium regime.

2.2.2. Species Properties

It is evident that the calculation of pure species enthalpies, energies and entropies are necessary to evaluate the thermodynamic properties of a mixture. Calculation of these quantities depends on the thermochemical state of the system. For sufficiently large flow time scales allowing enough collisions to occur, the system is said to be in local thermodynamic equilibrium. Then the energy level populations follow a Boltzmann distribution, such that a single temperature can be adopted to describe the mixture. Thermal nonequilibrium arises when different energy modes are excited. For an atom these are the translational mode e^{T}, associated with the kinetic energy of the atom from the motion of its center of mass, and the electronic mode e^{E}, associated with the energy of the motion of electrons about the nucleus. For a molecule there are two additional energy modes, namely the rotational mode e^{R}, attributed to the rotation of the molecule around the three orthogonal axes, and the vibrational mode e^{V}, referring to the energy of the atoms of a molecule that are vibrating with respect to an equilibrium position.

From quantum mechanics, it is known that energy in these modes is stored in quantized levels which can only take discrete values. An energy level may contain quantized orientations called states where

the number of these states having the same energy level are referred to as the degeneracy of that level. These degeneracies are described in quantum mechanics as a result of the multiple solutions obtained from the Schrödinger's equation [55].

Conventionally, instead of energies, enthalpies are used to express the state of a system. The total enthalpy of an atom or a molecule is equal to the sum of its respective energy modes and the contribution from chemistry, such that

$$h_{i,atom} = h_i^{\mathrm{T}} + h_i^{\mathrm{E}} + (\Delta h_f)_i \,, \tag{2.24}$$

$$h_{i,molecule} = h_i^{\mathrm{T}} + h_i^{\mathrm{R}} + h_i^{\mathrm{V}} + h_i^{\mathrm{E}} + (\Delta h_f)_i \,, \tag{2.25}$$

where the result of the summations are the absolute specific enthalpies referring to the total of the sensible and the formation enthalpies $(\Delta h_f)_i$ combined. Formation enthalpies are derived from the zero-point energies of species, which are the energies at a reference temperature. Obtaining these zero-point energies is impossible with calculations or measurements. Fortunately, adherence to the first law of thermodynamics ensures that all applications require only the differences in energies to be found, as the energy is conserved. In a trivial fashion, it can be proven that this change in zero-point energies is equal to the change in the formation enthalpies of the same reaction [3]. This heat of formation is defined as the energy needed in order to form one mole of substance from its constituent elements at standard conditions. The choice of these conditions does not affect the results, but conventionally they are taken as standard state at 298.15 K and 1 atm, where formation enthalpies of species in their natural states are zero.

According to the choice of practice, conservation of energy expressed in Eq. (2.4) can be written for absolute or sensible energies. The derivation is straightforward as the main formulation is preserved, when the energies are shifted by the formation enthalpies. The only caveat is, when sensible energies are considered, an additional source term is required on the right-hand side of the equation in the following form

$$\dot{\Omega}_f = -\sum_i \dot{\omega}_i (\Delta h_f)_i \,, \tag{2.26}$$

where $\dot{\omega}_i$ is the mass production rate to be derived in Section 2.4, which weighs the formation enthalpies to account for the heat release due to chemical reactions. INCA is able to work with both definitions, but for the present implementation the energy equation is written for absolute values and the source term does not appear.

Species thermodynamic properties for each of the energy modes are obtained through databases discussed in Section 2.2.3. Rotational, vibrational and electronic modes can be grouped under the heading of internal energy e_i^{I}. Essentially, all energy modes are coupled. However, under the Born-Oppenheimer approximation, translational and internal energy modes can be considered independently. This is not a direct consequence of this approximation, yet this interpretation is widely accepted in the aerothermodynamics community. Since the translational mode has very narrow spacings between its energy levels, it can be considered as continuous, and assumed to be decoupled from the internal modes which are kept discrete. INCA is currently build around a thermal equilibrium assumption. The coupling with Mutation^{++} allows examining thermal nonequilibrium as well, which is discussed in Section 2.5.

2.2.3. Databases

Calculation of the species properties for the different energy modes discussed in Section 2.2.2 will be presented here. Two sets of databases are available within Mutation^{++}: a compilation of spectroscopic data based on the Rigid-Rotor Harmonic-Oscillator (RRHO) model, and a collection of data sources in NASA's polynomial curve-fit format. Access to these databases inside Mutation^{++} eliminates the need for manually preparing the required species property files, as it is currently the way of practice for standalone INCA. This approach is generally prone to user mistakes and faulty interpretation errors. In fact, it was realized that such a misinterpretation was taking place within INCA, which caused the database and species properties files to overwrite each other instead of a complementary selection. This meant that an unspecified value in one of the files could overwrite the other value to yield an unphysical zero as the outcome. Another issue was based on a mismatch between the input units being interpreted erroneously by the code. Together with another issue regarding the choice of absolute and sensible

enthalpies, the errors were miraculously canceling out for certain simulations, that they have remained unnoticed for past studies. These are the aspects the Mutation^{++} implementation aims to remedy.

As opposed to the combustion-oriented data and models typically used by INCA for thermal equilibrium flows, the properties provided within Mutation^{++} are selected specifically for species in entry environments and thermochemical nonequilibrium could be included through the RRHO database.

Rigid-Rotor and Harmonic-Oscillator Model

RRHO model is based on the rigid-rotor approximation expressing a diatomic molecule as two masses at a fixed distance from each other, and the harmonic-oscillator approximation employing a spring analogy. Together, these models can be used to provide a simple yet effective framework for the rotational and vibrational modes of molecules. Here, an additional assumption is that the modes are taken to be in thermodynamic equilibrium.

The translational mode is often decoupled from the internal modes as discussed in Section 2.2.2. With the aid of statistical thermodynamics and quantum mechanics [133], expressions for the i^{th} species energy, enthalpy and entropy can be readily obtained for the translational mode as

$$h_i^{\mathrm{T}} = e_i^{\mathrm{T}} + R_i T = \frac{3}{2} R_i T + R_i T = \frac{5}{2} R_i T \,, \tag{2.27}$$

$$s_i^{\mathrm{T}} = \frac{h_i^{\mathrm{T}}}{T} + R_i \ln \left[\frac{k_B T}{p_i} \left(\frac{2\pi M_i k_B T}{N_A h_P^2} \right)^{\frac{3}{2}} \right] , \tag{2.28}$$

where k_B is the Boltzmann constant, N_A is the Avogadro number and h_P is the Planck's constant.

For the rotational mode, species properties are given by

$$h_i^{\mathrm{R}} = e_i^{\mathrm{R}} = \frac{\mathcal{L}}{2} R_i T \,, \tag{2.29}$$

$$s_i^{\mathrm{R}} = \frac{h_i^{\mathrm{R}}}{T} + R_i \left[\frac{\mathcal{L}}{2} \ln \left(\frac{T}{\theta_i^{\mathrm{R}}} \right) - \ln \sigma_i \right] , \tag{2.30}$$

where θ_i^{R} is the characteristic rotational temperature, indicating a threshold beyond which the rotational mode becomes excited. To account for the additional degrees of freedom, $\mathcal{L} = 2$ for linear molecules and $\mathcal{L} = 3$ for others. Lastly, σ_i is the steric factor related to the symmetry of the molecule, and it is equal to 1 for heteronuclear diatomic molecules such as CO and NO, equal to 2 for CO_2 and homonuclear diatomic molecules such as O_2 and N_2, and can be larger for polyatomic molecules. The rationale behind these differences in orientation are rooted in the degeneracies briefly mentioned in Section 2.2.2. In classical terms, they are due to different orientations of a molecule being indistinguishable or instead, dissimilar from one another.

Considering the vibrational mode next yields

$$h_i^{\mathrm{V}} = e_i^{\mathrm{V}} = R_i \sum_m \frac{\theta_{i,m}^{\mathrm{V}}}{\exp\left(\theta_{i,m}^{\mathrm{V}}/T\right) - 1} \,, \tag{2.31}$$

$$s_i^{\mathrm{V}} = \frac{h_i^{\mathrm{V}}}{T} - R_i \sum_m \ln \left[1 - \exp\left(\frac{-\theta_{i,m}^{\mathrm{V}}}{T} \right) \right] , \tag{2.32}$$

where $\theta_{i,m}^{\mathrm{V}}$ is the characteristic vibrational temperature, and the summation over m is for different vibrational modes again due to different orientations of a molecule. Number of vibrational modes of a molecule is given by $m = 3\mathfrak{n} - \mathcal{L} - 3$, where $\mathfrak{n}$ is the number of atoms comprising that molecule.

Finally, the equations for the electronic mode can be obtained separately from the RRHO approximations, and are written as

$$h_i^{\mathrm{E}} = e_i^{\mathrm{E}} = R_i \frac{\sum_l \mathfrak{g}_{i,l} \theta_{i,l}^{\mathrm{E}} \exp\left(-\theta_{i,l}^{\mathrm{E}}/T\right)}{\sum_l \mathfrak{g}_{i,l} \exp\left(-\theta_{i,l}^{\mathrm{E}}/T\right)} \,, \tag{2.33}$$

$$s_i^{\mathrm{E}} = \frac{h_i^{\mathrm{E}}}{T} + R_i \ln \sum_l \mathfrak{g}_{i,l} \exp\left(-\theta_{i,l}^{\mathrm{E}}/T\right) \,, \tag{2.34}$$

where l denotes different electronic levels, $\mathfrak{g}_{i,l}$ refers to the degeneracy, and $\theta^{\mathrm{E}}_{i,l}$ is the characteristic electronic temperature. To prevent the summations from diverging, a finite number of electronic levels are considered for each species [117].

One of the main advantages of the RRHO model is that it is not specific to certain temperature ranges, in contrast to similar empirical databases. This enables a continuous representation of the species properties, which is especially useful when derivatives of these quantities are being sought. Although the RRHO model is known to provide acceptable results in the past, it is restricted by inherent limitations [133]. One issue is the anharmonicity in the vibrational mode associated with the interatomic forces. Instead of a spring having an identical response for the two atoms of a molecule becoming closer or further apart, in reality there are repulsive and attractive forces at play, which significantly alter the energy levels of a vibrational excitation. Additionally, the coupling between the rotational and vibrational modes should be taken into account as their effects are of similar order. Furthermore, since the RRHO model does not consider chemical reactions, as the temperature increases, more and more molecules begin to dissociate, and the diatomic molecule assumption starts to become invalid. Hence, even though the RRHO model is a powerful tool, it should be applied with caution.

NASA Thermodynamic Polynomials

The NASA Glenn Research Center's database developed by Gordon and McBride [82] was presented through NASA's Chemical Equilibrium with Applications (CEA) program. The database is based on the polynomial fits for species properties, and it is among one of the more widely used sources in the aerothermodynamics community. These polynomials are provided in 7- or 9- coefficient forms for thermodynamic properties as

$$\frac{c_{p,i}}{R_i} = a_{0i}T^{-2} + a_{1i}T^{-1} + a_{2i} + a_{3i}T + a_{4i}T^2 + a_{5i}T^3 + a_{6i}T^4 \,, \tag{2.35}$$

which can be integrated from their definitions to provide the species enthalpies and entropies as

$$\frac{h_i}{R_i T} = -a_{0i}T^{-2} + a_{1i}\frac{\ln T}{T} + a_{2i} + \frac{a_{3i}}{2}T + \frac{a_{4i}}{3}T^2 + \frac{a_{5i}}{4}T^3 + \frac{a_{6i}}{5}T^4 + \frac{b_1}{T} \,, \tag{2.36}$$

$$\frac{s_i}{R_i} = -\frac{a_{0i}}{2}T^{-2} - a_{1i}T^{-1} + a_{2i}\ln T + a_{3i}T + \frac{a_{4i}}{2}T^2 + \frac{a_{5i}}{3}T^3 + \frac{a_{6i}}{4}T^4 + b_2 \,, \tag{2.37}$$

where b_1 and b_2 are the integration constants and they are available in the database together with the polynomial coefficients for specific ranges of temperatures.

The CEA database has been complimented in Mutation^{++} with updated values from several sources. Main improvements aimed for a more consistent treatment of species formation enthalpies. Scoggins et al. [119] have compiled an extensive database for over 1200 neutral and ionized species in carbon-phenolic mixtures, to be utilized in ablative reactions. A more exhaustive summary of the complete database is provided in the documentation of Mutation^{++} [117].

2.3. Transport Properties

At the microscopic scale, tracking the interaction between each particle based on Newton's second law provides the particles' position and time according to molecular dynamics. This approach is usually too costly due to the sheer number of particles to evaluate. A statistical approach can be considered when the number of particles exceed approximately a million, such that the statistical fluctuations become insignificant. In this regime, kinetic theory can be applied by making use of the Boltzmann equation. This theory enables establishing a link between the transport fluxes of conservative properties present in the Navier-Stokes equations, namely mass, momentum, and energy, with the macroscopic forces that produce them, such as the gradients of thermodynamic properties. This is accomplished by means of proportionality coefficients called the transport properties, like diffusivity, viscosity and thermal conductivity, which are associated with the diffusion fluxes $\mathbf{J}_i$, the viscous stress tensor $\overline{\overline{\boldsymbol{\tau}}}$, and the heat flux $\mathbf{q}$, introduced in Section 2.1. These properties provide a closure to the macroscopic conservation equations, and they are presented in this section. For the sake of brevity, the theory is presented for heavy particle collisions only, and neglects charged particle interactions.

Following the discussion of Hirschfelder, Curtiss and Bird [55], explicit forms of the transport fluxes are obtained by solving the Boltzmann equation with the Chapman-Enskog perturbative expansion

method. This theory provides a framework such that Navier-Stokes equations which govern the macroscopic dynamics of fluids, can be derived from the Boltzmann equation expressing the domain of mesoscopic statistics. Since point particles are assumed, internal energy modes and chemical reactions are not considered. Boltzmann's equation essentially describes the evolution of the velocity distribution in phase space. The multi-dimensional phase space is comprised of the spatial dimensions, velocity of the particle along these dimensions with respect to the bulk, and time. For this velocity distribution function $f_i(\mathbf{x}, \mathbf{u}, t)$ for species i, Boltzmann's equation is written as

$$\frac{\partial f_i}{\partial t} + \mathbf{u}_i \cdot \boldsymbol{\nabla}_x f_i + \frac{\mathbb{F}_i}{m_i} \cdot \boldsymbol{\nabla}_u f_i = \sum_i \mathcal{J}_{ij}(f_i, f_j) \,, \tag{2.38}$$

where the left-hand side is referred to as the streaming operator, which includes the temporal and convective rates of changes, and the influence of the applied body forces $\mathbb{F}$. The right-hand side is the collisional operator, which accounts for the collisions that affect the velocity distribution of particles through the partial collision operator $\mathcal{J}_{i,j}(f_i, f_j)$. Here the reactive collisional operator is omitted. Maxwell's transfer equations can be used to express the terms of the streaming operator regarding the transport fluxes, which depend on the velocity distribution function for the closure of the system. Under the assumption of molecular chaos, stating that the particle velocities are uncorrelated prior to colliding, the partial collisional operator for binary elastic collisions is given as

$$\mathcal{J}_{ij}(f_i, f_j) = \int\int\int (f_i' f_j' - f_i f_j) |\mathbf{u}_i - \mathbf{u}_j| b \, db d\epsilon d\mathbf{u} \,, \tag{2.39}$$

where prime values indicate particle states after the collision, b is the impact factor based on the offset of the two particles, and ϵ is the out-of-plane angle of approach. Boltzmann has shown through the H-theorem, that the resulting equation in Eq. (2.38) has a unique solution in the form of a Maxwell-Boltzmann distribution under the assumption of equilibrium. The Euler equations governing inviscid flows and the perfect gas law for dilute gases are recovered from these formulations of kinetic theory.

Considering the dissipative effects is accomplished by perturbing the linearized Boltzmann equation out of equilibrium. The Boltzmann equation is first nondimensionalized. Then, a small perturbation is applied in the form of an infinite series of a parameter ε, describing the asymptotic deviation from equilibrium as

$$f_i = f_i^{(0)} + \varepsilon f_i^{(1)} + \mathcal{O}(\varepsilon^2) \,, \tag{2.40}$$

where $f_i^{(0)}$ is the zeroth order distribution function and so on. This parameter ε, which stands for the Knudsen number, is taken very small, such that the system remains collision dominated, and a continuum description is still valid. Among the infinitely many solutions that this perturbation provides, a unique solution is obtained by constraining the perturbation effects and truncating the infinite series. The main assumption of this theory establishes that the macroscopic properties (ρ, $\rho\mathbf{u}$, ρe) are based on the zeroth order velocity distribution function. Then, the first order approximation is associated to dissipative effects and yields the Navier-Stokes equations. This result was first obtained by Chapman and Enskog independently, and it required the solution of an integro-differential equation for the calculation of the transport properties [55]. The solutions involved expanding the integrals in a finite series of Sonine polynomials of varying order. The resulting expressions for the transport properties depend on collision integrals, which represent an average over all possible relative energies between the particles. For two interacting species i and j, they are given in the following form

$$\Omega_{ij}^{(l,s)}(T_{ij}) = \sqrt{\frac{k_B T_{ij}}{2\pi \varpi_{ij}}} \int_0^\infty e^{-\varrho^2} \varrho^{2s+3} Q_{ij}^{(l)} \, d\varrho \,, \tag{2.41}$$

where l and s refer to the Sonine polynomial order, $\varpi_{ij} = (m_i^{-1} + m_j^{-1})^{-1}$ is the reduced mass of colliding particles, $\varrho = \sqrt{\varpi_{ij} \bar{g}^2 / 2 k_B T_{ij}}$ is the ratio of kinetic to thermal energy with relative collision velocity $\bar{g}$, and Q_{ij}^l is the generalized collision cross section given as

$$Q_{ij}^{(l)} = 2\pi \int_0^\infty \left(1 - cos^l \chi_{ij}\right) b \, db \,, \tag{2.42}$$

with the deflection angle of the collision given by

$$\chi_{ij} = \pi - 2b \int_{r_m}^{\infty} \frac{d\hat{r}}{\hat{r}^2 \sqrt{1 - b^2/\hat{r}^2 - \phi_{ij}(\hat{r})/\frac{1}{2}\varpi_{ij} g^2}} \,, \tag{2.43}$$

where $\hat{r}$ is the distance between particles, $\hat{r}_m$ is the distance of closest approach, and ϕ_{ij} is the intermolecular interaction potential. The collision integrals are usually expressed in a reduced form for hard-sphere cross-sections as

$$\bar{Q}_{ij}^{(l,s)} = \frac{4(l+1)}{(s+1)!\,(2l+1-(-1)^l)} \int_0^{\infty} e^{-\varrho^2} \varrho^{2s+3} Q_{i,j}^{(l)} \, d\varrho \,. \tag{2.44}$$

Interaction potentials in Eq. (2.43) are usually obtained from experimental measurements and are tabulated or fitted into polynomials. Scoggins [117] gives details on the interaction potentials provided in Mutation^{++} for a wide range of conditions including air, carbon species and the Martian atmosphere. Hence with these values, the transport properties can be calculated for a system. The implementation of Mutation^{++} offers an accurate and up-to-date improvement to the current procedure in INCA, which relies on an empirical Neufeld approximation for calculating the collision integrals [38]. Moreover, INCA considers simplified mixture rules, which disregard the multicomponent interactions between species. Whereas, Mutation^{++} evaluates the full Chapman-Enskog system instead. In the sections that follow, different multicomponent approaches for evaluating each transport property of a mixture will be presented.

2.3.1. Diffusivity

Accurate prediction of mass diffusion is of great importance in hypervelocity reacting flows, as significant discrepancies can occur depending on the fidelity of the selected diffusion model [87, 126]. These inconsistencies can have an effect on heat transfer, species fractions and also on mass blowing rates for ablative simulations [1, 17]. Chapman-Enskog approximation yields the species diffusion velocity $\boldsymbol{\mathcal{V}}_i$, introduced in Eq. (2.2) in relation with the diffusion flux $\mathbf{J}_i = \rho_i \boldsymbol{\mathcal{V}}_i$, as

$$\boldsymbol{\mathcal{V}}_i = -\sum_j D_{ij} \mathbf{d}_j \,, \tag{2.45}$$

where D_{ij} is the multicomponent diffusion coefficient matrix, and $\mathbf{d}_j$ is the vector of species driving forces given by

$$\mathbf{d}_j = \boldsymbol{\nabla} x_j + (x_j - y_j)\, \boldsymbol{\nabla} \ln p - \frac{y_j}{p} \left(\rho \mathbb{F}_j - \sum_k \rho_k \mathbb{F}_k \right) \,. \tag{2.46}$$

The driving force vector conveys the influence of chemical composition, pressure gradients, and the acting body forces. Computation of multicomponent diffusion coefficients depends on the evaluation of binary collision integrals and the chemical composition of the mixture. Depending on the order of the Sonine polynomial, a linear system needs to be solved, which is often computationally demanding. Thus, a common practice is to resort to simplified models.

Note that for a binary mixture, the famous Fick's law is written as

$$\mathbf{J}_i = -\rho \mathscr{D}_{ij} \boldsymbol{\nabla} y_i \,, \tag{2.47}$$

where the binary diffusion coefficients $\mathscr{D}_{ij}$ are provided by the first order approximation of the Chapman-Enskog expansion as

$$\mathscr{D}_{ij} = \frac{3}{16 n} \sqrt{\frac{2\pi k_B T}{\varpi_{ij}}} \frac{1}{\bar{Q}_{ij}^{(1,1)}} \,, \tag{2.48}$$

which are symmetric, $\mathscr{D}_{ij} = \mathscr{D}_{ji}$. Here n is the number density. The diffusion coefficient in Fick's law can be manipulated to approximate non-binary mixtures. For example, the most trivial models are based on constant Schmidt or Lewis numbers, which relate the rate of mass diffusion to the viscous and thermal diffusion rates, respectively. In these models the diffusivity is assumed to be constant for all species. However, more detailed representations are needed for an accurate assessment of diffusion, especially for ablative simulations [25]. Two such approaches are presented next in this section. For the following expressions, the driving force is taken to be only due to gradients of chemical compositions.

Modified Fick's law

Fick's law can be extended by replacing the binary diffusion coefficient term $\mathscr{D}_{ij}$ by an average multicomponent diffusion coefficient D_{im} for the mixture. The resulting expression approximates the diffusion flux as

$$\mathbf{J}_i = -\rho D_{im} \boldsymbol{\nabla} y_i \,, \tag{2.49}$$

where

$$D_{im} = \frac{1 - x_i}{\sum_{j \neq i} \frac{x_j}{\mathscr{D}_{ij}}} \,. \tag{2.50}$$

A correction to this expression can be applied in the form of a Ramshaw projection as follows

$$\mathbf{J}_i = -\rho D_{im} \boldsymbol{\nabla} y_i + y_i \sum_j \rho D_{jm} \boldsymbol{\nabla} y_j \,, \tag{2.51}$$

which ensures that the diffusive mass fluxes sum to zero to satisfy species mass conservation [116]. This is the model currently being used in INCA.

This model essentially treats the species i as the first, and the average of the remaining species as the second component of a binary diffusion. One of the underlying assumptions in this theory for the derivation of D_{im} implies that species i is moving much faster than all the other species. This approximation was seen to yield good results for trace species, which only constitute a small fraction of the mixture. However, since the model is applied to all species, major errors higher than 20% can occur for more dominant species [126]. Even so, the corrected model has been shown to provide better agreement with higher fidelity models for ablative simulations with mass blowing [1].

Stefan-Maxwell equations

A more rigorous option equivalent to Eq. (2.45) which respects the kinetic theory foundations is to solve the Stefan-Maxwell equations. These equations were originally written for the solution of the mole fraction gradients as

$$\boldsymbol{\nabla} x_i = \frac{M}{\rho} \sum_{j \neq i} \left(\frac{x_i \mathbf{J}_j}{M_j \mathscr{D}_{ij}} - \frac{x_j \mathbf{J}_i}{M_i \mathscr{D}_{ij}} \right) \,. \tag{2.52}$$

Equation 2.52 constitutes a set of linearly dependent equations with an additional constraint by the species mass conservation, $\sum_i \mathbf{J}_i = 0$. In Mutation^{++}, this system can be solved by the direct Cholesky LDL$^{\mathrm{T}}$ decomposition, or iteratively by the Conjugate-Gradient method. Even though the solutions of these equations are known to yield highly accurate results, additional computational resources are required compared to the approximate Fick's law models. Magin and Degrez [72] have shown the efficiency of the iterative Conjugate-Gradient methods in alleviating this drawback for equilibrium air.

2.3.2. Viscosity

The stress tensor appearing in Eq. (2.3) for expressing the flux of momentum is defined as

$$\overline{\overline{\boldsymbol{\tau}}} = \mu \left[\boldsymbol{\nabla} \mathbf{u} + (\boldsymbol{\nabla} \mathbf{u})^{\dagger} - \frac{2}{3} \boldsymbol{\nabla} \cdot \mathbf{u} \overline{\overline{\boldsymbol{I}}} \right] \,, \tag{2.53}$$

where μ is the dynamic (shear) viscosity of the mixture. In this formulation, the effects of bulk (volumetric) viscosity and the chemical pressure are omitted as they usually have small contributions or are difficult to express accurately [117]. Classical method of obtaining the shear viscosity by Sutherland's law is limited only to relatively low temperatures and fails when dissociation begins [87]. This is largely due to the fact that Sutherland's formula assumes approximate parameters for particle collisions, unlike the approach discussed in this context based on precise collision integrals. Instead, the most accurate way is to acquire it from the first-order Laguerre-Sonine polynomial approximation of the Chapman-Enskog expansion as

$$\mu_i = \frac{5}{16} \frac{\sqrt{\pi k_B T m_i}}{\bar{Q}_{ij}^{(1,1)}} \,. \tag{2.54}$$

For a mixture, shear viscosity is the outcome of a linear system given as

$$\sum_j G_{ij}^{\mu} \alpha_j^{\mu} = x_i \,, \tag{2.55}$$

$$\mu = \sum_i \alpha_i^{\mu} x_i \,, \tag{2.56}$$

where the summations are given over heavy species only as, even when they are present, electrons do not contribute to viscosity. G_{ij}^{μ} is the viscosity transport matrix depending on the species compositions and collision integrals. Its explicit form is given by Scoggins [117] based on the work of Magin and Degrez [72].

Solution of this system of equations can be accomplished by classical methods such as constructing a determinant [55] or by simplified mixture rules such as the ones derived by Wilke [134] or Gupta and Yos [52]. The mixture rule used in standalone INCA is the one from Herning and Zipperer [54], written as

$$\mu = \frac{\sum_i \left(\mu_i y_i / \sqrt{M}\right)}{\sum_i \left(y_i / \sqrt{M}\right)} \,. \tag{2.57}$$

This mixture rule is an even simpler version of Wilke's rule as it entirely neglects multicomponent interactions. The semi-empirical mixture rule of Wilke attempts to account for these interactions by a coefficient Φ_{ij} as

$$\mu = \sum_i \frac{y_i \mu_i}{M_i \Phi_{ij}}, \quad \Phi_{ij} = \sum_j \frac{y_j}{M_j} \left[1 + \sqrt{\frac{\mu_i}{\mu_j}} \left(\frac{M_j}{M_i}\right)^{1/4}\right]^2 \left[\sqrt{8\left(1 + \frac{M_i}{M_j}\right)}\right]^{-1} . \tag{2.58}$$

Wilke's rule assumes constant collision integral ratios for all interactions, and the same hard sphere cross sections for all binary collisions. It is often supplied by curve fits calculated by Blottner et al. [12] for species viscosities. Even when Wilke's mixing rule yields acceptable results for nonionized mixtures, despite its simplicity, it has been shown to perform slower than the Gupta and Yos model [97]. Regardless of its other simplifications, Gupta and Yos' mixing rule maintains kinetic theory definitions of collision integrals, and is therefore relatively more accurate as long as ionization in the flow remains weak [87, 114]. Comparison of these results for ablative simulations confirmed the expectations as both simplified models were in agreement at lower speed entry conditions, yet disparities occurred at higher altitudes [1]. An alternative approach for an accurate solution of the complete system is proposed by Ern and Giovangigli [40], which enables quicker solutions with Cholesky $\mathrm{LDL}^{\mathrm{T}}$ decomposition or iteratively by the Conjugate-Gradient method. Magin and Degrez [72] have demonstrated the superiority of the iterative Conjugate-Gradient method in terms of accuracy and robustness compared to other alternatives. Consistent resolutions were also reproduced using Mutation^{++} [117]. The $\mathrm{LDL}^{\mathrm{T}}$ method is the suggested option in Mutation^{++}, and it was chosen for the simulations performed in this study.

2.3.3. Thermal Conductivity

The heat flux term in Eq. (2.4) can be written for the contributions from conduction and mass diffusion as

$$\mathbf{q} = -\lambda \boldsymbol{\nabla} T + \sum_i h_i(T) \rho_i \boldsymbol{\mathcal{V}}_i \,, \tag{2.59}$$

where the first term stems from the Fourier's law with λ as the thermal conductivity of the mixture, and the second term refers to the diffusion of enthalpy. In this expression, the Dufour effect regarding thermal diffusion is usually small and therefore neglected. Thermal conductivity is obtained through a second-order Laguerre-Sonine polynomial approximation of the Chapman-Enskog expansion, and similar to viscosity, it is the solution of a linear system given as

$$\sum_j G_{ij}^{\lambda} \alpha_j^{\lambda} = x_i \,, \tag{2.60}$$

$$\lambda = \sum_i \alpha_i^{\lambda} x_i \,, \tag{2.61}$$

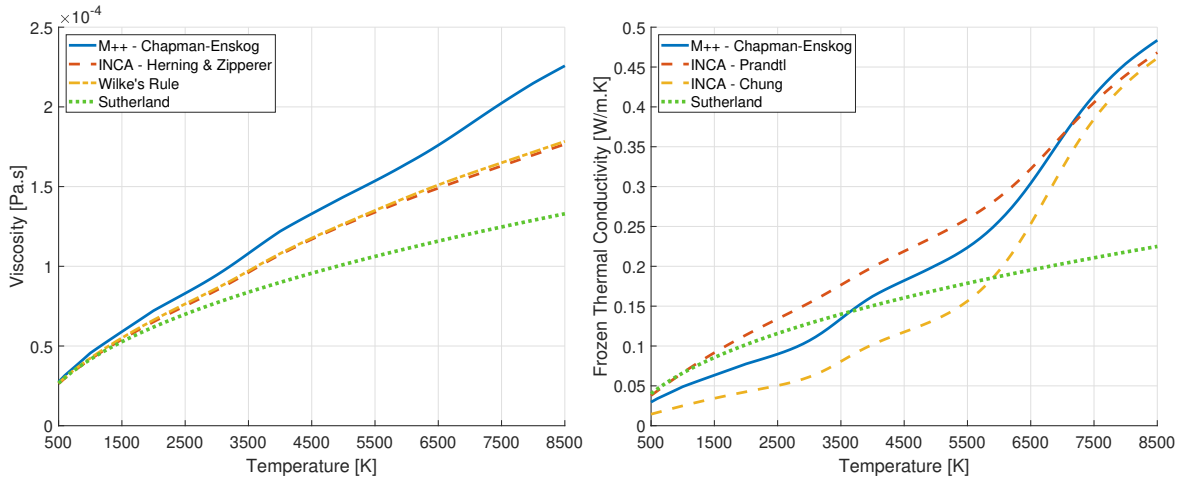

Figure 2.2: Comparison of the transport properties at 0.5 atm in Mutation^{++} and standalone INCA, with the traditional Sutherland's law. Chapman-Enskog results are taken as reference.

where the thermal conductivity transport matrix G_{ij}^{λ} is again a function of species compositions and collision integrals. The discussion presented for viscosity regarding the solution of this system also applies for the thermal conductivity. Standalone INCA obtains thermal conductivity from species Prandtl numbers or through the models suggested by Chung et al. [28] for relatively low temperatures. As with viscosity, both models fall back to the same simple mixing rule of Herning and Zipperer [54] in Eq. (2.57).

Under thermal nonequilibrium, the influence of additional energy modes can also be included, as will be shown in Section 2.5. Thermal conductivities of internal energy modes are computed by the Eucken correction [55], which assumes internal modes to be separable and in thermodynamic equilibrium. For any internal energy mode M, the thermal conductivity is such that

$$\lambda^{\mathrm{M}} = \sum_i \frac{\rho_i c_{p,i}^{\mathrm{M}}}{\sum_j x_j / \mathscr{D}_{ij}} , \tag{2.62}$$

where $c_{p,i}^{\mathrm{M}}$ are the internal specific heats obtained by substituting internal enthalpies and temperatures in Eq. (2.15). The mixture thermal conductivity is simply the sum of all contributions.

Comparison of mixture viscosities and thermal conductivities with respect to temperature at 0.5 atm for the standard 5-species air mixture is given in Fig. (2.2). Here, the multicomponent Chapman-Enskog method in Mutation^{++}, Herning and Zipperer's mixture rule in standalone INCA, Wilke's rule and the traditional Sutherland's law is compared. With the Chapman-Enskog formulation being the most theoretically accurate model, it is taken as the reference result. It can be deduced that the traditional Sutherland's law is clearly not applicable for high temperature regimes. Mixture rule of Herning and Zipperer is a highly simplified model without any multicomponent interactions, consequently it performs poorly as the temperature increases. The difference between Wilke's rule and that of Herning and Zipperer is small for this simple mixture as charged or ablative species are absent. It is important to remark that the species mass fractions here were directly acquired from Mutation^{++}, and was common for all models. However, for the actual computation of the species properties, Mutation^{++} results relied on its collisional database and the others used INCA's Neufeld approximation. Since the mixture rule of Herning and Zipperer is behaving similar to Wilke's rule in this comparison, it emphasizes that the deficiency underlying standalone INCA calculations is in fact not entirely due to the simplified mixture rule, but also due to the lack of an accurate database for collision integrals. These discrepancies were anticipated in Section 2.3 and are expected to amplify when collisions between more complex particles are considered. The significance of the difference in thermal conductivities will become clearer through the results in Chapter 4, as these differences directly affect the computed heat fluxes. One major aspect which can be observed from these plots is the onset of dissociation, signaled by the larger slopes around 3500 K and 6500 K for O_2 and N_2, respectively. Note that these dissociation temperatures are slightly lower compared to the ones stated in Section 1.2 since those ones were for 1 atm condition.

Generally, increasing pressure inhibits dissociation reactions [3]. Additionally, an important aspect to note here is that the degree at which the different models respect this physical variation as with the Chapman-Enskog formulation varies significantly. This also hints at the level of fidelity of each model.

2.4. Chemical Kinetics

Describing the complex nonequilibrium processes in a hypersonic medium necessitates accurate consideration of the underlying chemistry. To that end, this section provides closure to the chemical source term $\dot{\omega}_i$ in Eq. (2.2).

Reactions that occur in a single step are referred to as elementary reactions, and any elementary reaction r can be written in the following general form

$$\sum_i \nu_{i,r}^{'} S_i \rightleftharpoons \sum_i \nu_{i,r}^{''} S_i \,, \tag{2.63}$$

where $\nu_{i,r}^{'}$ term in the reactants and $\nu_{i,r}^{''}$ term in the products are the stoichiometric coefficients of the forward and backward reactions, respectively, for the i^{th} species denoted by the dummy variable S_i. An elementary reaction is reversible and can proceed in both directions.

To arrive at an expression for the chemical source term, the rates at which each reaction is occurring needs to be evaluated. According to the law of mass action [133], the molar rate-of-progress for a reaction r is given by

$$\mathfrak{R}_r = k_{f,r} \prod_i \left(\frac{\rho_i}{M_i}\right)^{\nu_{i,r}^{'}} - k_{b,r} \prod_i \left(\frac{\rho_i}{M_i}\right)^{\nu_{i,r}^{''}} \,, \tag{2.64}$$

which represents the net rate of species mole production or destruction with $k_{f,r}$ and $k_{b,r}$ as the forward and backward reaction rate coefficients, respectively [117]. The forward and backward reaction rates can be linked by considering the case of chemical equilibrium. The definition of chemical equilibrium given in Section 1.2 is based on the idea that these forward and backward reaction rates are in balance. Hence, in chemical equilibrium $\mathfrak{R}_r$ becomes zero, and an equilibrium constant $K_{eq,r}$ can be defined as

$$K_{eq,r} = \frac{k_{f,r}}{k_{b,r}} = \prod_i \left(\frac{\rho_{eq,i}}{M_i}\right)^{\left(\nu_{i,r}^{''} - \nu_{i,r}^{'}\right)} \,, \tag{2.65}$$

and it is related to the change in Gibbs free energy given in Eq. (2.13) as

$$K_{eq,r} = (\mathcal{R}T)^{-\sum_i \left(\nu_{i,r}^{''} - \nu_{i,r}^{'}\right)} \exp\left(-\sum_i \frac{\left(\nu_{i,r}^{''} - \nu_{i,r}^{'}\right) g_i / M_i}{\mathcal{R}T}\right) \,. \tag{2.66}$$

Since the equilibrium constant is provided by thermodynamics, by knowing one of the reaction rates, the other can be retrieved from Eq. (2.65). In this work, the forward reaction rate coefficient is calculated according to a modified Arrhenius rate law written as

$$k_{f,r} = A_r T^{\beta_r} \exp\left(-\frac{(E_a)_r}{\mathcal{R}T}\right) \,, \tag{2.67}$$

where the pre-exponential constants A and β, and the activation energy E_a for each reaction are usually obtained empirically or through theoretical expressions from quantum mechanics [117]. Hence, $\mathfrak{R}_r$ in Eq. (2.64) can be calculated for any reaction defined in the mixture. Considering the weighted contribution of all reactions yields the chemical source term for a species i as

$$\dot{\omega}_i = M_i \sum_r \left(\nu_{i,r}^{''} - \nu_{i,r}^{'}\right) \mathfrak{R}_r \,. \tag{2.68}$$

Third-body reactions involve an inert species, which only participates in the exchange of chemical energy in a reaction, while remaining unchanged in the reactants and products. These reactions can be considered by simply assuming that the law of mass action in Eq. (2.64) can be scaled by third-body efficiency factors.

In case of thermal nonequilibrium, an important thing to note is that the formulations in Eq. (2.66) and Eq. (2.67) strongly depend on the selection of the appropriate temperature. The equilibrium rate coefficients are generally scaled by a parameter, which is a function of the temperature belonging to the relevant thermal bath. The choice of the thermal bath is not straightforward, but available for certain reactions [117].

In INCA and Mutation^{++}, species to be considered in the mixture and the reaction mechanisms they are permitted to undertake are specified by user inputs. Arrhenius rate law constants can be explicitly provided as well. These mechanism inputs are then checked for stoichiometric inconsistencies and erroneous entries. In addition to the net species production rates $\dot{\omega}_i$, Mutation^{++} provides analytical expressions for the Jacobian of the source terms

$$\mathfrak{J}_{ij} = \frac{\partial \dot{\omega}_i}{\partial \rho_j} \,, \tag{2.69}$$

which are required to efficiently advance the solution in time as will be discussed in Section 3.2.

2.5. Thermal Nonequilibrium

Excitation of the species internal energy modes as discussed in Section 2.2.2, renders the single temperature assumption invalid. Calculation of species energies for each mode can be accomplished in a number of ways with varying degrees of accuracy and complexity. The most rigorous option is to track each energy level individually, which requires an overwhelming amount of computational resources. To alleviate this problem, energy partitioning models are proposed, which describe the way the energy is partitioned among the energy levels of a particle.

One such class describing thermal nonequilibrium considers the multi-temperature models. Multi-temperature models are based on the assumption that the internal energy modes can be decoupled, such that each mode is governed under a Boltzmann distribution at a representative temperature of its own. A common example to one of these models that is provided by Mutation^{++} is Park's two-temperature model [100], which has also been the most widely adopted method among the tools reviewed in Section 1.3. This model assumes that the translational and rotational modes are in thermal equilibrium under a translational temperature $T^{\mathrm{T}} = T^{\mathrm{R}}$, while vibrational and electronic modes are in thermal equilibrium under a vibrational temperature $T^{\mathrm{V}} = T^{\mathrm{E}}$. For the latter temperature, an additional internal energy equation can be formed as

$$\frac{\partial \rho e^{\mathrm{V}}}{\partial t} + \boldsymbol{\nabla} \cdot \left(\rho \mathbf{u} e^{\mathrm{V}} + \mathbf{q}^{\mathrm{V}} \right) = \dot{\Omega}^{\mathrm{TV}} + \dot{\Omega}^{\mathrm{CV}} \,, \tag{2.70}$$

where $\dot{\Omega}^{\mathrm{TV}}$ is the source term for energy exchange between the two modes, $\dot{\Omega}^{\mathrm{CV}}$ is the source term for energy transferred by chemical reactions, and $\mathbf{q}^{\mathrm{V}}$ is the vibrational temperature heat flux defined as

$$\mathbf{q}^{\mathrm{V}} = -\lambda^{\mathrm{V}} \boldsymbol{\nabla} T^{\mathrm{V}} + \sum_i h_i(T^{\mathrm{V}}) \rho_i \boldsymbol{\mathcal{V}}_i \,, \tag{2.71}$$

where λ^{V} is obtained from the Euken correction given in Eq. (2.62) and species thermodynamic properties belonging to the vibrational energy bath are obtained from the RRHO database described in Section 2.2.3.

In Eq. (2.70), the first energy exchange term $\dot{\Omega}^{\mathrm{TV}}$ describes how the system relaxes to equilibrium through collisions. A relaxation time scales the difference in energies between the two states as they equilibrate. In this study, the Landau-Teller form is used as

$$\dot{\Omega}^{\mathrm{TV}} = \sum_m \dot{\Omega}^{\mathrm{TV}}_m = \sum_m \rho_m \frac{e^{\mathrm{V}}_m(T^{\mathrm{T}}) - e^{\mathrm{V}}_m(T^{\mathrm{V}})}{\tau^{\mathrm{TV}}_m} \,, \tag{2.72}$$

where the summations are over each molecule m, and τ^{TV}_m is the relaxation time according to Park's correction to the expression proposed by Millikan and White [100]. The second source term $\dot{\Omega}^{\mathrm{CV}}$ refers to the variation of vibrational energy due to chemical reactions. This term is related to the production rate of molecules as

$$\dot{\Omega}^{\mathrm{CV}} = \sum_m \dot{\Omega}^{\mathrm{CV}}_m = \sum_m e^{\mathrm{V}}_m \dot{\omega}_m \,. \tag{2.73}$$

This formulation corresponds to a non-preferential dissociation model assuming that the probability of a molecule dissociating from any vibrational state is the same. That is, a molecule loses or gains all of its average vibrational energy when it undergoes a dissociation or recombination reaction. Preferential models, such as the one from Marrone and Treanor [76], consider dissociation to be more probable for higher vibrational levels, but they are not yet implemented in Mutation^{++}.

The global energy equation in Eq. (2.4), which is written for the summation of all energy modes $e = \sum_{\mathrm{M}} e^{\mathrm{M}}$, needs to be modified as well with the following heat flux considering the contribution from the vibrational mode as

$$\mathbf{q} = -\lambda^{\mathrm{T}} \boldsymbol{\nabla} T^{\mathrm{T}} - \lambda^{\mathrm{V}} \boldsymbol{\nabla} T^{\mathrm{V}} + \sum_i h_i(T^{\mathrm{T}}, T^{\mathrm{V}}) \rho_i \boldsymbol{\mathcal{V}}_i \,. \tag{2.74}$$

Solution of these modified governing equations yields an additional energy density for the vibrational energy bath. Then, for each mode, their respective energy equations can be solved using a Newton-Rhapson iterative procedure to obtain the two temperatures for the mixture. This temperature duality demands temperature-dependent relations in the previous sections to have variations based on the thermal bath they are being computed for. Generally, the effective temperature to calculate the rate coefficient of a molecular dissociation reaction is computed as a geometric average of the two temperatures as $\sqrt{T^{\mathrm{T}} T^{\mathrm{V}}}$. These are taken into account within Mutation^{++} and the properties belonging to each energy mode are found distinctly [117].

One of the biggest assumptions adopted in this model aims to decrease the computational cost by assuming that the species equilibrate under the two mixture temperatures, instead of having individual temperatures for each energy mode. The validity of this assumption falters for cases considering large deviations from equilibrium, such as regions right after a shock relevant for radiation calculations as observed by Panesi et al. [98]. Under those conditions, rotational temperatures have shown significant departure from translational temperatures until equilibrating downstream. These limitations are confirmed by Park [103], where he discusses the applicability of the model two decades after its first conception.

When sufficient amount of collisions to relax the system to thermodynamic equilibrium do not occur, the system cannot be represented under a temperature definition. More advanced partitioning models are needed which require larger number of equations to be solved. These include state-specific models where some modes are taken in nonequilibrium as pseudo-species and the remaining ones are assumed to be in thermodynamic equilibrium. A more rigorous option is to model by a state-to-state (STS) approach, which treats all internal energy levels as pseudo-species [98]. These models require quantum chemistry calculations for evaluating accurate rate coefficients, and with additional pseudo-species, the amount of conservation equations becomes numerous. An alternative method is to employ coarse-grain models, which respect the coupled nature of energy modes by grouping similar energy levels into bins from *ab initio* STS data [74, 93]. This approach does not necessarily alleviate the computational cost, but it preserves the chemical basis of nonequilibrium effects, and the resolution can be arbitrarily improved according to a binning process [117].

2.6. Gas-Surface Interactions

In highly excited flows, prescribing the surface state only by means of simplified surface conditions, such as a prescribed temperature or heat flux, is insufficient in modeling the complex interactions. Considering accurate gas-surface interaction phenomena is crucial for correctly evaluating the heat flux towards the vehicle by accounting for surface catalysis and ablative mass blowing.

In their review of ablative material response models and simulation tools, Lachaud et al. [66] notes Aerotherm's report from 1968 [61] as the first open literature publication presenting a detailed investigation regarding tools for designing in high-enthalpy conditions. They go on to state that contemporary design tools are successors of the codes developed by Aerotherm, often with simplifications alongside improvements. The research and development oriented tools are generally more advanced, but lack the robustness for design applications. An example of a simplification is that, as opposed to high-fidelity codes, most design codes have refrained from tracking species production rates, but focused on the average mass production by assuming that chemical equilibrium holds. Consequently, design codes are employed multiple times to estimate the interactions along a vehicle's trajectory, where more advanced codes consider the most critical point in the trajectory, such as when peak heating occurs.

The two main processes that govern the heterogeneous chemistry reactions at the gas-surface interface are catalysis and ablation. The following section reviews relevant approaches to model these interactions.

2.6.1. Modeling Catalysis and Ablation

An introduction to the concept of a surface as a catalyst and a surface chemically decomposing under ablation was provided in Section 1.2. Many different approaches have been developed over the years to simulate these phenomena according to empirical observations. Earliest catalysis treatments disregarded the effect of diffusion and assumed full recombination of species at the surface. This is currently referred to as the super-catalytic condition and it generally lacks the physical basis of more appropriate models. A common way of treating catalytic surface reactions has been suggested by Goulard [50], and it is referred to as the effective catalytic recombination coefficient or "gamma" model in literature. This model is established on the experimentally found γ parameter which is defined as a ratio of the flux of species recombining at the surface $\mathcal{M}_{i,rec}$ to the flux of species impinging on the surface $\mathcal{M}_{i,imp}$ [6]. To write it explicitly,

$$\gamma_i = \frac{\mathcal{M}_{i,rec}}{\mathcal{M}_{i,imp}} , \tag{2.75}$$

where $\mathcal{M}_{i,imp}$ is given by

$$\mathcal{M}_{i,imp} = n_i \sqrt{\frac{kT_w}{2\pi m_i}} , \tag{2.76}$$

if a Maxwellian particle distribution is assumed at the wall, or by

$$\mathcal{M}_{i,imp} = n_i \sqrt{\frac{kT_w}{2\pi m_i}} + \frac{\mathbf{J}_i \cdot \mathbf{n}_w}{2m_i} , \tag{2.77}$$

if a Chapman-Enskog perturbation is considered [4]. Here, n_i is the number density, T_w is the temperature at the wall and $\mathbf{n}_w$ is the unit normal vector to the surface. From these relations, a catalytic reaction rate term can be formulated as

$$\dot{\omega}_{i,cat} = \gamma_i m_i \mathcal{M}_{i,imp} . \tag{2.78}$$

This ratio describes the reaction efficiency in determining the mass production rate of species at the surface. A γ value of unity corresponds to a fully catalytic surface, where all the particles impinging on the surface recombine. Conversely, when γ is equal to zero, the surface is non-catalytic and no reactions occur at the surface. All intermediate states are referred to as partially catalytic. Catalysis is approximated as a recombination reaction for a single species by neglecting the elementary reactions. Even though variants of this model have been widely applied in the aerothermodynamics community, it is limited by severe assumptions. Unlike reality, most of the reactions are taken to be irreversible, and the heat associated with these reactions are assumed to transfer to the surface completely, without storing a portion of the energy within the products [117].

A high-fidelity alternative is to use finite-rate chemistry models, where essentially the reactions are modeled in multiple steps at a finite rate often governed by an Arrhenius rate relation. In the finite rate chemistry model, gaseous species participate in interactions with surface sites. Four types of interactions may occur: adsorption, desorption, Eley-Rideal interaction, and Langmuir-Hinshelwood interaction. Adsorption describes the mechanism when a gaseous species forms a chemical bond with an active surface site. The rate of this reaction depends on the probability of an impinging atom to become adsorbed. Desorption refers to the opposite mechanism, in which the chemical bond is broken with enough activation energy to release the species from the surface. In an Eley-Rideal mechanism, an impinging species recombines with an adsorbed species and the product immeditately breaks off from the surface. Finally, Langmuir-Hinshelwood interaction describes a similar process, where the recombination occurs between two adsorbed species. Details of these reactions, and the implementation of both the γ and finite-rate chemistry models in the Mutation^{++} library are discussed by Bellas-Chatzigeorgis et al. [7].

Different approaches also exist for modeling ablation. A common method used by Milos et al. [23, 85] is based on B' curves. Derivation of this B' parameter assumes that the heat and mass transfer analogy holds, such that the nondimensional mass blowing and heat fluxes given by

$$C_M = \frac{\dot{m}}{\rho_e u_e B'} , \quad C_H = \frac{q_w}{\rho_e u_e h_e} , \tag{2.79}$$

satisfy $C_M \simeq C_H$, where $\dot{m}$ is the mass flux, subscript e denotes conditions at the boundary layer edge, and subscript w is for the wall conditions [21]. Assuming a Fickian diffusion, constant c_p, and a Lewis number of unity, the surface gradient quantities can be approximated according to boundary layer theory to obtain an expression for B' as

$$B' = \frac{\dot{m}}{\rho_e u_e C_M} \approx \frac{\rho D_{wm} c_p}{k} \frac{y_{c,w}}{1 - y_{c,w}} = \frac{1}{Le} \frac{y_{c,w}}{1 - y_{c,w}} \approx \frac{y_{c,w}}{y_{a,w}} \,. \tag{2.80}$$

Hence, B' is a nondimensional mass flux defined as the ratio of the mass fraction of gaseous carbon species to air species at the local wall conditions. Values for B' are often tabulated and by utilizing this data mass blowing rates can be specified. A drawback of this method is that the chemical composition of the mixture at the wall is disregarded. By assuming equilibrium at the surface, ablation rates are often overpredicted [84]. Moreover, the method requires a separate blowing factor to account for the cooling due to outgassing. Similar to catalytic reactions, a remedy is provided by implementing the more intricate finite-rate chemistry model for ablation [24], as indicated by Candler [17]. Arrhenius type functions are formulated for oxidation, nitridation, and sublimation reactions, based on empirical constants such as the one for carbon from the early work of Park [99], to formulate a similar expression to that given in Eq. (2.78) for ablation. By doing so, chemical nonequilibrium at the surface is respected, and the effect of blowing can inherently be considered by a steady-state approach, as will be presented in this section. Instead of the classical model from Zhluktov and Abe [140], the finite-rate ablation model implemented in Mutation^{++} is based on recent measurement data acquired from molecular beam experiments conducted for identifying individual reaction mechanisms [5]. In the current study, elementary reactions are not considered. Instead, reaction rate probabilities for characteristic chemical processes are used to compute the ablative reactions. These probabilities could be defined by empirical constants, as temperature dependent Arrhenius relations or by other relevant thermochemical properties [5]. This approach is known to yield accurate results and it has been employed by similarly advanced tools [25, 91].

Several frameworks have been considered by researchers and reviewed by Schrooyen [116] to numerically implement these approaches by simulating the diverse aspects of ablative materials. These configurations mainly revolve around the idea of coupling a flow solver with a material response code to some degree of cooperation. A standalone material solver suffers from simplified boundary conditions, which model the absent fluid by means of separate inviscid flow field solutions. Other thermodynamic surface conditions are usually acquired from semi-empirical relations. Coupling the material code with a flow solver alleviates these deficiencies to an extent, based on the strength of the coupling. A weak coupling generally means that both codes are developed and operate independently such that they only exchange information at predefined time steps [77]. Material is often simulated as having a one-dimensional response, and interior flows are modeled by Darcy's law. More involved implementations provide detailed information regarding the interior of the material which allows establishing a momentum balance at the interface to simulate flow directions of the blowing gases and pressure gradients inside a porous material. As a further advancement, strongly coupled systems share the computational domain between the two solvers, and are therefore able to simulate both aspects in a time-accurate manner [2, 26]. However, implementation of this architecture requires meticulous care since both codes need to be modified thoroughly. These frameworks have the material response at their core. At the other end of the spectrum, an ablative boundary condition implementation preserves the flow field, and behaves like any other boundary condition within a CFD solver by disregarding the material code. In this method, the material response is modeled by surface balances at the gas-surface interface, and the flow field is obtained by numerically solving the Navier-Stokes equations. This is the approach adopted in this study.

A crucial aspect of ablating heat shields is the recession of the surface due to mass loss. This unsteady shape change alters the flow field, and consequently has an impact on the aerodynamic performance of the vehicle. From the definitions that will be given in this chapter, it is possible to calculate the recession speed of the discretized surface from the mass blowing rate of species and the surface density. The challenge is to impose this recession rate to the gas-surface interface, in a way that the numerical solution is compatible with the movement. Furthermore, the frequency of this mesh adaptation also has an impact on the accuracy and computational cost of the simulations. This process may be carried out in an uncoupled way by regenerating the mesh every time it is requested [65] or during run-time through a coupled approach [78]. Care must be taken for large recession rates to avoid unphysical jumps

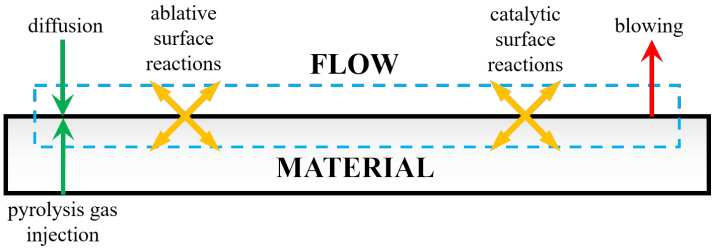

Figure 2.3: Surface species mass balance for an ablating material. Adapted from Turchi [129].

or numerical instabilities. Recession of the surface is neglected in the cases considered in Chapter 4, but it is seen as a provisional continuation of this work.

Before proceeding with the theory of surface balances, a note on thermal nonequilibrium is befitting here. Effects of thermal nonequilibrium are relatively minor [2] and often neglected [67] for cases involving gas-surface interaction. The main reasons behind this simplification are twofold. Firstly, thermal nonequilibrium is mostly dominant just after the shock, since the internal energy modes equilibrate as they approach stagnation. This post-shock relaxation towards the body is ensured as long as very low pressures, which does not allow for sufficient number of collisions to occur, are avoided [53]. Secondly, contemporary GSI models, such as the one considered in this study, inherently assume thermal equilibrium at the wall. Research on this subject through the application of coarse-grained STS models have suggested an increase in overall heat flux due to the interaction between catalysis and thermal nonequilibrium [6]. Another recent study investigated the portion of the recombination energy stored by the internal modes and on the surface [8]. It was found that the common approach of assuming all the energy to be deposited on the surface was reasonably valid, and had no major impact on the heat flux. The influence of any deviation from thermal equilibrium on GSI is part of an ongoing work at VKI.

2.6.2. Mass and Energy Balances

In the present analysis, the gas-surface interaction modeling is performed through a dedicated ablative boundary condition implemented in INCA by means of the GSI module [7] within Mutation^{++}. Thermal equilibrium is assumed at the surface and mass loss due to mechanical degradation is neglected.

Ablation modeling approaches which perform without the need of a material response code, initially considered an isothermal ablative boundary condition assumption for the gas-surface interface [10, 16]. Under surface chemical equilibrium, species compositions at the wall are computed for a given wall pressure found through the flow solution. A mass balance at the interface was then solved to calculate the mass blowing and the associated recession rates. The next evolution came with the implementation of an energy balance equation at the interface, which abolished the isothermal wall assumption by solving for the wall temperature [11]. Then, the equilibrium assumption was replaced with a finite-rate chemistry model by Chen and Milos [25], to better model the reactions between the flow and the surface species, such as oxidation, nitridation, and sublimation, which govern the physicochemical environment.

Development of a formula for the species mass and energy balances can be achieved by considering a thin lamina approach [129]. Balances based on this approach are shown by a control volume encompassing the immediate vicinity of the surface for mass in Fig. (2.3) and for energy in Fig. (2.4).

In order to establish a balance for the mass of species, the effect of the pyrolysis gas and surface ablation must be considered, since these processes inject additional mass into the flow. Unlike for a catalytic case, where the flow speed normal to the surface v is zero, for the ablative case, there exists a blowing velocity due to the outgassing of the chemical products. This velocity gives rise to a convective flux term $\rho_i v$ in addition to the diffusive flux $\rho_i \mathcal{V}_i$ due to the concentration gradients. These fluxes are balanced by a species surface source term $\dot{\omega}_{i,w}$, which accounts for all the surface reactions shown in Fig. (2.3), and a term for mass blowing. For a single species i this balance is written as

$$(\rho_i v)_w + (\rho_i \mathcal{V}_i)_w = \dot{\omega}_{i,w} + \dot{m}_g y_{i,g} \,. \tag{2.81}$$

Summing up this expression for all species in the mixture yields the global surface mass balance as

$$(\rho v)_w = \dot{m}_c + \dot{m}_g = \dot{m} \,, \tag{2.82}$$

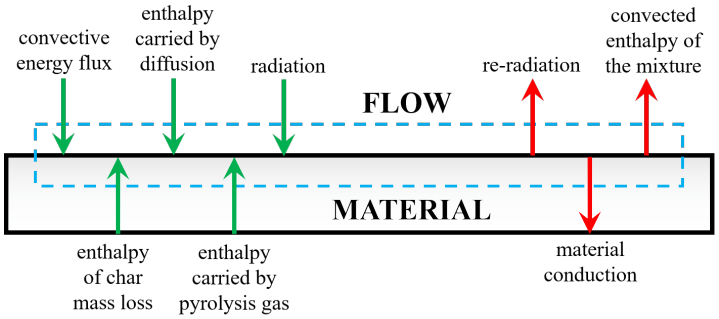

Figure 2.4: Surface energy balance for an ablating material. Adapted from Turchi [129].

where $\dot{m}_c = \sum_i \dot{\omega}_{i,w}$ is the char blowing rate. With an ablative surface model correctly accounting for the surface reactions of the species present in the flow field, the surface mass balance can be numerically solved for the total mass loss. A suitable ablation model can provide a closure to the mass balance by calculating the chemical source terms in Eq. (2.81), provided that detailed knowledge on chemical interactions between the flow, pyrolysis gas, and solid surface is available. Once the mass balance is solved, the velocity of the gas blowing out of the surface is given by

$$v_{blow} = \frac{\dot{m}}{\sum_i \rho_i} , \tag{2.83}$$

and the speed at which the surface is recessing can be computed as

$$v_{surf} = \frac{\dot{m}}{\rho_s} , \tag{2.84}$$

where ρ_{solid} is the density of the surface material.

Similarly, a global energy balance can be established. Regarding Fig. (2.4), a condition can be proposed for a state such that by heat conduction and blowing gas exertion, all the energy fluxes arriving at the surface due to the flow is ensured to dissipate. If this condition can be satisfied, then energy balances for a reference frame fixed to an ablating surface under recession yields

$$\lambda_w \left.\frac{\partial T}{\partial r}\right|_w - \sum_i \left(\rho_i h_i \mathcal{V}_i\right)_w + \dot{q}_{rad_{in}} + \dot{m}_g h_g + \dot{m}_c h_c = \dot{q}_{rad_{out}} + (\rho h v)_w + \dot{q}_{cond,s} , \tag{2.85}$$

where r is a normal distance from the surface, and the terms represent from left to right: fluid thermal conduction, diffusion of enthalpy, ambient radiation, energy which is brought to the surface by the blowing gas and recession, surface radiation, convected enthalpy of the mixture (free-stream gas, blowing gas and surface ablation products), and conductive heat flux through the solid material. All variables are taken normal to the surface.

In this current formulation, an external radiative heat flux is not considered. Instead, a constant integral emissivity for the surface ϵ_s is obtained empirically to express the net radiative heat flux according to the Stefan–Boltzmann law as

$$\dot{q}_{rad,net} = \dot{q}_{rad,out} - \dot{q}_{rad,in} = \sigma \epsilon_s \left(T_w^4 - T_{env}^4\right) , \tag{2.86}$$

with T_{env} as the temperature of the surrounding environment.

The conductive heat flux term in Eq. (2.85) cannot be determined from CFD simulations without a dedicated material solver. This term can be set to zero for a radiative equilibrium energy balance. However, this simplification is often not justified as the wall temperature strongly varies temporally and spatially [85]. For an alternative formulation, consider the energy conservation equation for the solid phase of a planar surface receding at a constant speed $\dot{s}$ with respect to a reference frame attached to the surface of the material, written as

$$\frac{\partial}{\partial t}\left(\rho_s h_s\right) = \frac{\partial}{\partial r}\left(\lambda_s \frac{\partial T_s}{\partial r}\right) - \dot{s}\frac{\partial}{\partial r}\left(\rho_s h_s\right) - \frac{\partial}{\partial r}\left(\dot{m}_g h_g\right) , \tag{2.87}$$

where from left to right the terms refer to the variation of sensible energy in time, conduction through the material, convection due to recession, and energy released by the blowing gas [61]. If the material in consideration is assumed to be thick enough so that its back surface maintains its initial temperature and virgin material density ρ_v, while the density at the wall interface remains equal to the charred material density ρ_c, then, Eq. (2.87) can be integrated between the receding and back surfaces to obtain

$$\dot{q}^{ss}_{cond,s} = \lambda_{s,w} \left.\frac{\partial T}{\partial r}\right|_s = \dot{s}\left(\rho_{c,w} h_{c,w} - \rho_{v,in} h_{v,in}\right) + \dot{m}_g h_g \,. \tag{2.88}$$

This expression is valid when the temperature profile within the material is time-independent, that is, the material has reached a steady-state (ss) condition [129]. Hence, Eq. (2.88) can be substituted for the surface conduction term in Eq. (2.85) to express an energy balance at steady-state which can be numerically solved for the wall temperature.

Another consequence of the steady-state assumption is that it allows establishing a relation between the char and pyrolysis blowing rates, which would have otherwise required a material response code to determine. Consider the recession rates of the surface and virgin layer, respectively:

$$\dot{s}_c = \frac{\dot{m}_c}{\rho_c} \quad , \quad \dot{s}_v = \frac{\dot{m}_g}{\rho_v - \rho_c} \,. \tag{2.89}$$

Under the steady-state assumption, the thickness between these surfaces are preserved as they recess together at the same rate. This leads to the powerful relation derived by Turchi [129] under the ratio φ of the pyrolysis gas mass flux to the char mass flux as

$$\varphi = \frac{\dot{m}_g}{\dot{m}_c} = \left(\frac{\rho_v}{\rho_c} - 1\right) \,, \tag{2.90}$$

which quantifies the pyrolysis gas mass flux, once the virgin and char material densities are provided. This density ratio can be determined experimentally for a given material. Then, the resulting relation can be substituted into Eq. (2.82) to obtain the total mass loss when the effects of pyrolysis are present.

3

Numerical Methods

This chapter deals with the framework the equations in Chapter 2 are embedded in, that is, the numerical solver computing the flow itself. The methodology behind the numerical approaches chosen in this study is presented in the following sections.

3.1. Mathematical Model

Simulating the physicochemical phenomena of atmospheric entry is an elaborate challenge. Throughout the EDL sequence, the vehicle goes through various different conditions. One variable is the mean free path of the system, defined as the average distance traveled by a particle before it experiences a collision. A large mean free path corresponds to a low-density flow present in the outer atmosphere. Hence, evaluating the impact of each individual particle becomes important. In this rarefied flow regime, the assumptions of continuum flow break down, and Navier-Stokes equations become unreliable. Instead, molecular dynamics simulations should be utilized such as DSMC methods. As the vehicle proceeds to descent, it submerges into a denser environment. The mean free path is smaller, hence Navier-Stokes simulations are valid. The limits of this continuum breakdown are established by the Knudsen number defined as the ratio of mean free path to a characteristic length [3]. As the current applications exhibit sufficiently low Knudsen numbers, Navier-Stokes equations are applicable.

The compressible Navier-Stokes equations given in Chapter 2 can be summarized in

$$\frac{\partial \mathbf{U}}{\partial t} + \boldsymbol{\nabla} \cdot \mathbf{F}(\mathbf{U}) = \mathbf{S}\,, \tag{3.1}$$

where $\mathbf{U}$ is the vector of conserved variables, $\mathbf{F} = \mathbf{F}_{inv} + \mathbf{F}_{vis}$ is the sum of inviscid and viscous fluxes, and $\mathbf{S}$ is the vector of source terms. Along the x axis, they take the following forms:

$$\mathbf{U} = \begin{bmatrix} \tilde{\rho}_i \\ \rho u \\ \rho v \\ \rho w \\ \rho \tilde{E} \end{bmatrix}, \quad \mathbf{F}_{inv} = \begin{bmatrix} \tilde{\rho}_i u \\ \rho u^2 + p \\ \rho uv \\ \rho uw \\ u(\rho \tilde{E} + p) \end{bmatrix}, \quad \mathbf{F}_{vis} = \begin{bmatrix} \tilde{J}_{\mathrm{x},i} \\ -\tau_{\mathrm{xx}} \\ -\tau_{\mathrm{xy}} \\ -\tau_{\mathrm{xz}} \\ -(\tau_{\mathrm{xx}} u + \tau_{\mathrm{xy}} v + \tau_{\mathrm{xz}} w) + \tilde{q}_{\mathrm{x}} \end{bmatrix}, \quad \mathbf{S} = \begin{bmatrix} \tilde{\dot{\omega}}_i \\ 0 \\ 0 \\ 0 \\ \tilde{\dot{\Omega}} \end{bmatrix}. \tag{3.2}$$

Here, the tilde above the variables indicates that they can be expanded according to the number of species and thermal baths considered; depending on the degree of chemical and thermal nonequilibrium model used to express the flow.

3.2. Numerical Approach

The flow solver considered in this work, INCA, is a high-fidelity finite-volume CFD code capable of exercising the compressible Navier-Stokes equations on three-dimensional block-Cartesian grids with a large number of different discretization schemes. For the purpose of this thesis, high-order WENO schemes with HLLC flux functions are selected to discretize the inviscid terms. Second order centered differences are used for the viscous terms and an explicit third-order Runge-Kutta scheme is selected

for time integration. The code supports MPI and OpenMP parallelization through multi-block domain decomposition. INCA has been successfully used in many applications with a specialization towards simulation of shock-boundary layer interaction [106], trans- and supercritical jet flow [92], reacting shock-bubble interaction [34], and multiphase fuel injection [81].

INCA is equipped with explicit and implicit LES methods and can also perform DNS simulations. However, as numerous trial simulations were made for each case considered in Chapter 4, the computational cost of these high-fidelity LES would have been insurmountable, and infeasible during the time constraints of this thesis. The reasoning behind the large number of trial cases were two fold: firstly, the focus of this project was on the implementation and validation of INCA coupled to the Mutation^{++} library, and secondly, the INCA solver was being extended to atmospheric entry flow regimes, where it had never ventured before. Both of these aspects of the project demanded many iterations on the implementations and encouraged computational experimentation. Therefore, two-dimensional test cases and high-order WENO schemes were used instead.

Weighted essentially non-oscillatory (WENO) schemes offer high-order accuracy in the absence of discontinuities, while ensuring stable and sharp capture in the presence of discontinuities, such as strong shocks. These schemes are suitable for high Mach number flows as they do not rely on numerical filters, limiter functions or artificial viscosity for solutions through discontinuities. The main idea behind WENO schemes is to use a high (e.g. 3rd or 5th) order stencil, which comprises of lower (2nd or 3rd, respectively) order sub-stencils. In regions of smooth flow, the larger stencil is used to reconstruct the solution at both sides of the cell boundaries from a convex combination of sub-stencils. The lower order sub-stencils make use of the cell averaged values and are scaled by linear weight coefficients. When a discontinuity is detected according to the smoothness indicator of Jiang and Shu [59], the influence of the sub-stencil hosting the steep change is diminished through nonlinear weights used to scale the contribution of each sub-stencil in the final approximation. These nonlinear weights are a function of the linear weights and the smoothness parameters. More details and a review of different approaches in using WENO schemes are given by Shu [123]. Once the solution at both sides of a cell boundary is reconstructed, the HLLC approximate Riemann solver is used to compute the associated fluxes [127]. The acoustic wave speeds are selected directly to be the fastest from the local data and Roe-average speeds.

Reacting flow simulations manifest a wide variety of time scales for fluid dynamics and chemical reactions. This often leads to a numerically stiff system of equations, where the selected time step might become unsuitable for progressing the solution, resulting in numerical instabilities. In INCA, 2nd-order accurate Strang time splitting scheme [125] is applied, which separates the stiff chemical source terms from the remaining Navier-Stokes equations, and alternates between the solution of these two sets of equations at half time steps. The expression for the chemical source term reduces to an ordinary differential equation (ODE) and it is solved by the VODE library [15], which is an external, variable-coefficient ODE-solver using fifth-order backward differences. The mass production rates and their analytical Jacobians with respect to species densities as in Section 2.4, are provided to the ODE-solver by Mutation^{++}. This allows for a more efficient evaluation of the derivatives compared to the current implementation in INCA based on finite differences and internally generated Jacobian matrices.

Time stepping for the flow solution is governed by a CFL condition. The explicit third-order Runge-Kutta method from Gottlieb and Shu [49] remains stable by maintaining total variation diminishing characteristics for CFL ≤ 1. In addition to the grid size, the time step selection is restricted by a convective limit based on acoustic wave speeds and a viscous limit based on viscous work, heat conduction, and species diffusion.

For immersed boundaries, common isothermal and adiabatic wall boundary conditions are available in INCA. Mutation^{++} offers reactive surfaces through its GSI module presented in Section 2.6. Implementation of this reacting surface boundary condition is closely linked to the treatment of the fluid-solid interface. To that end, INCA utilizes adaptive mesh refinement for Cartesian grids with a conservative immersed interface method.

3.3. Immersed Boundary Methods

Immersed Boundary methods use numerical grids that do not conform with the shape of the boundaries of the domain. For example, instead of a structured or an unstructured grid that tries to follow the shape of a boundary, Cartesian grids are imposed which are allowed to penetrate the object of interest. This

approach introduced by Peskin [107], alleviates the time-consuming task of setting up a body-conformal grid, and creates a geometrically simple domain for arbitrary shapes even under deformation. The resulting immersed boundary grid is perfectly orthogonal and can be solved through finite-difference, finite-volume, or finite-element methods, while avoiding the use of computationally expensive coordinate transformations or discretization operators. Especially for boundaries under motion, such as recession, immersed boundary methods are much more robust and efficient, since the Cartesian grid is mostly preserved throughout the solution, contrary to the body-conformal grids, where a new grid needs to be generated and adapted to the new shape. Nevertheless, special care must be taken to have sufficient grid resolution near the boundaries, as it is inherently more difficult for these methods to resolve the shape. Consequently, an increase in the Reynolds number requires a larger increase in the number of grid cells for a Cartesian grid as opposed to a similar body-conformal grid. However, depending on the shape of the body, a portion of grid cells may lie within the solid object, which do not require the same treatment as cells in the flow. In general, immersed boundary methods provide a lower operation count per grid point compared to body-conformal grids. A brief introduction is presented here based on the classical review with historical development of these methods by Mittal and Iaccarino [88].

The fundamental issue with immersed boundary methods is imposing the boundary condition appropriately. Initially, a source term in the form of a forcing function is defined within the governing equations, which simulates the presence of the boundary. In literature, two different approaches exist, namely the continuous forcing approach and the discrete forcing approach. In the former one, the forcing function is substituted in the continuous governing equations, which is then discretized on the entire Cartesian grid. In the latter approach, the governing equations are first discretized regardless of the influence of the immersed boundary, then the cells in that vicinity are adjusted according to a forcing operator representing the known boundary conditions.

The continuous forcing approach is independent of the applied spatial discretization, which makes its implementation relatively straightforward. The main drawback of this approach is its inability to conserve mass, momentum or energy at the interface, leading to unphysical losses or gains [27]. The discrete forcing approach discretizes the equations first, before applying the forcing operator. This approach demarcates the fluid and solid regions to avoid solutions within the immersed boundary. The implementation of forcing is closely related to the adopted discretization scheme. Smoothing is applied, and it causes undesirable spread near the boundaries. A more distinct boundary can be captured by adjusting the computational stencil near the immersed boundary. One alternative is using ghost-cells [128], which lie in the solid region, but have at least one neighboring cell in the fluid region. This cell can be used to interpolate the boundary condition information on the immersed boundary. A similar interpolation is used in reconstruction methods [60], to reconstruct the local velocity field near the immersed boundary. Different schemes can be devised with varying accuracies depending on the number of cells they consider while constructing the interpolation.

These boundary assessment concepts are also important for an immersed boundary in motion, where the movement of a decaying interface introduces cells emerging from the solid region. The spreading in continuous forcing methods results in a smooth transition, but in discrete forcing, the cells that are newly added to the fluid domain need to be identified distinctly. Since information from the previous time steps do not exist for these cells, a temporal discontinuity occurs. This can be remedied by merging the unknown cells with adjacent ones or by interpolating values from neighboring cells to obtain an expression for the initial time step preceding the movement.

Contrary to previously described discrete forcing methods, an approach which respects the underlying conservation laws is referred to as the cut-cell finite-volume method. First introduction of this method for inviscid flows is attributed to Clarke et al. [29], and it was later applied to viscous flows by Udaykumar et al. [130] and Ye et al. [139]. In this approach, the fluid cells that are cut by the immersed boundary are reshaped by eliminating their solid counterparts to yield a sharp interface representing the boundary. Then, fluxes of conserved quantities can be computed at the cell faces of the resulting deformed control volumes. This ensures that the conservation laws are satisfied locally and globally [88]. It is noted that the application of this process in three dimensions is nontrivial, as the deformed cell shape becomes more complex.

A major problem in cut-cell methods is that the interface might abruptly divide a cell into a very small fraction of its initial size, which may lead to numerical instabilities for explicit methods, and poor convergence for implicit time integration. From the progression presented by Örley et al. [96], this issue was first remedied by merging these cells with nearby cells. However, the merging process

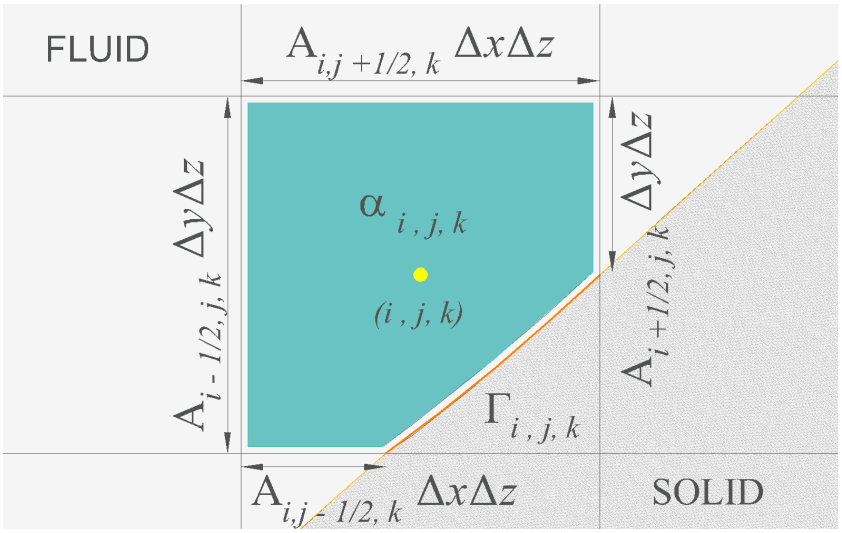

Figure 3.1: Sketch of a two-dimensional cut-cell in the immersed interface method.

involves additional complexities, as it requires the calculation of the fluxes between diagonally adjacent cells and additional modifications of the computational stencil for the cells around the merged cell. A linking approach is proposed by Kirkpatrick et al. [62] where a master and slave pairing is imposed on the cells, which enables the calculation of the fluxes to be the same for both entities such that the computational stencil is kept unchanged. In another approach by Colella et al. [30], a stable yet nonconservative discretization is induced within a conservative scheme, and the differences in the fluxes of conserved quantities are redistributed to nearby cells according to mass weighting. The cell-linking and flux distribution approaches are combined through a mixing operation by Hu et al. [57] for two-dimensional compressible flows. Meyer et al. [83] proposed an improvement on this by including the diagonal cells for mixing as well. This conservative mixing procedure is considered in the present work for the treatment of cut-cells having volume fractions smaller than a chosen threshold.

INCA hosts a unique immersed interface method employing sub-cell triangulation instead of the level-set cut-cell technique, as explained in the following section.

3.3.1. Conservative Immersed Interface Method with Cut-elements

Meyer et al. [83] proposed a conservative second-order accurate immersed interface method for incompressible flows based on a level-set technique sketched in Fig. (3.1). For a given cell with the geometric indices (i, j, k), the fluid and solid domains are demarcated by the interface $\Gamma_{i,j,k}$. The deformed faces of the cell are scaled by the face aperture parameter $A_{i,j,k}$. The fluid volume fraction of a cell is given by $\alpha_{i,j,k}$, such that the effective fluid volume is equal to $(V_f)_{i,j,k} = \alpha_{i,j,k}\Delta\mathrm{x}\Delta\mathrm{y}\Delta\mathrm{z}$.

Proceeding with the finite volume methodology and integrating the convective part of Eq. (3.1) over the fluid domain for a time step $\Delta t = t^{n+1} - t^n$ yields

$$\int_{t^n}^{t^{n+1}} \left[\int_{V_f} \frac{\partial \mathbf{U}}{\partial t}\, dV + \int_{V_f} \boldsymbol{\nabla} \cdot \mathbf{F}(\mathbf{U})\, dV \right] dt = 0\,. \tag{3.3}$$

Applying Gauss' theorem gives

$$\int_{t^n}^{t^{n+1}} \left[\int_{V_f} \frac{\partial \mathbf{U}}{\partial t}\, dV + \int_{S_f} \mathbf{F}(\mathbf{U}) \cdot \mathbf{n}\, dS \right] dt = 0\,, \tag{3.4}$$

where S_f is the wetted surface of a given cell. Then, defining a volume average for the conserved variables of a cell as

$$\overline{\mathbf{U}}_{i,j,k} = \frac{1}{\alpha_{i,j,k} V_{i,j,k}} \int_V \mathbf{U} dV\,, \tag{3.5}$$

where $V_{i,j,k}$ is the total volume of the cell; the three-dimensional discretization of Eq. (3.4) on a Cartesian

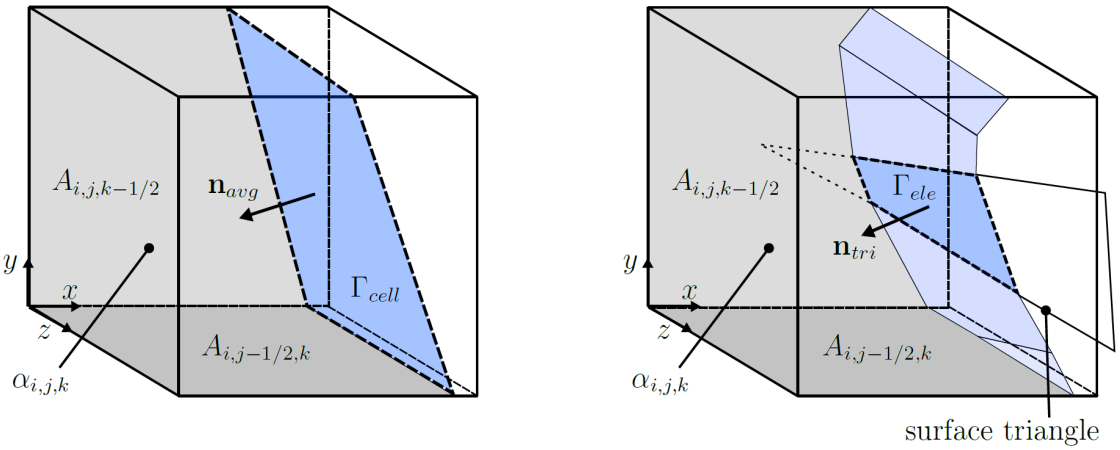

(a) **(b)**

Figure 3.2: Sketches of (a) level-set and (b) cut-element techniques. Retrieved from Örley [95].

grid is given by

$$\begin{aligned}\alpha^{n+1}_{i,j,k}\overline{\mathbf{U}}^{n+1}_{i,j,k} = \alpha^{n}_{i,j,k}\overline{\mathbf{U}}^{n}_{i,j,k} \\ + \frac{\Delta t}{\Delta x_i}\left[A_{i-1/2,j,k}\overline{\mathbf{F}}_{i-1/2,j,k} - A_{i+1/2,j,k}\overline{\mathbf{F}}_{i+1/2,j,k}\right] \\ + \frac{\Delta t}{\Delta y_j}\left[A_{i,j-1/2,k}\overline{\mathbf{F}}_{i,j-1/2,k} - A_{i,j+1/2,k}\overline{\mathbf{F}}_{i,j+1/2,k}\right] \\ + \frac{\Delta t}{\Delta z_k}\left[A_{i,j,k-1/2}\overline{\mathbf{F}}_{i,j,k-1/2} - A_{i,j,k+1/2}\overline{\mathbf{F}}_{i,j,k+1/2}\right] \\ + \frac{\Delta t}{V_{i,j,k}}\mathbf{X}_{i,j,k}\,.\end{aligned} \tag{3.6}$$

Note that, $\overline{\mathbf{F}}$ refers to the face-averaged fluxes at the cell faces. Here, the discretization in time is applied for a forward Euler scheme, which is a sub-step of the main Runge-Kutta scheme mentioned in Section 3.2. The variable $\mathbf{X}_{i,j,k}$ stands for the interface exchange term, which conveys the boundary information to the fluid cell, as will be discussed below. The immersed interface method in INCA has been further developed by Örley et al. [96] and Pasquariello et al. [105]. Those modifications are briefly discussed first.

The cut-cell method is shown in Fig. (3.2a) for a three-dimensional block with a so called level-set interface, which represents an average planar geometry as an approximation of the actual shape. Örley et al. [96] have noted that this method may result in numerical artifacts and spurious pressure oscillations for sharp interfaces or discontinuities in the deformation of the interface. They have proceeded to suggest an improvement, which accurately resolves the actual shape of the surface, by partitioning a cell interface into a set of cut-elements as shown in Fig. (3.2b). This is achieved by introducing sub-cell cut-elements that exactly preserve the triangulations based on the stereolithography or standard tessellation language (STL) definition of the solid surface. Cut-elements are directly obtained from the intersection of the STL description of a solid body and the fluid. Throughout the evolution of the surface, number of cut-elements and their connectivities vary, which leads to non-matching interfaces between the fluid and structural solvers. To remedy this concern, Pasquariello et al. [105] have extended the cut-element method to arbitrary interface deformations by combining the technique with a Mortar element method. This cut-element method is adopted in the present study.

Following this cut-element approach, the interface exchange term $\mathbf{X}_{i,j,k}$ in Eq. (3.6) can be expressed as a sum of the contributions of each cut-element as

$$\mathbf{X}_{i,j,k} = \sum_{el} \mathbf{X}_{el}\,, \tag{3.7}$$

where the index el goes over all cut-elements for a given cut-cell. For a given cut-element, interface exchange for momentum and energy can be expressed as

$$\mathbf{X}_{el} = \mathbf{X}_{el}^{p} + \mathbf{X}_{el}^{v} + \mathbf{X}_{el}^{q} \,, \tag{3.8}$$

where, from left to right the terms refer to pressure work, viscous stresses, and heat transfer. The pressure term is given by

$$\mathbf{X}_{el}^{p} = \begin{bmatrix} 0 \\ p_{\Gamma,el} \Delta\Gamma_{el} n_{\mathrm{x}}^{\Gamma,el} \\ p_{\Gamma,el} \Delta\Gamma_{el} n_{\mathrm{y}}^{\Gamma,el} \\ p_{\Gamma,el} \Delta\Gamma_{el} n_{\mathrm{z}}^{\Gamma,el} \\ p_{\Gamma,el} \Delta\Gamma_{el} \left(\mathbf{v}^{\Gamma,el} \cdot \mathbf{n}^{\Gamma,el} \right) \end{bmatrix} , \tag{3.9}$$

where $p_{\Gamma,el}$ is the element interface pressure obtained from a one-sided face-normal approximate Riemann solver, $\Delta\Gamma_{el}$ is the interface area per element, $n^{\Gamma,el}$ refers to the normal vector of the element, and $\mathbf{v}^{\Gamma,el}$ is the interface velocity evaluated at the face centroid. Similarly, the viscous term is given by

$$\mathbf{X}_{el}^{v} = \begin{bmatrix} 0 \\ \left(\int_{\Gamma_{el}} \overline{\overline{\boldsymbol{\tau}}} \cdot \mathbf{n}^{\Gamma,el} dS \right)_{\mathrm{x}} \\ \left(\int_{\Gamma_{el}} \overline{\overline{\boldsymbol{\tau}}} \cdot \mathbf{n}^{\Gamma,el} dS \right)_{\mathrm{y}} \\ \left(\int_{\Gamma_{el}} \overline{\overline{\boldsymbol{\tau}}} \cdot \mathbf{n}^{\Gamma,el} dS \right)_{\mathrm{z}} \\ \int_{\Gamma_{el}} \left(\overline{\overline{\boldsymbol{\tau}}} \cdot \mathbf{v}^{\Gamma,el} \right) \cdot \mathbf{n}^{\Gamma,el} dS \end{bmatrix} , \tag{3.10}$$

where $\overline{\overline{\boldsymbol{\tau}}}$ is the local stress tensor. Lastly, the heat exchange for an isothermal wall is given by

$$\mathbf{X}_{el}^{q} = \begin{bmatrix} 0 \\ 0 \\ 0 \\ 0 \\ \int_{\Gamma_{el}} (-\lambda \boldsymbol{\nabla} T) \cdot \mathbf{n}^{\Gamma,el} dS \end{bmatrix} . \tag{3.11}$$

Note that in all of these terms, the local values for cut-elements are selected to be the ones at a so called image point, which is generally half cell size away from the interface. The value of a quantity of interest at the image point is acquired by interpolating it from the surrounding cell centers.

As it can be deduced from the exchange terms, only the momentum and energy contributions are present in these formulations, i.e. the first row of each exchange term is zero. This is because there is no mass exchange in the basic isothermal and adiabatic boundary conditions in standalone INCA. This no longer remains true for an interface undergoing gas-surface interactions, as it will be presented in Section 3.4.2.

3.3.2. Ghost-cell Boundary Conditions

Once the exchange terms of the finite volume is conservatively defined with the help of the immersed interface method, ghost-cells are employed to communicate the boundary information to the actual solution. Ghost-cells are located at the interior of the solid domain but lie close to the solid wall interface. These cells are used to complete the finite volume reconstruction close to the wall without requiring any modification of the computational stencil. Ghost-cell values are extrapolated according to the desired boundary conditions as proposed by Mittal et al. [89] and further extended to stationary and moving interfaces by Pasquariello et al. [105]. For this purpose, an average face centroid and normal vector calculated from a weighted average of all cut-elements associated with that cell is favored over the intricate cut-element geometry. As it can be seen in Fig. (3.3), cell-center of a ghost-cell is selected as the ghost-point. An image point is defined $2\Delta l$ away from the ghost-point, where Δl is equal to the distance between the ghost-point and the boundary-intercept. The value at this image-point is estimated from the surrounding eight (four in two dimensions) cells by triliner (bilinear in

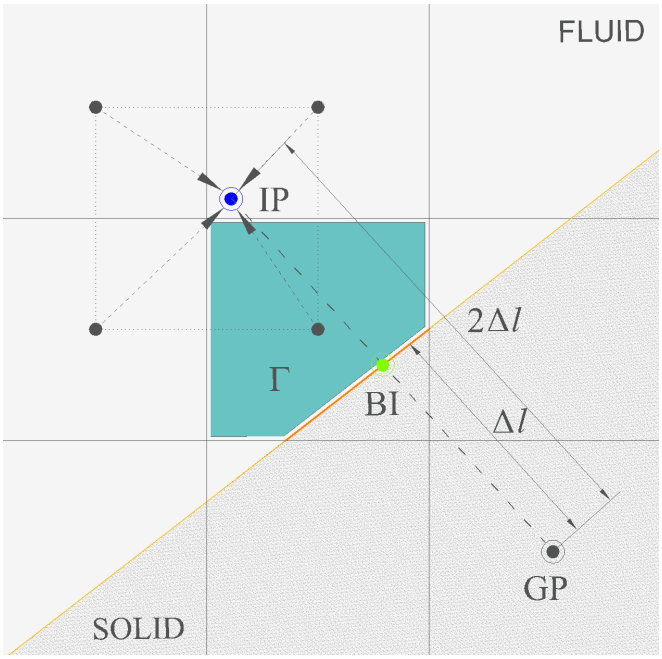

Figure 3.3: Sketch of a two-dimensional ghost-cell extrapolation.

two dimensions) interpolation. Since the boundary-intercept is prescribed beforehand according to the boundary condition, once the image-point value is known, a linear extrapolation is used to find the value of a flow quantity at the ghost-point. After primitive variables are extrapolated to ghost-points, thermodynamic routines are called to compute the state of the mixture under the given conditions. Including gas-surface interactions essentially modifies the wall boundary condition and consequently the ghost-point extrapolation, which will be discussed in Section 3.4.2.

A common issue for ghost-point extrapolation in high-temperature flows with cold walls ($T_{BI} \ll T_{IP}$) is that the extrapolation might lead to unphysical values at the ghost-points if the mesh is too coarse such that the thermal boundary layer is not resolved. This becomes apparent when the image point temperature is of the order of thousands and the wall temperature is close to standard temperature. Then, a linear extrapolation to the ghost point might result in a negative temperature value. A fix for this problem, when reducing the cell size is too costly, is to use a simple clamping check, which ensures a non-negative minimum value for the ghost-point temperature. This limit is selected as the half of the wall temperature value. Among other strategies tested in another immersed boundary ghost-cell approach [121], this one was seen to work most effectively. This clamping was also applied in the current simulations and it was modified for the vibrational temperature.

3.4. Coupling Implementations

This section concerns itself with the computational procedure undertaken during the coupling of the INCA solver with the Mutation^{++} library. The main purpose of this section is to act as a quick manual to aid in the accessibility of this distribution by potential future users. For prospective developers, more detailed information regarding all the modifications during the coupling procedure is given in Appendix A.

Since INCA did not host a dedicated application programming interface (API), all changes were directly applied to the source code. This meant that hard-coded baseline models needed to be bypassed by providing additional options for the new implementations. Full coupling is achieved in the final distribution with all available modules, as none of the standalone INCA subroutines for thermodynamics, transport or chemical rates are being used, when Mutation^{++} is enabled. Calls to Mutation^{++} features from INCA first pass through the interface module, which stores all the relevant subroutines. This interface is written to establish the necessary communication of variables between the two libraries. The subroutines inside this interface had to be blended in a compatible way with INCA's existing framework. Although this entails tedious bookkeeping, it allowed for a more efficient implementation,

which showed a noticeable advantage in terms of computational overhead compared to implementations of Mutation^{++} through an API for other flow solvers. Throughout the entire coupling, the current development refrained from code alterations inside Mutation^{++} to preserve ease of library updates.

Compilation of Mutation^{++} is linked to the main INCA compilation. Once the environment variables necessary for Mutation^{++} to function are provided, the distribution becomes operational. These environment variables are mentioned in the guidelines of Mutation^{++} and are also provided within the first few lines of the interface code. Once these are set, Mutation^{++} implementation can be enabled with just three options from the main INCA input file: `MUTATIONPP_LIB` takes on a logical argument to turn the implementation on or off, `MPP_MIXNAME` sets the Mutation^{++} mixture file name, and `MPP_STATE_MODEL` selects the thermochemical flow model as equilibrium (`Equil`), chemical nonequilibrium (`ChemNonEq1T`), or thermochemical nonequilibrium (`ChemNonEqTTv`). Guidelines for setting up these appropriate mixture and mechanism files can be found in the documentation for Mutation^{++} [120]. These are written in the extensible markup language (XML) format. The inputs for species properties, thermodynamic database values and mechanism specifications required for the standalone INCA still need to be provided as dummy inputs, which are only read during the initial setup and disregarded afterwards. To enable gas-surface interactions, the user needs to provide an appropriate GSI mechanism file for Mutation^{++} and select the desired immersed boundary wall option for the surface mass balance (`MASS`), or mass and energy balances (`ENER`). Although not considered in this work, when interface recession speeds will be enabled, the density of the solid in Eq. (2.84) can be defined right after the wall option in the immersed boundary input file.

3.4.1. T-T$^{\mathrm{V}}$ Two-Temperature Model

The thermal nonequilibrium model within Mutation^{++} was discussed in Section 2.5. The implementation of this model required the introduction of a vibrational energy variable to be conserved, an associated vibrational temperature and a vibrational thermal conductivity. In accordance with the theory, the general transport equation for the vibrational energy required the addition of the vibrational heat flux and the source terms in Eq. (2.70). The conductive and diffusive terms of the vibrational heat flux are added for the vibrational energy conservation and also for their contribution in the global energy conservation. The source term for vibrational energy exchange and chemical reactions are added in two half time steps of the Strang time-splitting scheme. The ODE-solver for the separate source term problem is also modified to include the vibrational temperature as an input.

At the immersed boundary, thermal equilibrium assumption is imposed, as warranted by the discussion in Section 2.6.1. Due to its commonality in the surveyed literature, the strict form of this assumption with $T = T^{\mathrm{V}}$ is selected rather than imposing zero change in vibrational temperature at the wall. In instances where the translational temperature is being clamped to a limit as explained in Section 3.3.2, the wall temperature seen by the vibrational temperature is adjusted accordingly.

3.4.2. Gas-Surface Interactions with an Immersed Boundary Method

As explained in Section 2.6, the GSI module in Mutation^{++} works as a boundary condition for the flow solver. As an input, this module accepts the chemical state at a certain distance away from the surface. To be consistent with the immersed boundary formulation, this point is referred to as an image point. Given the species mole fractions at the image point, and the distance of the surface to this point, mole fraction gradient for the Stefan-Maxwell diffusion model can be computed. Depending on the selected surface option, either the mass balance in Eq. (2.81) is solved with an isothermal wall temperature, or an energy balance in Eq. (2.85) is solved assuming steady-state conduction. The resultant surface state is defined by the new surface species concentrations and the surface temperature. Additionally, depending on the surface type, chemical production rates of each species is outputted. These contributions sum up to zero for a catalytic wall condition, and according to Eq. (2.83) give zero blowing velocity. For an ablative wall condition on the other hand, this summation yields the total mass blowing flux and consequently the blowing velocity. After Mutation^{++} provides this surface state, this information needs to be interpreted by INCA for the flow to register the presence of the reacting surface.

Similar to the non-reactive, or non-catalytic wall mentioned in Section 3.3.2, boundary conditions need to be extrapolated to the ghost-cells. Using the values at an image point in the fluid and the species concentrations, surface temperature, and blowing velocity at the wall, ghost-point properties are found through a linear extrapolation. Similarly to the extrapolated temperatures, extrapolated

species fractions are limited by physical constraints to avoid nonphysical values.

The ghost point extrapolation of GSI outputs is a common and sufficient procedure followed by most flow solvers, which utilize a similar coupling framework. However, in the case of INCA, to conservatively complete the finite volume definition of the cut-cells, the immersed interface method explained in Section 3.3.1 needs to be modified as well. This is apparent from the fact that now a reacting interface is present for the cut-cells. More specifically, each cut-element comprising the cut-cell interface needs to take into account the impact of GSI on momentum and energy exchange at the interface and it must now include the exchange of mass as well. This is established by proposing two additional exchange terms for mass by rewriting Eq. (3.8) for a reacting interface as

$$\mathbf{X}_{el} = \mathbf{X}_{el}^{p} + \mathbf{X}_{el}^{v} + \mathbf{X}_{el}^{q} + \mathbf{X}_{el}^{m} + \mathbf{X}_{el}^{sp} \,, \tag{3.12}$$

where $\mathbf{X}_{el}^{m}$ stands for the global mass exchange and $\mathbf{X}_{el}^{sp}$ stands for the species mass exchange for each species i for a given cut-element.

The new exchange term for global mass exchange can be mathematically expressed as

$$\mathbf{X}_{el}^{m} = \begin{bmatrix} \int_{\Gamma_{el}} \dot{m}\, dS \\ \left[\int_{\Gamma_{el}} \dot{m} \left(\mathbf{v}_{blow}^{\Gamma,el} \cdot \mathbf{n}^{\Gamma,el}\right) dS\right]_{\mathrm{x}} \\ \left[\int_{\Gamma_{el}} \dot{m} \left(\mathbf{v}_{blow}^{\Gamma,el} \cdot \mathbf{n}^{\Gamma,el}\right) dS\right]_{\mathrm{y}} \\ \left[\int_{\Gamma_{el}} \dot{m} \left(\mathbf{v}_{blow}^{\Gamma,el} \cdot \mathbf{n}^{\Gamma,el}\right) dS\right]_{\mathrm{z}} \\ \left[\int_{\Gamma_{el}} \dot{m} \left(e^{\Gamma,el} + \frac{1}{2}\| \mathbf{v}_{blow}^{\Gamma,el} \|^2\right) dS\right] \end{bmatrix} , \tag{3.13}$$

where $\dot{m}$ is the total species production rate given in Eq. (2.82), $\mathbf{v}_{blow}^{\Gamma,el}$ is the blowing velocity given by Eq. (2.83), and $e^{\Gamma,el}$ is the internal energy at the interface. Note that since a momentum balance is not solved in the GSI module, the blowing is always taken normal to the surface. Hence, the dot product with the blowing velocity essentially extracts the component of the inviscid normal momentum flux in the relevant coordinate axis.

Similarly, the mass exchange for each species i can be written as

$$\mathbf{X}_{el}^{sp} = \left[\int_{\Gamma_{el}} \dot{m}_i\, dS\right] \,, \tag{3.14}$$

which does not adhere to the vector arrangement of other exchange terms as it expands according to the number of species. Naturally, the sum of the species mass exchange terms yields the global mass exchange and it is only non-zero when the surface is ablative. However, as long as the surface is reacting, catalytic reactions will alter the surface species compositions and therefore lead to non-zero species mass exchange. With the addition of these two terms, an interface definition for global and species mass exchange is established.

The presence of GSI also requires modifications to the existing interface terms for pressure work, viscous stresses and heat transfer. For pressure and viscous effects, the recession in an ablative simulation leads to positive interface velocities $\mathbf{v}^{\Gamma,el}$ normal to the cut-element, computed according to Eq. (2.84) for the terms in Eq. (3.9) and Eq. (3.10), similar to a moving geometry [96, 105]. Regarding the approximately solved Riemann problem for the interface pressure, the interface velocity translates to the velocity of the intermediate state. For the viscous term, the difference between the image point velocity and the interface velocity is used to compute the velocity gradient in the local stress tensor. Lastly, for the heat exchange term, since with GSI there is diffusion of species at the interface, the enthalpy of diffusion should be included in Eq. (3.11) as

$$\mathbf{X}_{el}^{q} = \begin{bmatrix} 0 \\ 0 \\ 0 \\ 0 \\ \int_{\Gamma_{el}} \left(-\lambda \boldsymbol{\nabla} T + \sum_i h_i \rho_i \boldsymbol{\mathcal{V}}_i\right) \cdot \mathbf{n}^{\Gamma,el} dS \end{bmatrix} . \tag{3.15}$$

This additional term for the diffusive heat flux plays a major role in estimating the total surface heat flux and it also required a new post-processing routine to account for its contribution.

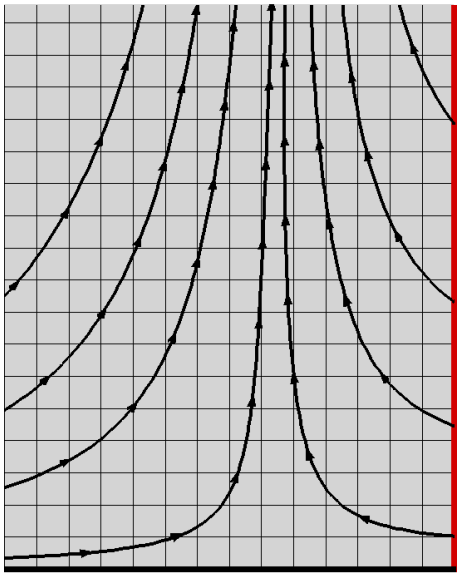

Figure 3.4: Streamlines for an example case of surface blowing with the GSI implementation, produced by INCA-Mutation^{++} coupling. Flow approaches from the left-hand side and the red edge indicates an ablative wall.

These new exchange terms for each cut-element fully define the surface interface with GSI and complete the construction of the finite volume scheme for the cut-cells. These exchange terms are added to the fluxes coming from the fluid faces, including the deformed faces which are scaled with the face apertures. Then, the fluid solution can be advanced and the ghost-point values can be determined using these updated cut-cells for the image point interpolation. An inherent drawback of this procedure is that the GSI module needs to be called for two different occasions for a given cell: once for each cut-element associated with a cut-cell, and a second time during the extrapolation to ghost-points. This is expected to increase the computational cost, yet it is currently the only plausible way to adopt this approach consistently. In the future, storing the GSI solution in the cut-element data structure should be considered. A sample visual to demonstrate surface blowing in INCA with these new implementations is presented in Fig. (3.4).

To the author's knowledge, this thesis marks the first time that a boundary condition for gas-surface interactions has been implemented in a conservative immersed boundary method.

4

Validation Results and Discussion

A fundamental step in this study involves the application of the coupled framework presented in the preceding chapters. In order to establish a sufficient level of confidence in these new implementations, evaluating the accuracy and performance of this framework in relevant problems is an indispensable task. This chapter presents the results of the simulations conducted for this purpose.

The verification and validation of these implementations will be performed through comparison with test cases of interest. As discussed in Section 3.2, since a large number of trials were foreseen to successfully operate this new framework, one of the main concerns for the test cases was efficiency. To that end, test cases with two-dimensional cylindrical geometries are selected as a roughly approximated representation of blunt capsule heat shields. Quarter cylinders are employed to make use of symmetry, and since the front region is of more interest than the rear. General structure of a coarse and fine grid are given in Fig. (4.1). This type of grid was generated for all the considered cases by the use of INCA's adaptive mesh refinement module. The grids were generated based on the given minimum size for the cell being cut by the fluid-solid interface. Depending on the surface resolution requirements, the minimum cell size for the cut-cell varied between the different cases considered. Once this smallest cell size is defined, a grid block is then refined around that cut-cell. Then, the grid progressively gets coarser towards the edges of the domain, becoming twice as large with each coarsening step. Each refinement step forms a block of uniformly-sized cells in line with the partitioning procedure for parallel computing. Block sizes vary in order to keep the number of cells at each block similar, i.e. spatially larger blocks contain coarser grids and vice versa. This helps to provide an efficient partitioning; distributing comparable amounts of computational load for each processor. As the grid gradually becomes coarser according to the selected minimum cell size, the residual cell resolution in the vicinity of the shock was mostly sufficient to accurately represent the discontinuity. Hence, no separate shock refinement was applied. Additionally, the interior grids which lie deep beneath the solid and do not contribute to the flow solution are automatically removed to avoid additional library calls for those cells. These choices aided in further lowering the computational cost per simulation.

A standard supersonic inlet condition is imposed on the left edge of the domain by fully defining the thermochemical state and velocity according to the corresponding freestream values. A first order Neumann condition imposing zero gradients through the boundary is selected for the top and right edges. The bottom edge holds the symmetry boundary condition with zero gradients and zero normal velocity. The wall boundary condition along the cylindrical surface is given by the conservative immersed interface method presented in Section 3.3.1. Depending on the flow physics, an adiabatic, isothermal or reacting immersed boundary is selected.

In terms of the numerical scheme, the third-order WENO scheme mentioned in Section 3.2 is used instead of the fifth-order alternative. It was seen that the third-order scheme was already able to match the sought accuracy level in the test cases that were considered. In earlier trials with the fifth-order scheme, it was observed that a sharper shock profile was captured, yet the influence on the heat fluxes were insignificant. Additionally, it was seen that the fifth-order scheme was more prone to amplifying numerical distortions. These observations did not justify the additional cost of the larger computational stencil evaluation.

According to the above specifications, three separate campaigns were studied; from Sekhar [121] in

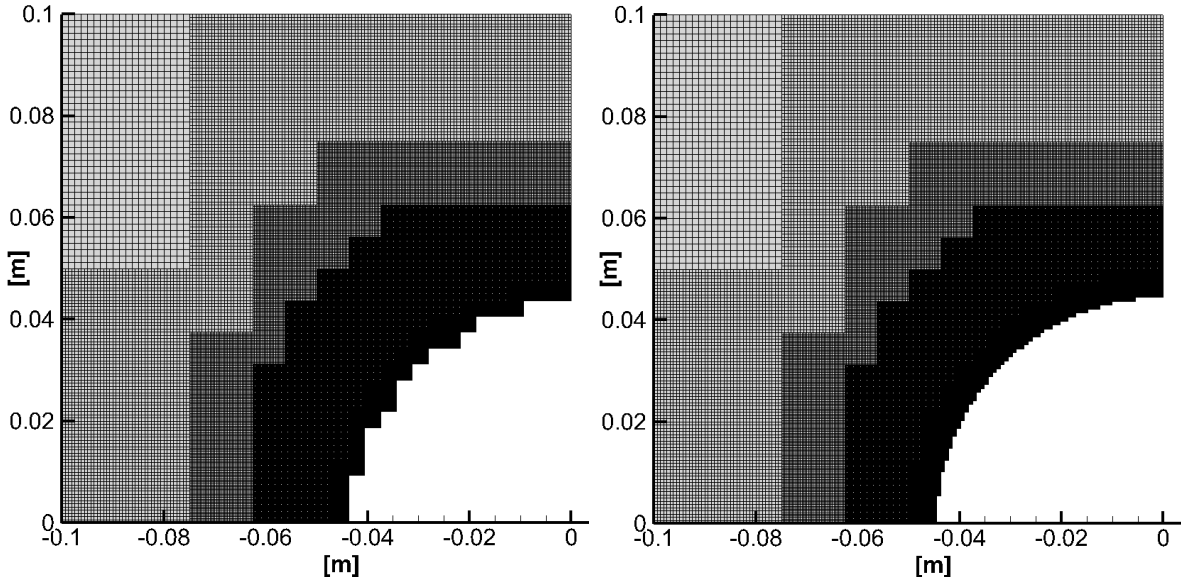

Figure 4.1: General structure of (a) coarser and (b) finer grids having first cell distances of 1×10^{-4} and 1×10^{-5} next to the surface, respectively.

Section 4.1, Knight et al. [63] in Section 4.2, and Chen & Milos [25] in Section 4.3. Details of each are given in their respective sections. A table summarizing the array of test cases considered under each campaign is given in Table 4.1. The relevant mixtures and reaction mechanisms are provided in Appendix B. Effects of radiation, ionization, and recession are neglected in all of these campaigns. The general approach in the selection of these test cases aimed at analyzing the fundamental features studied in this context. Inviscid and viscous cases, low to moderately high hypersonic Mach numbers, pressures, and freestream temperatures, cold and hot wall temperatures are all studied to explore the capabilities and limitations of this analysis tool in a wide range of challenging environments relevant for atmospheric entry applications. The selected cases investigated the effects of chemical nonequilibrium, thermochemical nonequilibrium, and gas-surface interactions, which are classified under the tags "CNE", "TTV", and "GSI", respectively. Comparisons were made with the standalone INCA, whenever possible. Results for the standalone INCA are trivially labeled as "INCA", and the ones utilizing the Mutation^{++} coupling are labeled "INCA-M^{++}". These shorthand notations are followed throughout the chapter.

4.1. Flow Field under Thermochemical Nonequilibrium

The first campaign to be considered reproduces the chemically reacting inviscid and viscous cases from Sekhar [121], which are the final cases presented in his thesis incorporating all the development for their code. One of the reasons for selecting this test case was this code, NASCART-GT, which similarly employs the Cartesian grid immersed-boundary finite-volume approach. Contrary to the current immersed interface method with cut-cells and cut-elements in INCA, NASCART-GT depends solely on ghost cells for imposing the boundary conditions. As noted in Section 3.3, this approach is more straightforward and generally computationally less demanding, but practically it does not ensure conservation in the flow. The comparison here with INCA will outline how these aspects influence the accuracy of both codes. The reference simulations for this comparison are the ones given in Sekhar, performed by the DPLR solver, which was briefly described in Section 1.3. Being able to compare with such a well-established code was also an important motivation for this campaign. In general, the purpose of this test case is to demonstrate the capabilities of the INCA-Mutation^{++} framework under thermochemical nonequilibrium for these typical atmospheric entry conditions of low freestream densities, pressures and temperatures at a relatively high Mach number. The exact quantities could be found in Table 4.1.

The test cases considered by Sekhar aimed at predicting the main features of this Mach 12.7 flow with a relatively coarse grid structure. Since their goal was not to have an accurate estimation of

Table 4.1: Array of test cases considered in this study.

Test Cases	Flow Model	R_{cyl} [m]	M_∞	u_∞ [m/s]	ρ_∞ [kg/m^3]	P [Pa]	$y_{i,\infty}$	T_∞ [K]	T_{wall} [K]	Comparison with
Sekhar (Adia.)	TTV	0.1	12.7	3570	$1.6\text{x}10^{-3}$	90	N_2: 0.7671 O_2: 0.2329	195.96	-	NASCART-GT & DPLR
Sekhar (Isot.)									500	
Knight HEG I (Euler)	CNE	0.045	8.98	5956	$1.547\text{x}10^{-3}$	476	N_2: 0.7453 O_2: 0.00713 NO: 0.01026 N: $6.5\text{x}10^{-7}$ O: 0.2283	901	-	US3D
Knight HEG I (N-S)	CNE & TTV & GSI								300	5 Codes & Experiment & US3D
Knight HEG III (N-S)	CNE & TTV & GSI		8.78	4776	$3.26\text{x}10^{-3}$	687	N_2: 0.7356 O_2: 1340 NO: 0.0509 N: 0.0000 O: 0.07955	694	300	5 Codes & Experiment
Chen & Milos	GSI	0.01905	5.84	5354	$3\text{x}10^{-3}$	1671.36	N_2: 0.6169 O_2: 0.0000 NO: 0.0046 N: 0.1212 O: 0.2573	1428	3250	2 Codes & Experiment

the surface heat fluxes, the minimum cell size at the wall was taken on the order of 10^{-4} m. The resulting number of cells were 96 000 for the inviscid case and 18 000 for the viscous case. However, due to poor agreement for the viscous case, the results were later updated by Sekhar and Ruffin [122] with a grid having 924 000 cells. These updated results are used for comparison in this campaign. The grids generated by the current study in INCA respected this coarse resolution to be comparable. Due to nonphysical extrapolations observed at grid refinement steps with thermal nonequilibrium, uniform grids were used instead. In order to maintain similar number of cells, the smallest cell size was taken as 7×10^{-4} m, which resulted in a total of 94 080 cells.

NASCART-GT utilizes a combination of the AUSMPW+ scheme and the MUSCL scheme for the discretization of the convective fluxes with second-order accuracy. Viscous terms are discretized by second-order central differencing. The implicit LU-SSOR scheme is used for temporal discretization. Transport properties are obtained from simplified mixture rules. Chemistry source terms are similarly decoupled and solved with a point-implicit solver. The code can operate with thermochemical nonequilibrium using Park's two-temperature model [100] just as Mutation^{++}, but does not include any implementations to handle gas-surface interactions. Hence, simplified adiabatic and isothermal wall boundary conditions are employed for the inviscid and viscous cases, respectively. Thermal equilibrium is enforced at the wall.

The results of INCA with the Mutation^{++} implementations are presented in the following sections for the inviscid and viscous cases. The reaction mechanisms are taken from Park [101] as given in Appendix B, to be consistent with NASCART-GT. The standalone INCA solver could not be operated under these conditions due to a failure in chemical source term computations. It is suspected that estimating the Jacobians of the chemical source terms, Eq. (2.69), with finite-differences was not suitable under these conditions, where the reaction rates are very fast. Mutation^{++} implementation overcomes this issue by providing analytical expressions. Additionally, the INCA results would have been limited only to a single temperature definition. As it will be seen, thermal nonequilibrium was prominent in these results due to the strong shock wave, and it could only be included within the INCA-M^{++} framework developed in this study.

4.1.1. Inviscid Simulations

The inviscid simulations with the adiabatic wall boundary condition are presented in Fig. (4.2) for the Mach number and pressure contours, and in Fig. (4.3) for the translational and vibrational temperature contours. A major and most immediate conclusion to be drawn from these figures is the successful operation of INCA with Mutation^{++}. The strong bow shock is captured sufficiently. The subsonic region close to the nose and the sonic line where the flow transitions to supersonic speeds are identified as clearly as the reference results. Compared to the freestream pressure, the flow compresses by 200 times at the stagnation point, and then expands towards the shoulder. Temperature contours display the large temperature jump as the high kinetic energy of the incoming hypersonic flow is released beyond the shock as the flow halts to subsonic speeds. Thermal nonequilibrium occurs as it can be observed that the behavior of the translational-rotational and vibrational-electronic temperatures are considerably different from each other. Vibrational temperature lags behind the translational temperature as the governing energy transfer mechanisms are slower.

It can be seen that the shock standoff distance is around 0.029 m for all three codes. However, the shock is much finely resolved for NASCART-GT, when compared to INCA-M^{++} and DPLR. Allocating a large number of cells around a possibly over-refined shock has resulted in poorer accuracy in other regions of the domain for NASCART-GT. For example, INCA-M^{++} agrees better with DPLR than NASCART-GT in the stagnation point region and the shoulder of the cylinder around 90° angle. As DPLR is the more referenced code, this agreement aids in confirming the off-surface capabilities of the present development. Certain fluctuations are present aft of the shock for pressure and temperature contours, which might be related to the relatively coarse grid structure. However, the overall extends of the contours are in line with DPLR, especially for the vibrational temperatures where a large discrepancy is present for NASCART-GT.

Properties along the stagnation line are also compared for temperatures in Fig. (4.4). The vibrational excitation is seen to be clearly predicted by INCA-M^{++}. As anticipated, ambient molecules vibrationally excite beyond the shock and the dissociating species in the shock layer transfer some amount of that energy to the thermal bath of translational energy. Since this process occurs at a finite and relatively slow rate, the vibrational temperature lags the translational temperature, achieving its peak more downstream. The vibrational temperature peak is not as large as that for the translational temperature due to this slow energy transfer between the modes and also due to the dissociation of molecular species past the shock. For the translational and vibrational temperatures INCA-M^{++} results again agree better with DPLR than NASCART-GT. Peak translational and vibrational temperatures are around 6000 K and 4900 K, respectively for both INCA-M^{++} and DPLR. The extended vibrational excitation region behind the shock in NASCART-GT is also visible from the contour plots. However, this higher vibrational temperature region is absent in the predictions of INCA-M^{++} and DPLR. It can also be seen that the peaks of the vibrational temperatures occur at the intersection of the vibrational and translational temperature curves. This is a theoretically expected behavior of the currently employed non-preferential dissociation model mentioned in Section 2.5. At the wall, all simulations equilibrate at the same temperature of 3725 K, which is a very high temperature as there is no boundary layer cooling for the inviscid case.

For the mole fractions along the stagnation line in Fig. (4.5), it can again be seen that the results are similar between all simulations. These temperatures are not high enough for a significant dissociation of N_2. On the other hand, dissociation of O_2 beyond the shock is apparent from the sharp increase of O fractions. It was seen that the concentrations of NO and N were on the order of 10^{-5} for INCA-M^{++}, which meant that they did not appear within the range of compared references. Consequently, a higher concentration of O_2 is predicted for the current simulations, whereas the references suggest further dissociation towards the body for the recombination reactions producing NO. As the selected mechanisms and governing relaxation models are theoretically consistent between the codes, this discrepancy might be attributed to the differences in the thermodynamic databases used. Mutation^{++} currently relies solely on the RRHO database when thermal nonequilibrium is considered. Instead, using a combination of the NASA polynomial database with RRHO database would be more beneficial. This is already a planned implementation in the Mutation^{++} community. It was not attempted in this study to avoid any modifications to the baseline Mutation^{++} distribution for the sake of maintaining accessibility. Nevertheless, the concentrations of major species agree well with both DPLR and NASCART-GT. Overall, good agreement is obtained for the inviscid results.

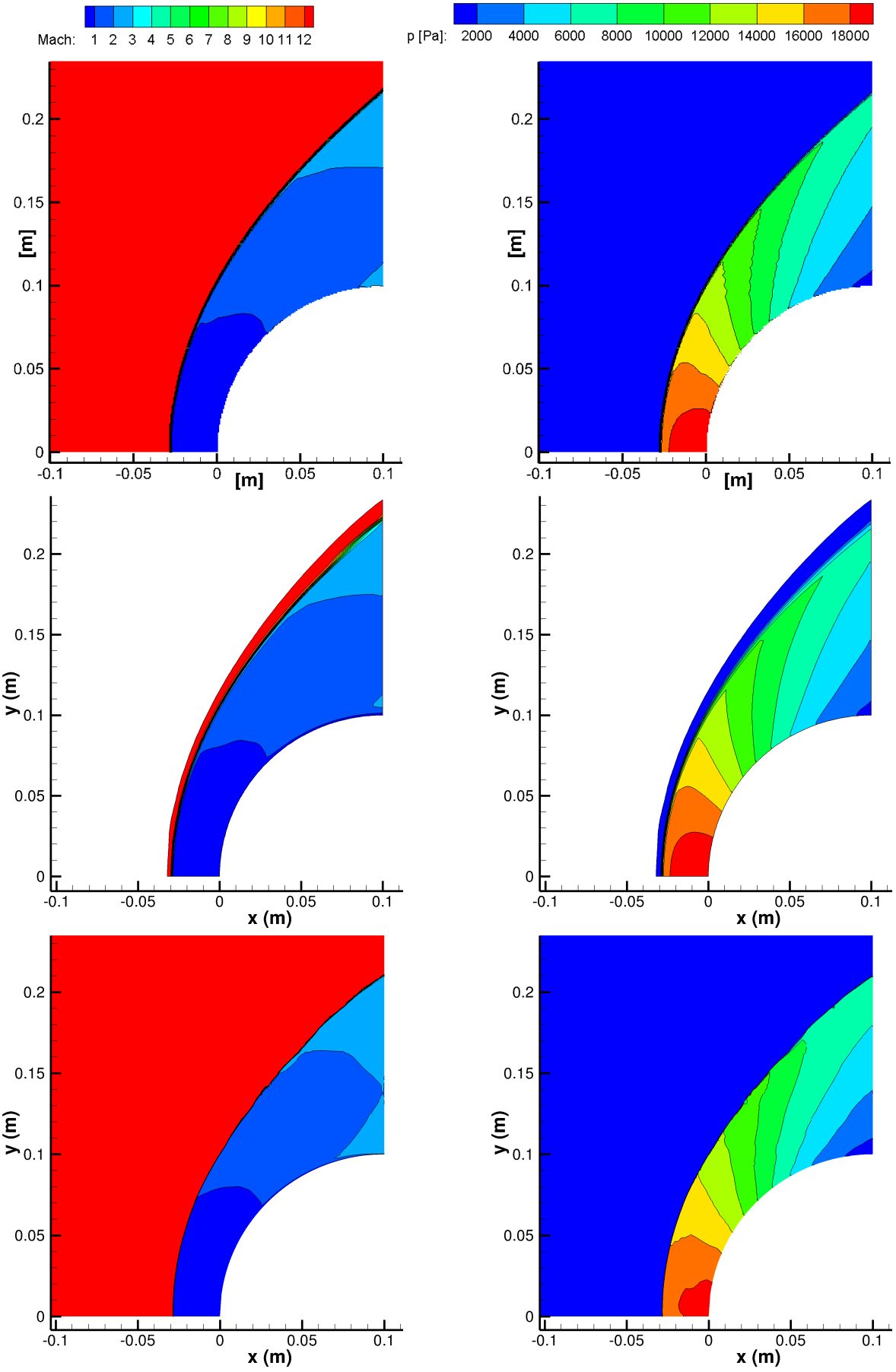

Figure 4.2: Comparison of Mach number (left column) and pressure (right column) contours for INCA-M^{++} (first row), DPLR (second row), and NASCART-GT (third row) for the inviscid case from Sekhar.

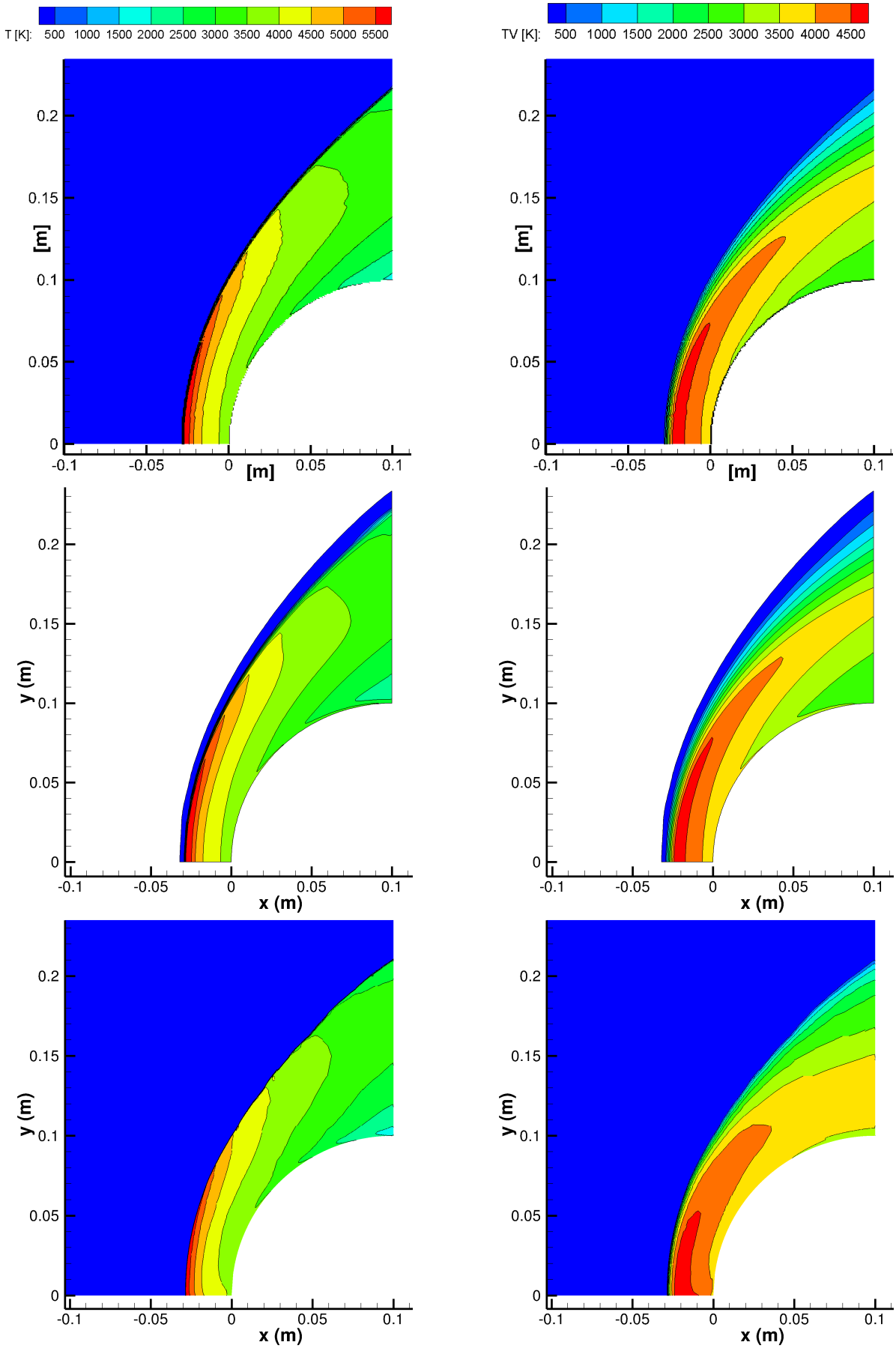

Figure 4.3: Comparison of translational temperature (left column) and vibrational temperature (right column) contours for INCA-M^{++} (first row), DPLR (second row), and NASCART-GT (third row) for the inviscid case from Sekhar.

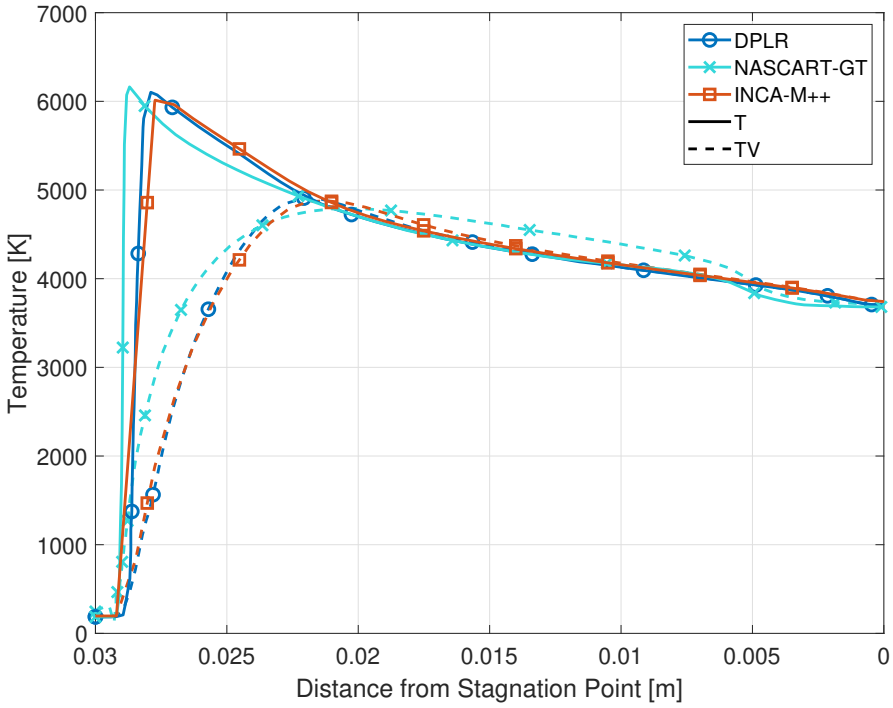

Figure 4.4: Comparison of temperatures along the stagnation line for INCA-M^{++}, DPLR, and NASCART-GT for the inviscid case from Sekhar.

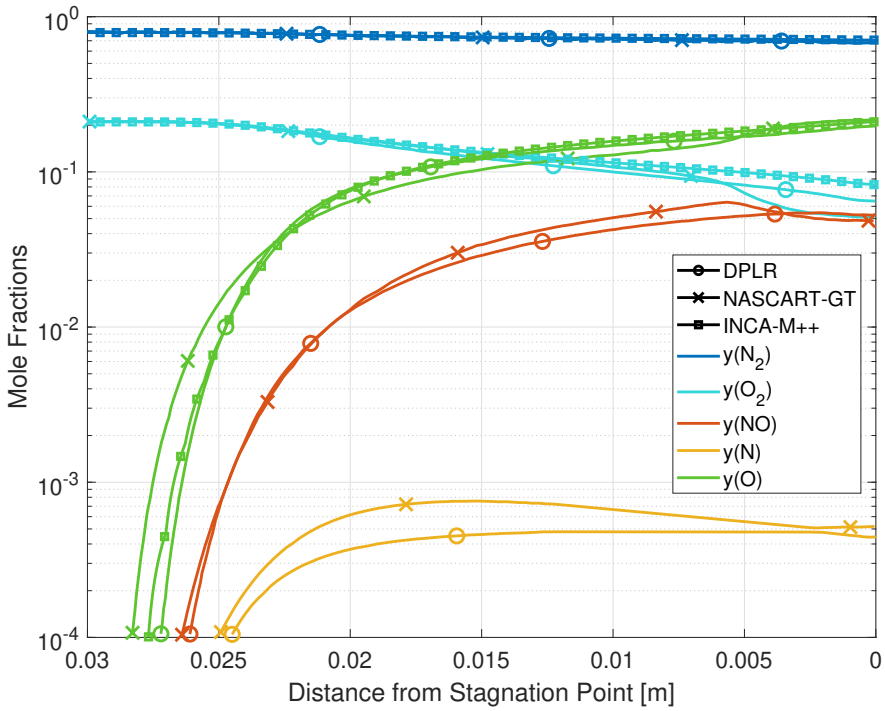

Figure 4.5: Comparison of mole fractions along the stagnation line for INCA-M^{++}, DPLR, and NASCART-GT for the inviscid case from Sekhar.

4.1.2. Viscous Simulations

The same conditions are now simulated with an isothermal wall at 500 K in a viscous flow field to consider the influence of transport properties. Note that these are the results presented by Sekhar and Ruffin [122] for a grid with 924 000 cells as an update to the previous results with a much coarser grid of 18 000 cells. However, since the pressure contours were not available in this paper, previous coarser result from Sekhar [121] is shown for that plot only. The grid for INCA-M^{++} remained the same as for the inviscid case with 94 080 cells. The contour plots can be found in Fig. (4.6) for Mach number and pressure, and in Fig. (4.7) for the translational and vibrational temperatures. A similarly good aggrement between INCA-M^{++} and DPLR is present, especially in the stagnation region and at the shoulder of the cylinder. Sonic line profile and the accelerated expansion region at the shoulder are smoothly captured. Extend of translational and vibrational temperature regions are also predicted well. As noted, since the purpose of these simulations was to investigate the general flow field as efficiently as possible, the grid is kept coarse. Both DPLR and NASCART-GT provides a finer resolution at the boundary layer, which is visible clearly in the temperature contours as the ambient temperature is being cooled down to the cold-wall temperature. Shock standoff distances of INCA-M^{++} and DPLR are again similar around 0.029 m, whereas NASCART-GT seems to be overpredicting it at around 0.033 m. Although operating with a much finer grid compared to the other codes, NASCART-GT is still unable to match the accuracy of DPLR in contrast to INCA-M^{++}, which again exhibits a very good agreement even with such a coarse grid.

Quantities along the stagnation line are not provided in the references for this case. Regardless, for the current isothermal simulations they are presented in Fig. (4.8) for temperatures and in Fig. (4.9) for mole fractions. Here, in addition to the solutions with the thermal nonequilibrium flow model, single temperature chemical nonequilibrium results with the Mutation^{++} implementation are also provided to assess the influence of vibrational excitation. As it can be clearly seen from the temperature plot, the shock standoff distance is considerably underestimated with the single temperature model. As opposed to a distance of 0.029 m supported by the previous comparison with references, the single temperature model predicts the shock to be 0.027 m away from the stagnation point. This stems from the lower post-shock density for the two-temperature model compared to the single temperature model. The chemical reaction rates are slower behind the shock for the two-temperature approach due to the geometric average temperature $\sqrt{T^{\mathrm{T}}T^{\mathrm{V}}}$ considered. Consequently, as dissociation reactions lag behind, the ratio of post-shock to freestream densities decreases, which in turn increases the standoff distance. Another intuitive way to interpret this is to note that density is mainly a function of the translational temperature, and a lower temperature corresponds to a denser shock layer with a shorter shock standoff distance. Additionally, since there is no vibrational energy transfer for the single temperature model, the peak shock temperatures are predicted lower at 5100 K, compared to the 6000 K of thermal nonequilibrium results. As anticipated, species mole fractions indicate a slight delay in dissociation reactions under thermal nonequilibrium. In general, an earlier dissociation for O_2 is followed by a weaker dissociation of N_2 due to marginally low temperatures. As the flow approaches the surface, both solutions begin to equilibrate. Close to the wall, vibrational temperature is slightly larger than the translational temperature with the recombination reactions giving rise to more molecular species. However, this boundary layer variation is not as apparent, since the grid is very coarse and does not host sufficient resolution close to the surface. In general this deviation is minor, and since the two temperatures reach the same equilibrium temperature, the initial remark in Section 2.6.1 regarding the negligible impact of thermal nonequilibrium at the wall is valid for this case.

This campaign has demonstrated the verification of the baseline Mutation^{++} implementations under chemical and thermal nonequilibrium conditions. Observations made here indicate the importance of considering thermal nonequilibrium, especially when there is no sufficient time for the flow to relax to equilibrium, such as for shock-boundary layer interaction problems. These test cases from Sekhar confirm that the extension of INCA to atmospheric entry regimes have been successful in accurately predicting the flow field around a blunt body.

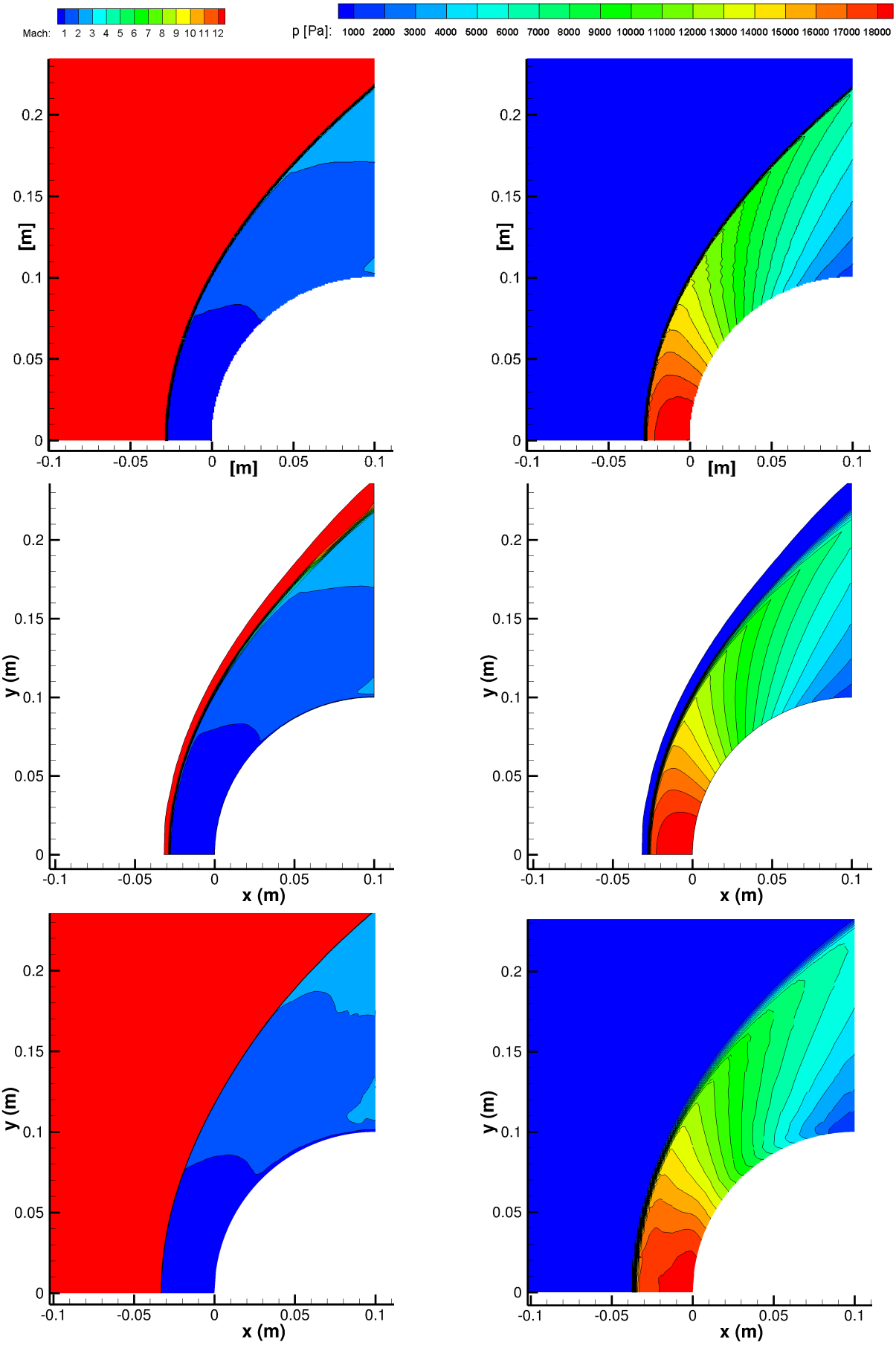

Figure 4.6: Comparison of Mach number (left column) and pressure (right column) contours for INCA-M^{++} (first row), DPLR (second row), and NASCART-GT (third row) for the viscous case from Sekhar and Ruffin. Pressure contour for NASCART-GT is from Sekhar.

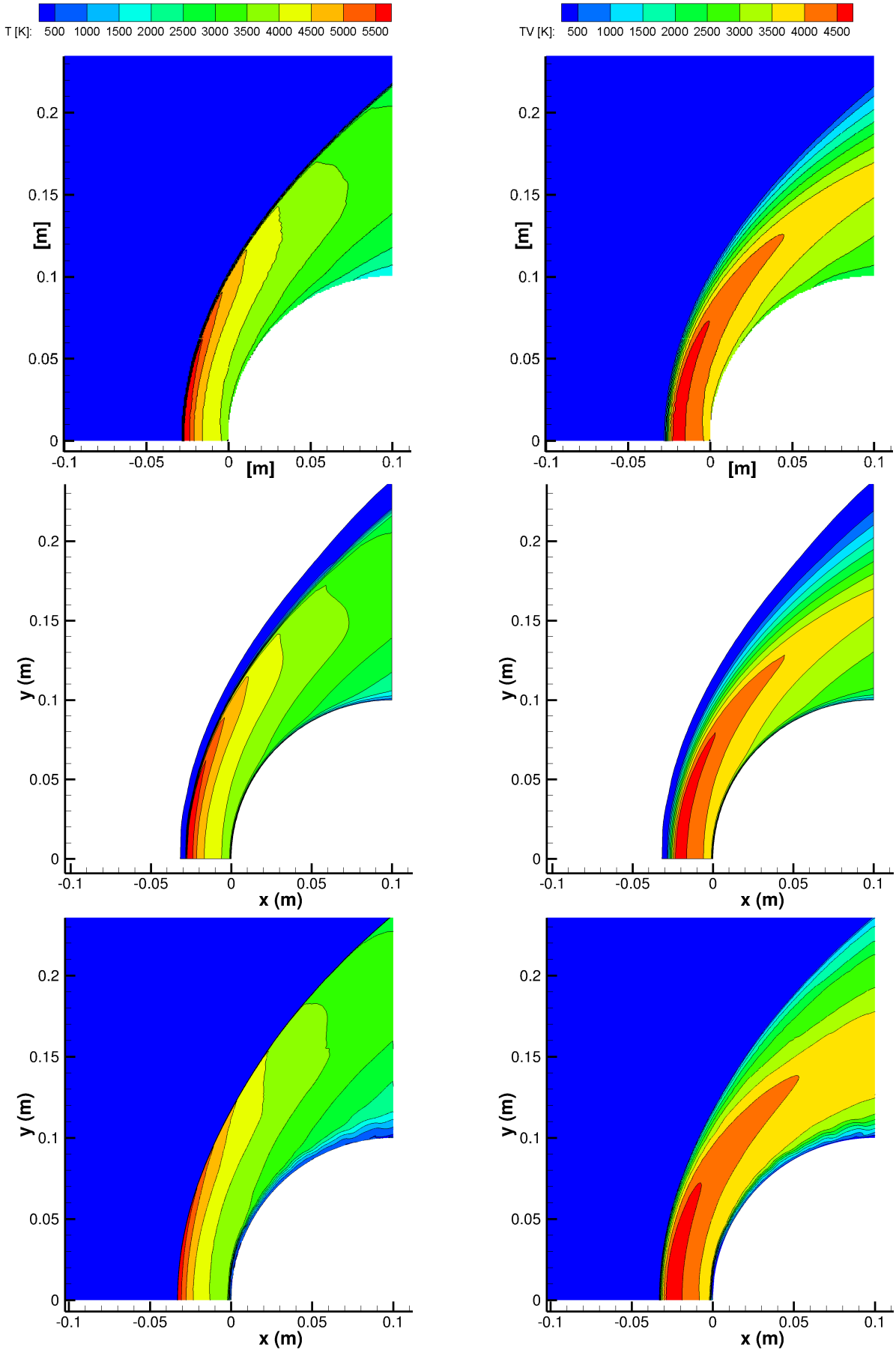

Figure 4.7: Comparison of translational temperature (left column) and vibrational temperature (right column) contours for INCA-M^{++} (first row), DPLR (second row), and NASCART-GT (third row) for the viscous case from Sekhar and Ruffin.

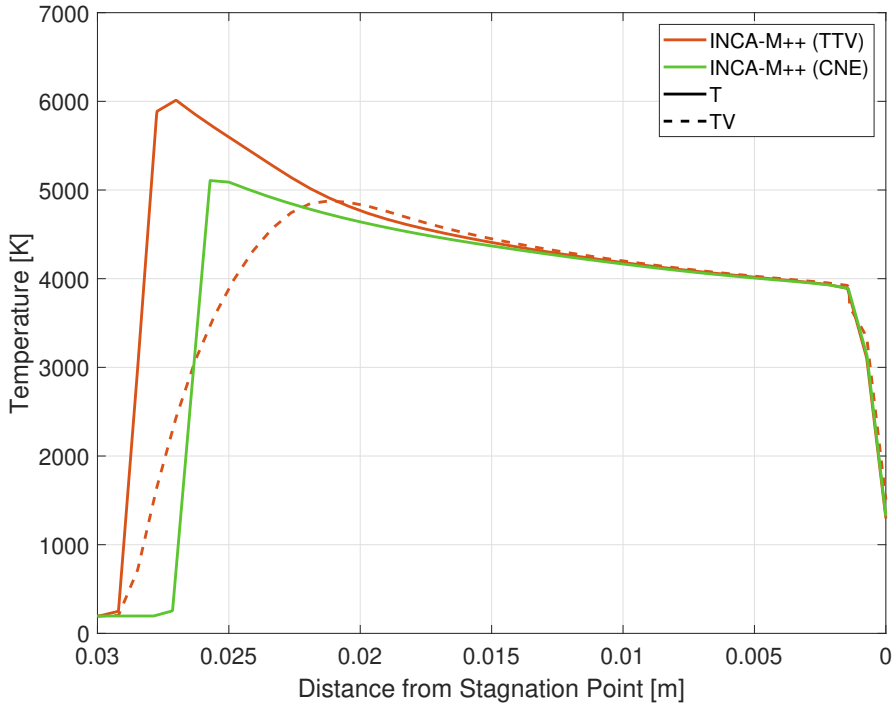

Figure 4.8: Comparison of temperatures along the stagnation line for INCA-M^{++} with TTV and CNE flow models for the viscous case from Sekhar.

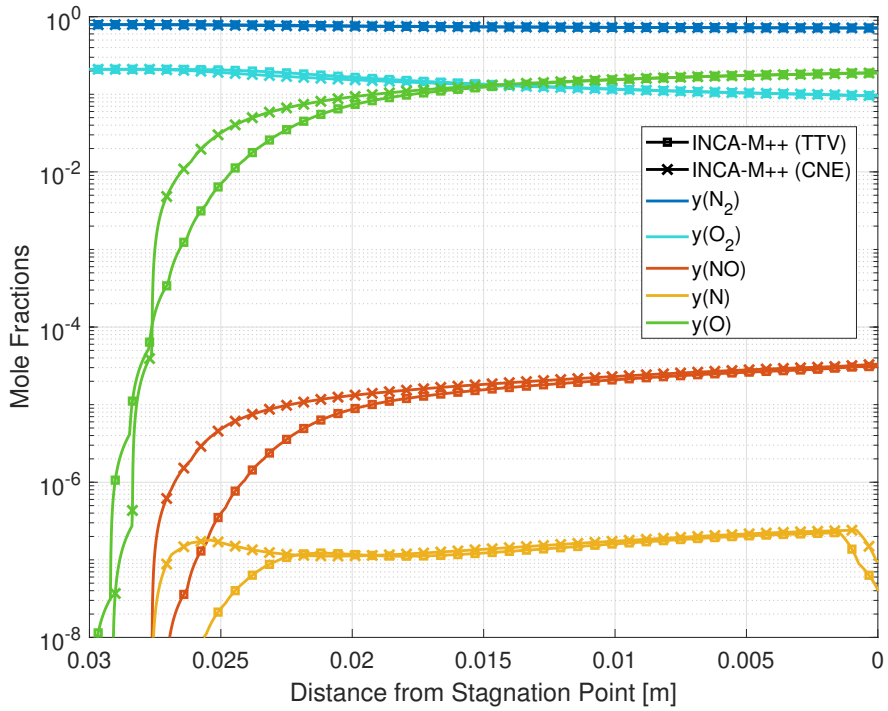

Figure 4.9: Comparison of mole fractions along the stagnation line for INCA-M^{++} with TTV and CNE flow models for the viscous case from Sekhar.

4.2. Influence of Catalysis on Surface Heat Fluxes

The second campaign considers the test cases presented by Knight et al. [63], where five different CFD codes from participating institutions are assessed with respect to the experiments conducted at the high-enthalpy shock tunnel of the German Aerospace Center (DLR). Two separate experiments are available, corresponding to 22.4 MJ/kg and 13.5 MJ/kg total enthalpy conditions, and are labeled as HEG I and HEG III, respectively. The freestream conditions can be found in Table 4.1. The reaction mechanisms employed in the INCA simulations for the 5-species air model are given in Appendix B.

The main idea behind the compilation of these different CFD code results by Knight et al., is to assess the capabilities of various computational tools by some of the experts in the aerothermodynamics community. All participants have independently used the best approaches available to them for their results. The study concludes that the prediction of heat fluxes and the influence of the surface chemical state on their computation is still a topic, which has not achieved wide maturity in the community. This conclusion stems from the lack off agreement of most of the CFD tools with the experimental results.

For a general overview of the flow field, the only contour plots presented by Knight et al. are from the simulations of Walpot using a second-order accurate body-conformal finite volume solver. The relevant reaction rates are acquired from the work of Dunn and Kang [37], and Park [101]. Thermal conductivity and viscosity are obtained from the simplified mixture rule of Wilke [134] according to the curve fits of Blottner et al. [12]. For diffusion, Fick's law with a constant Lewis number of 1.2 is used. Most notably, the surface boundary condition was selected as a super-catalytic wall, forcing recombination to the concentrations of $N_2 = 0.7624$ and $O_2 = 0.2376$. Comparisons of the corresponding flow fields with standalone INCA and INCA with Mutation^{++} implementation are presented in Fig. (4.10) for Mach number and atomic nitrogen concentrations. Both INCA simulations have used the same grids and the same specifications to clearly compare the two results. This meant a non-catalytic surface state as it is the case for the standalone INCA. Apart from an extended subsonic region in the results of Walpot, the Mach number contours agree well in all three simulations. The differences start to appear in the atomic nitrogen contours, where a clear difference is present between the INCA and INCA-M^{++} results. Firstly, a lower concentration of atomic nitrogen in Walpot's results starting downstream of the shock may be due to the differences in the diffusion models. It could also be related to the differences in vibrational relaxation models causing a delay in dissociation reactions. This argument could be supported by Fig. (4.11), which is for a thermochemical nonequilibrium case under the same HEG I conditions. In this figure, the steep rise in the translational temperature is apparent in both contours. Note that the boundary layer regions are different as the thermal nonequilibrium solution assumed a non-catalytic surface. Although the general trends agree, the contours of Walpot indicate larger regions, where the vibrational temperature is dominant over the translational temperature. Most significantly, the vibrational temperature rises towards the shoulder of the cylinder, where the flow rapidly expands. The extent of this higher vibrational temperature region differs between the two simulations. Although they are expected to be similar to the current implementation, the exact parameters used by Walpot for vibrational relaxation are not provided.

Further investigating the contours of mass fractions of atomic nitrogen, one can trivially note the differences in the boundary layer regions in all three simulations. Although the grid resolutions are the same for both INCA simulations, a thicker boundary layer region similar to that of the reference result is predicted by INCA-M^{++}. This is attributed to a more accurate evaluation of the transport properties. The rationale behind this reasoning is based on the negligible differences expected in the other modules. That is, for this simple 5-species mixture, thermodynamic values are largely similar. Moreover, the outcome of chemical kinetics is to a good extent dictated by the reaction mechanisms, which are selected to be the same. This leaves the transport property evaluation as the most distinctive feature in both versions. The inadequacy of the mixture rules and collision integrals in the standalone solver for these environments has been discussed in Section 2.3, hence these results are directly indicative of the improvements that the current implementation brings. The difference between the results of Walpot at the wall stems from the super-catalytic boundary condition, effectively depleting the amount of atomic nitrogen in the boundary layer to force the concentrations to the prescribed values. A more appropriate comparison could be made between a fully catalytic simulation with INCA-M^{++} as given in Fig. (4.12). Here recombination at the wall is similarly visible. Recombination towards the wall is expected as the temperature drops in the boundary layer. Introducing catalysis incentivizes recombination at the surface and forces this reaction to directly release its energy to the solid. The actual impact of these observations on the surface state should be assessed based on the surface profiles.

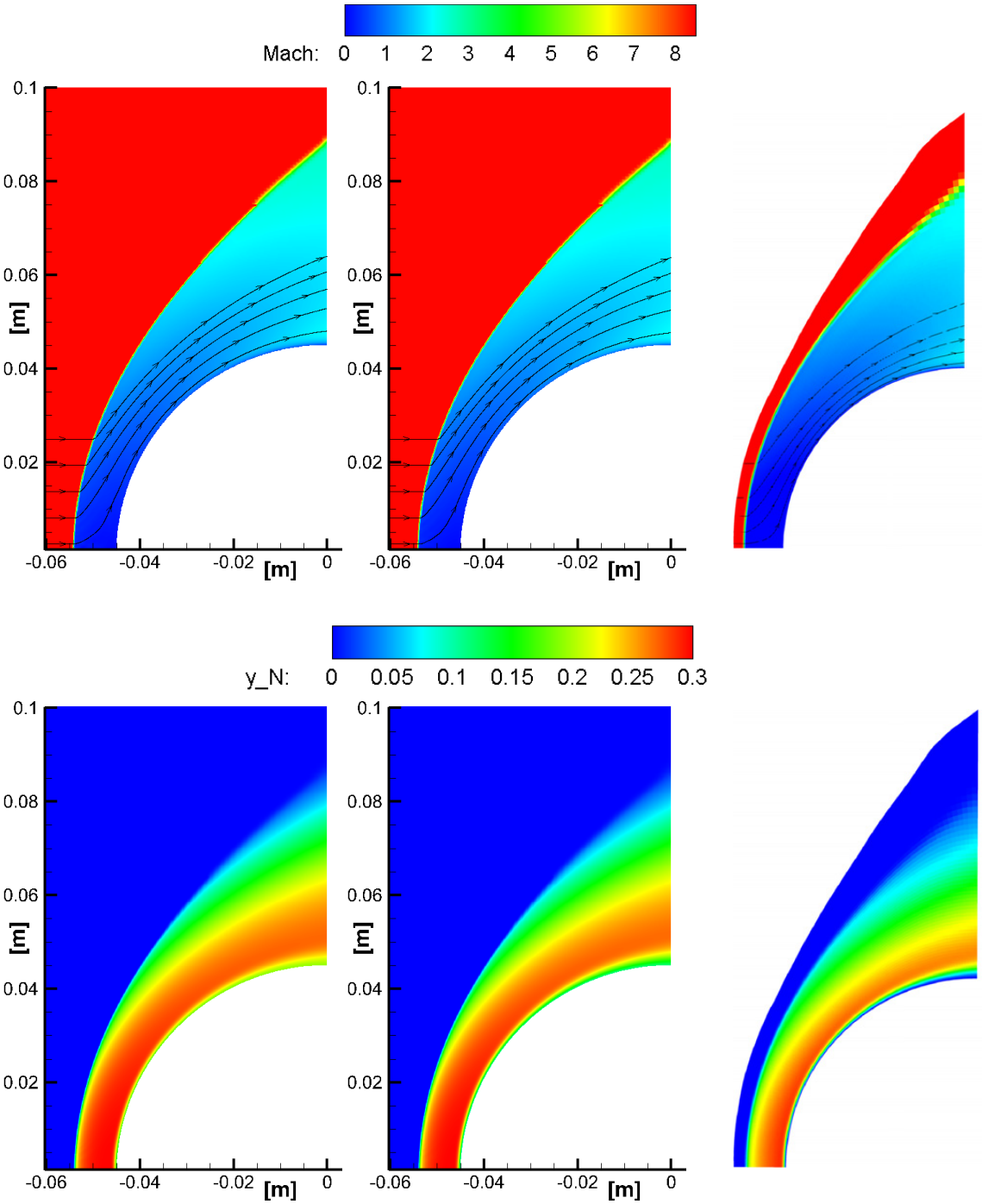

Figure 4.10: Comparison of Mach number (first row) and mass fractions of N (second row) contours for INCA (first column), INCA-M^{++} (second column), and the results from Walpot (third column) for HEG I conditions as presented by Knight et al.

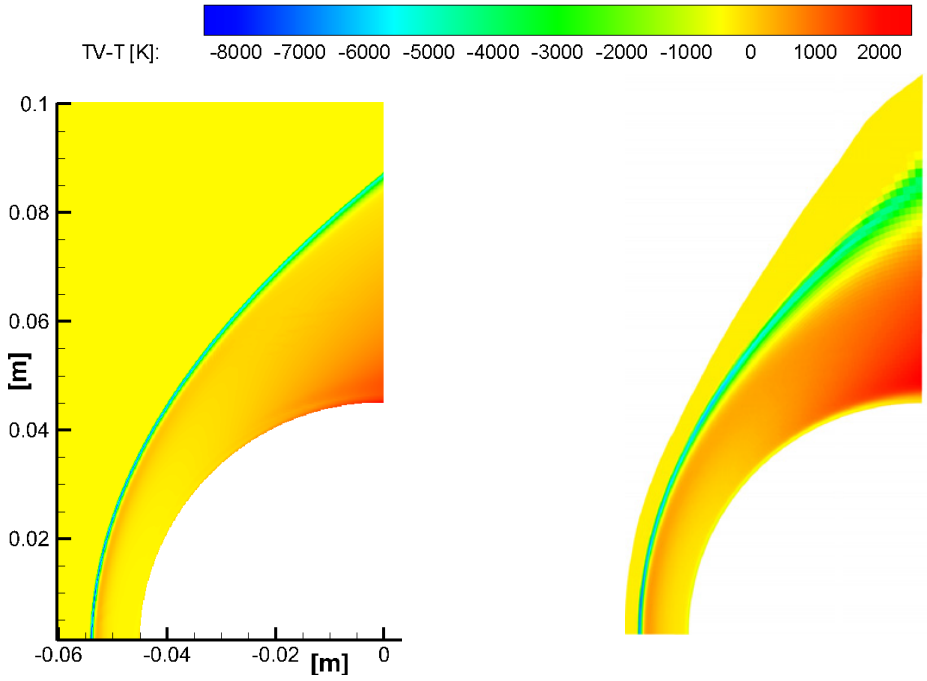

(a) (b)

Figure 4.11: Comparison of the difference between the vibrational and translational temperature contours for (a) INCA-M^{++} and (b) the results from Walpot for HEG I conditions as presented by Knight et al.

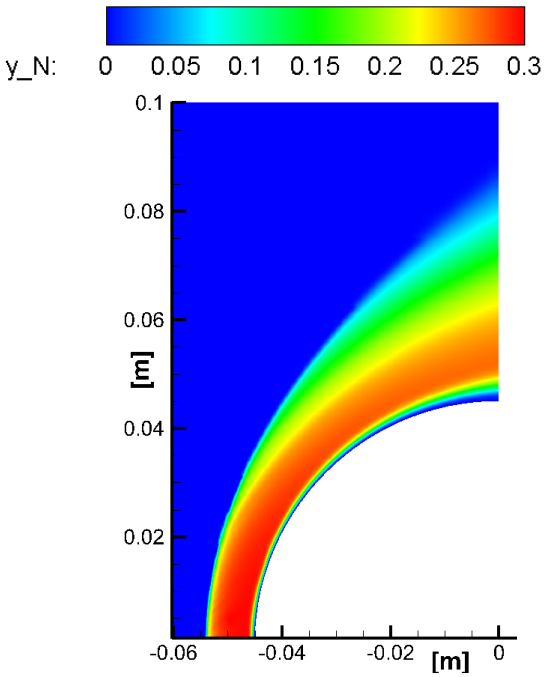

Figure 4.12: Mass fractions of N for the fully catalytic ($\gamma = 1$) INCA-M^{++} simulations for the HEG I conditions.

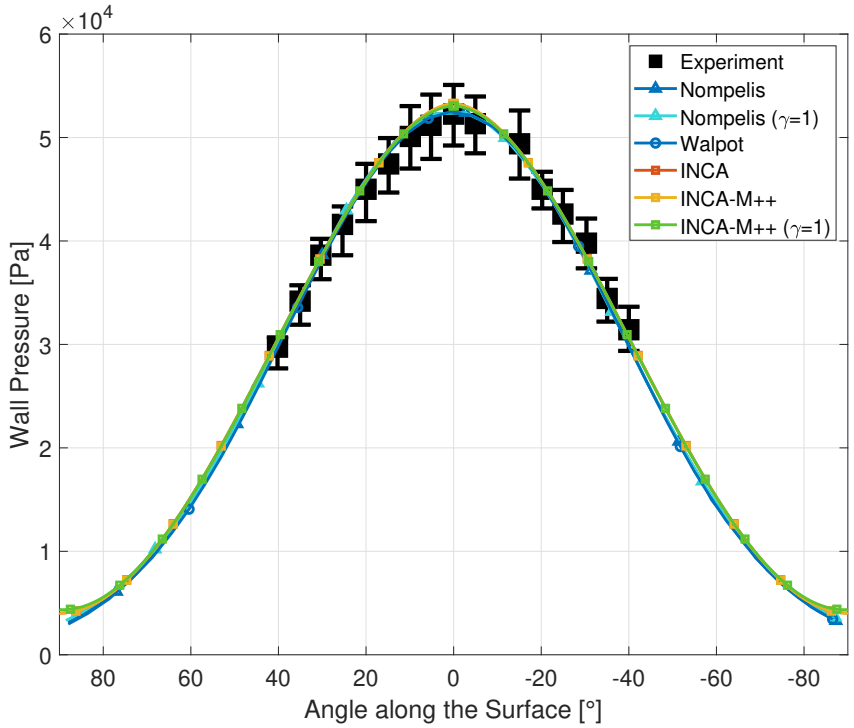

Figure 4.13: Comparison of pressures around the wall with the experimental values, non-catalytic and fully catalytic results from Nompelis, super-catalytic results from Walpot, INCA, and non-catalytic and fully catalytic results from INCA-M^{++} for the HEG I case from Knight et al.

For a more quantitative comparison, heat fluxes and pressures along the surface are compared. For this comparison, the results of Nompelis from Knight et al. are also included as those have shown significantly better agreement with the measurements compared to the other codes. This accuracy may partially be attributed to their additional consideration of surface catalyticity. Briefly, Nompelis have used a second-order accurate finite volume code with body-conformal grids, which is supposedly a predecessor of the US3D code mentioned in Section 1.3. In their simulations, they have used the reaction rates from Park [101], and obtained their transport properties similarly to Walpot. The comparisons are given in Fig. (4.13) and Fig. (4.14) for the HEG I conditions for pressure and heat flux distributions around the wall, respectively. The results extracted from Knight et al. include the experimental measurements, results of the simulations with the super-catalytic boundary condition from Walpot, and results for the non-catalytic and fully catalytic boundary conditions from Nompelis. In comparison to these, the current study investigated the performance of standalone INCA, and INCA with the Mutation^{++} implementation using non-catalytic and fully catalytic boundary conditions.

It must be noted that, while calculating the surface heat fluxes, some fluctuations were present in the profiles. These were absent for the pressure values. A first estimate suspected an insufficient grid resolution problem, yet the fluctuations were increasing for finer grids. Even though it is still unclear, these fluctuations might be an inherent artifact of the immersed interface approach with cut-elements. One explanation could be due to a sudden shift in the interpolation array used for the image points introduced in Section 3.3.1 for the cut-elements. As one traverses the interface, these fluid cell center values selected for the interpolation differ for the image point of each cut-element. It is probable that even adjacent cut-elements with slightly different inclinations could employ different sets of interpolation points, leading to a larger contrast between image point values for sharper gradients and coarser grids. This is especially relevant for a cylindrical shape as in this study, since the slope varies constantly and incrementally along the geometry. This could be a source of these fluctuations, yet further investigation is needed. Hence, the presented heat flux profiles are the fourth-order polynomial fits of these distributions. To quantify the acceptability of this way of representation, adjusted R-square values and the standard root mean squared errors are computed for the heat flux data and the

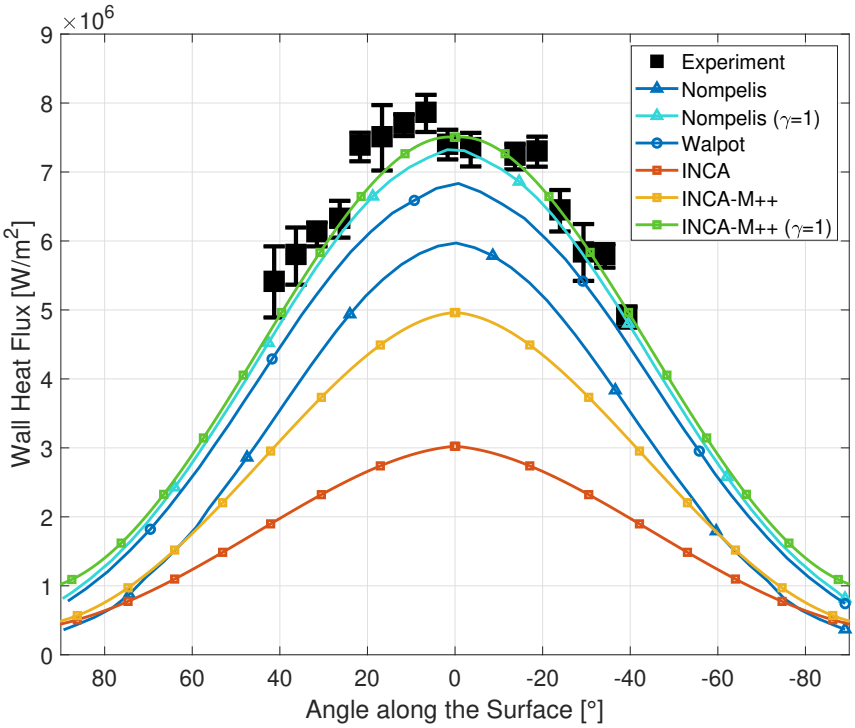

Figure 4.14: Comparison of heat fluxes around the wall with the experimental values, non-catalytic and fully catalytic results from Nompelis, super-catalytic results from Walpot, INCA, and non-catalytic and fully catalytic results from INCA-M^{++} for the HEG I case from Knight et al.

corresponding polynomial fits. These values provide a confidence level for how well the fit represents the given data, with values of R-square closer to 1 and small root mean square errors indicating less variance in the data set. For the results in this study, the adjusted R-square values were mostly around 0.99 with the lowest value recorded as 0.97. The root mean squared errors are on the order of 10^{-4}, which is acceptable for the heat flux values of over several million units.

The pressure distributions are matched by all simulations in Fig. (4.13). This has been the case with INCA even for significantly coarser grids. However, capturing the heat flux profile requires much more attention. As it can be seen from Fig. (4.14), both the standalone and the newly developed non-catalytic INCA simulations fall short of the experimental measurements and other predictions. Standalone INCA predicts the lowest heat flux out of all simulations with an approximately 60% difference at the stagnation point compared to the measurement results. Although they host the same grids, the non-catalytic INCA-M^{++} results are still much closer to the other predictions. This is expected to be largely based on the considerably more accurate multicomponent system solution provided by Mutation^{++} for the transport properties, especially for thermal conductivity for the heat flux calculation, as opposed to the simplified transport properties in standalone INCA. Moreover, collisional data for these calculations are obtained from an accurate database with Mutation^{++}, instead of an empirical approximation used by the standalone solver. Although noticeably better, these non-catalytic results are still 34% lower than the expected results at the stagnation point, which signals that the cause of the discrepancy is due to the absence of an appropriate physicochemical surface model, as will be seen.

Large differences are also present between the results of Nompelis and Walpot, which might be due to a difference in grid resolutions. Throughout this study, it was found through various trials that coarser grids on the order of 10^{-4} m are strictly unsuitable for predicting the heat flux as they do not resolve the thermal boundary layer sufficiently. An adequate surface resolution adopted by most body-conformal grids is usually on the order of 10^{-6} m. For Cartesian grids, the lack of similar studies renders this requirement more ambiguous, even more so for the cut-element approach of this work. It was observed that imposing smaller minimum cell sizes with the adaptive Cartesian grid approach significantly increased the total number of cells, and consequently the computational cost.

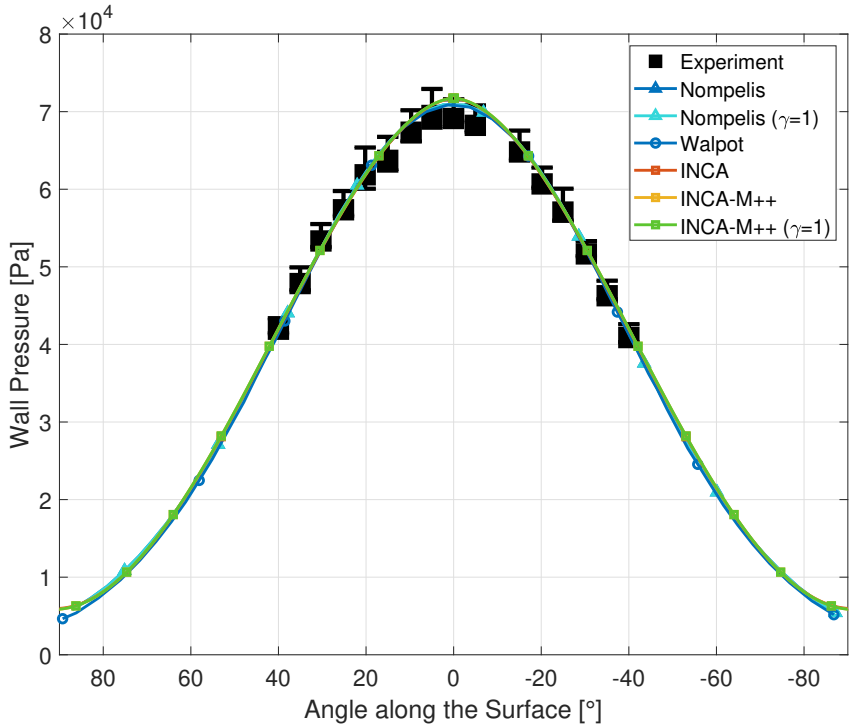

Figure 4.15: Comparison of pressures around the wall with the experimental values, non-catalytic and fully catalytic results from Nompelis, super-catalytic results from Walpot, INCA, and non-catalytic and fully catalytic results from INCA-M^{++} for the HEG III case from Knight et al.

A grid convergence study might have been beneficial, but it could not be carried out as successive refinements demanded sharp increases in resources. This was an important drawback in this study and its limitations will be discussed in Section 4.4. Therefore, the presented INCA solutions were carried out with smallest cell sizes on the order of 10^{-5} m. This might partially explain the differences in the non-catalytic heat flux profiles between Nompelis and INCA-M^{++}.

Continuing with Fig. (4.14), it can be seen that the simulations which are most successful in matching the experimental measurements are the ones with the fully catalytic wall states from INCA-M^{++} and Nompelis, with INCA-M^{++} being only 1.4% higher and Nompelis being 1.1% lower with respect to the closest measurement location around the stagnation point. Both results are well within the given uncertainty ranges. This result remarks the crucial impact of including an appropriate surface state in high temperature applications. The simplistic super-catalytic boundary condition from Walpot does not succeed in representing the heat flux profile. Accounting for surface recombination reactions requires an accurate mass balance for the influence of diffusion. The addition of the diffusive heat flux drastically amplifies the heat flux estimations. INCA-M^{++} and Nompelis are mostly in good agreement with each other. INCA-M^{++} simulations predict a slightly higher heat flux, which is in fact closer to some of the measurement points.

A similar conclusion can be drawn for the HEG III cases presented in Fig. (4.15) and Fig. (4.16). The pressure profiles are again in good agreement with all simulations. The heat flux profiles on the other hand showcase clear distinctions. The HEG III case is a lower enthalpy case associated with a less severe heating environment. Hence, all results are able to match the measurements up to a certain degree of accuracy, except for the standalone INCA solution, which underpredicts the stagnation point heat flux by approximately 50%. The non-catalytic INCA-Mutation^{++} simulation also gives out a 22% lower value at the stagnation point. Most favorable predictions are again the ones from INCA-M^{++} and Nompelis with the fully catalytic boundary condition, having only 4.4% and 2.2% higher predictions than the nearest measurement location around the stagnation point, respectively. For this condition, INCA-M^{++} slightly overpredicts the reference values, although it is still within the range of tolerances for most of the measurement locations.

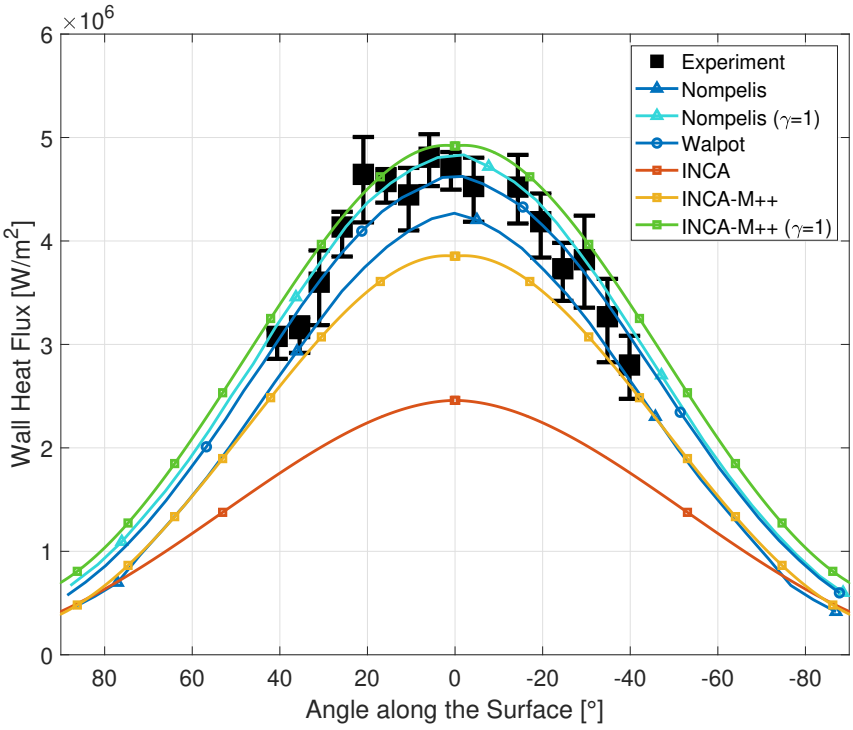

Figure 4.16: Comparison of heat fluxes around the wall with the experimental values, non-catalytic and fully catalytic results from Nompelis, super-catalytic results from Walpot, INCA, and non-catalytic and fully catalytic results from INCA-M^{++} for the HEG III case from Knight et al.

4.2.1. Comparison with US3D-Mutation^{++}

An additional study was compared with the contemporary US3D code through a collaboration with VKI. This version of US3D was also being coupled to Mutation^{++}, which allowed verifying the implementations in both codes. In addition to the viscous case, the same test conditions for HEG I are evaluated for an inviscid assumption to be compared by both codes. The simulations are run for thermal equilibrium for both cases. Since properties along the stagnation line were not presented by Knight et al. [63], the purpose of this comparison was to gain confidence over the shock layer region as well.

The comparisons are presented for the inviscid case in Fig. (4.17) and Fig. (4.18), and for the viscous case in Fig. (4.19) and Fig. (4.20), for the temperature and mass fraction distributions, respectively. Standalone INCA is omitted in the inviscid case as it did not provide acceptable results. In both conditions, results of US3D and US3D with Mutation^{++} implementations mostly overlap. As US3D is already a well-established solver, this agreement gives further confidence in the models used in Mutation^{++}. The grid resolution was finer at the shock for INCA and finer at the wall for US3D. Hence, the shock is sharper for INCA simulations, yet the boundary layer in the viscous solutions is resolved better by US3D. The shock standoff distances are still in line between US3D and INCA-M^{++}, while standalone INCA predicts it at a slightly upstream location. Once again, the boundary layer is estimated to be in a better agreement with the US3D results, with Mutation^{++} implementations compared to standalone INCA operating on the same grid resolution. INCA predicts a thinner thermal boundary layer and for the same minimum cell distance from the wall, it overpredicts the boundary layer temperature. Whereas with Mutation^{++} implementations, a thicker thermal boundary layer prediction corresponds to an almost exact match of the temperature distribution close to the wall with US3D.

Mass fractions of all the species are in good agreement between the simulations. Since the freestream contained a large concentration of atomic oxygen, it does not show a significant increase in the logarithmic scale. Compared to the first campaign, here sufficiently high shock temperatures lead to a notable amount of dissociation for nitrogen. There is a slight mismatch for NO around the shock and close to the wall, which was later identified to be due to an older version of the reaction mechanism used by US3D simulations. For the viscous case, it could be observed from the rapid decrease in the

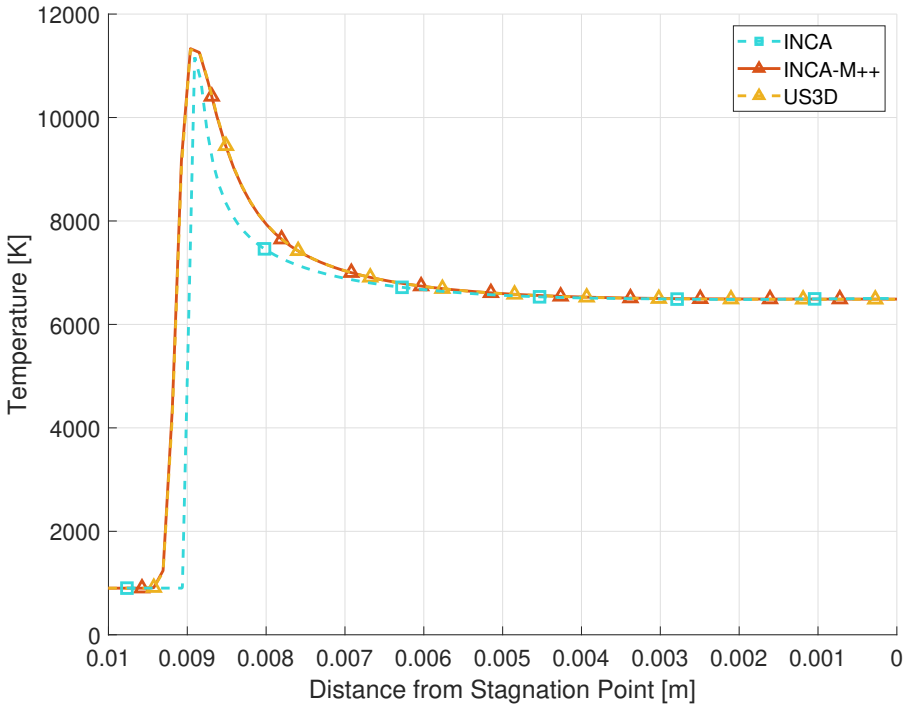

Figure 4.17: Comparison of temperatures along the stagnation line for INCA-M^{++}, US3D, and US3D-M^{++} for the HEG I case from Knight et al. assuming inviscid flow.

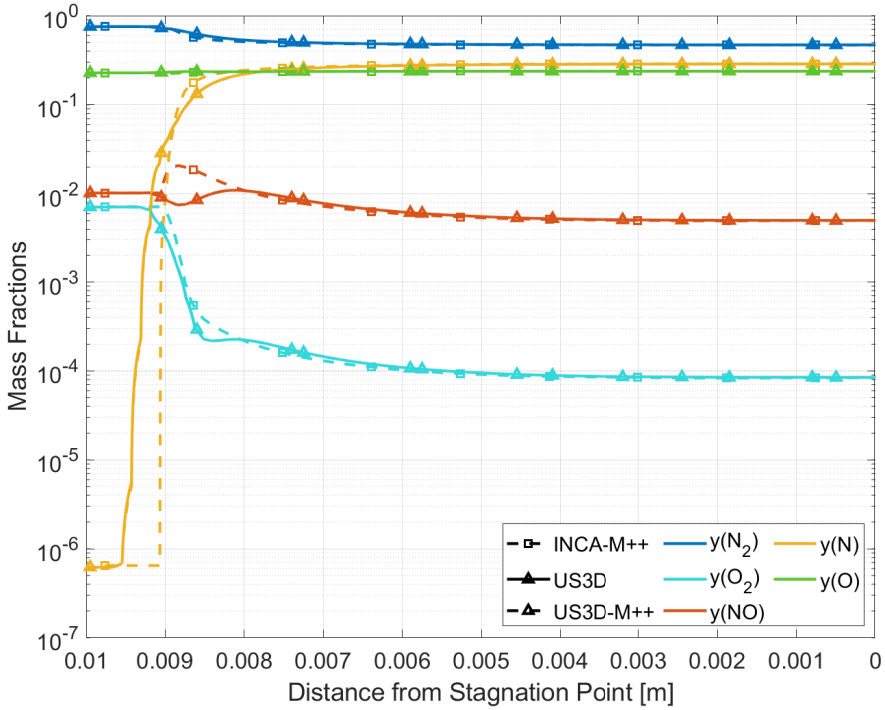

Figure 4.18: Comparison of species mass fractions along the stagnation line for INCA-M^{++}, US3D, and US3D-M^{++} for the HEG I case from Knight et al. assuming inviscid flow.

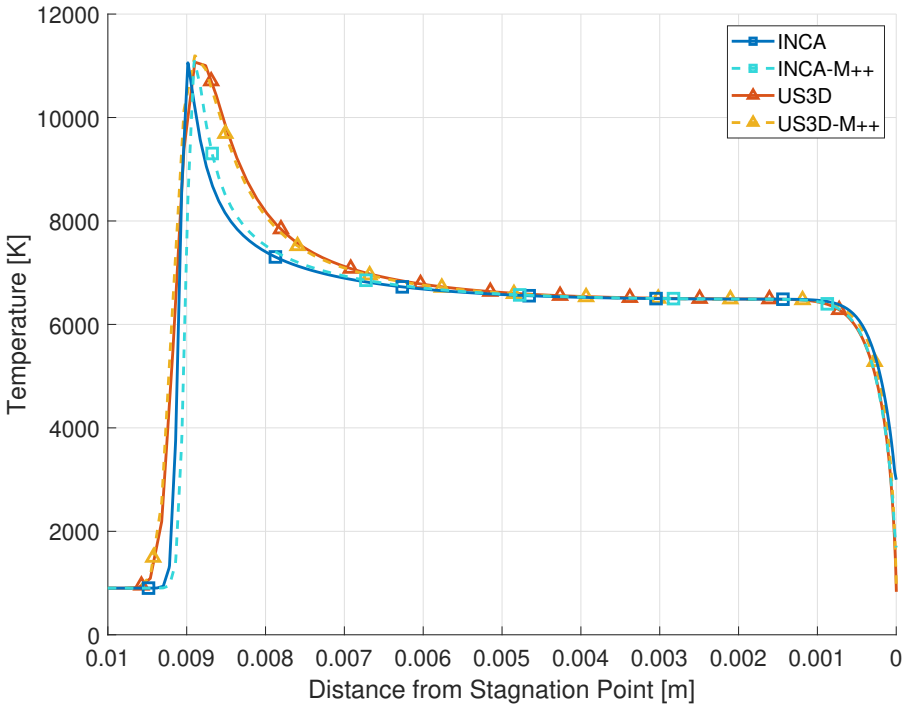

Figure 4.19: Comparison of temperatures along the stagnation line for INCA-M^{++}, US3D, and US3D-M^{++} for the HEG I case from Knight et al.

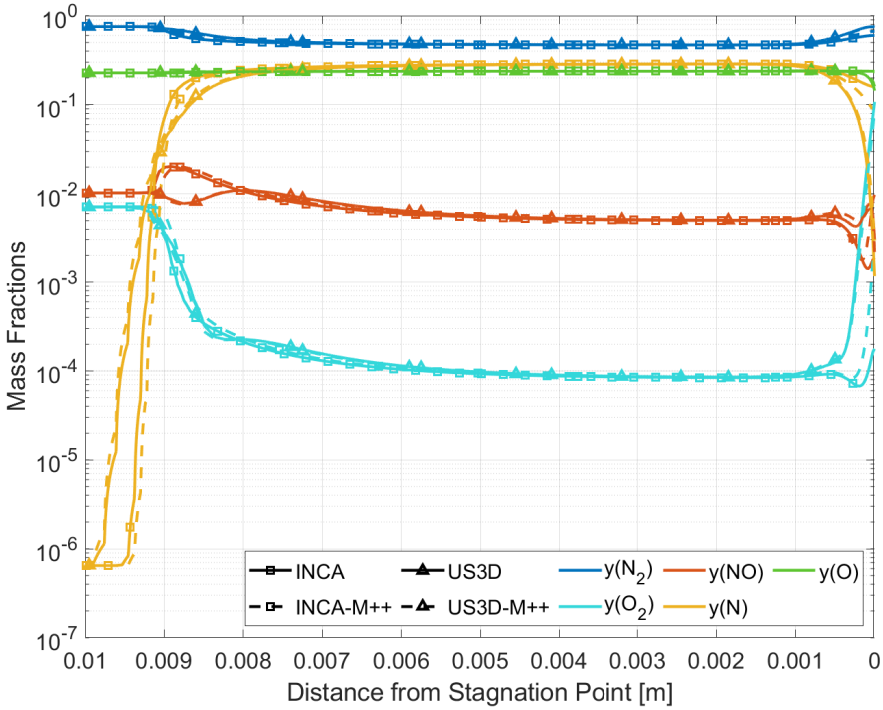

Figure 4.20: Comparison of species mass fractions along the stagnation line for INCA, INCA-M^{++}, US3D, and US3D-M^{++} for the HEG I case from Knight et al.

atomic species mass fractions, that dissociated species begin to recombine as they approach the cold wall. Discrepancies close to the wall are present due to the different surface resolutions. Nevertheless, Mutation^{++} implementations are closer to the US3D results when compared to standalone INCA.

This comparison concludes the test cases from Knight et al. A thorough comparison with reference results for all relevant aspects of the simulations have been presented. It is concluded that the new implementations have operated successfully under the given conditions.

4.3. Mass Blowing due to Ablation

In the third campaign, an application with ablative surface reactions is investigated. For this purpose the test case from Chen and Milos [25] is reproduced with the newly developed GSI implementations within INCA. The general conditions for the test case have been given in Table 4.1. The complete geometry consists of a graphite sphere and a cone. As the heat fluxes are most severe around the sphere and ablation is prominent there, the cone section is neglected and only the 80° cylinder is considered. Reference results are available from an arc-jet experiment at the Interactive Heating Facilities at NASA Ames Research Center. The freestream conditions describe a fully dissociated oxygen and partially dissociated nitrogen flow at a Mach number of 5.84. Freestream total enthalpy is approximated to be 27 MJ/kg with a total stagnation pressure of 0.80 atm. This test case was also studied more recently by Mortensen and Zhong [90]. Results from both references will be compared with the current development.

Chen and Milos have used an implicit flux-splitting finite volume flow solver. Transport properties were calculated based on the work of Yos [52]. In their simulations, they have employed four different surface models. Two of them from Park [102], which mutually consider oxidation and sublimation of C_3 and one of them additionally considers nitridation. The third model is the one proposed by Zhluktov and Abe [140], which considers oxidation, sublimation and surface recombination reactions. Lastly, the fourth model assumes chemical equilibrium at the surface.

Mortensen and Zhong's solver on the other hand uses a high-order shock-fitting method. Unlike a shock capturing scheme, post-shock conditions are calculated from Rankine-Hugoniot relations. A fifth-order upwinding scheme and a sixth-order central scheme is used to discretize the inviscid and viscous terms, respectively. Explicit third-order Runge-Kutta method is used to march in time. Viscosity is obtained from curve fits of Blottner et al. [12] and the mixture values are computed by Wilke's rule [134]. Diffusion is calculated through Fick's law for a constant Schmidt number. Their surface model is similarly based on the work of Park [102] including oxidation, sublimation and recombination of atomic oxygen.

The current study follows Park's surface model like Chen and Milos for sublimation, but includes surface recombination similar to Zhluktov and Abe, and uses the same reaction parameters for ablation as Mortensen and Zhong. Similarly to Mortensen and Zhong, nitridation is neglected due to its uncertain probability coefficient for this case. In addition to the 5-species air model without ionization used in the previous campaigns, additional carbon based species CO_2, CO, CN, C_3, C_2, C are considered for a total of 11 species. Reaction mechanisms for this mixture are given in Appendix B. The surface reactions are given explicitly according to the reactive efficiency models discussed in Section 2.6.1 as

$$C_{(s)} + O \xrightarrow{(1)} CO\,, \tag{4.1}$$

$$C_{(s)} + 2O \xrightarrow{(2)} C_{(s)} + O_2\,, \tag{4.2}$$

$$3C_{(s)} \xrightarrow{(3)} C_3\,, \tag{4.3}$$

in order, they stand for oxidation, surface recombination and sublimation. The reaction probabilities of oxidation and recombination reactions are given as

$$\eta_1 = 0.63 \exp\left(-1160/T_w\right)\,, \tag{4.4}$$

$$\eta_2 = 0.63 \exp\left(-1160/T_w\right)\,. \tag{4.5}$$

The rate of production for the sublimation reaction is

$$\dot{\omega}_{C_3} = \eta_3 \left(\rho_{C_3,\text{equil}} - \rho_{C_3}\right) \sqrt{\frac{k_B T_w}{2\pi m_{C_3}}} \tag{4.6}$$

where η_3 is the vaporization coefficient taken as unity [100], and $\rho_{C_3,\text{equil}}$ is the equilibrium surface density of C_3 and it is given through the corresponding saturated vapor pressure expression as [5]

$$p_{C_3,\text{equil}} = 5.19 \times 10^{14} \exp\left(-90908/T_w\right) . \tag{4.7}$$

An important simplification done for this test case is that a uniform temperature wall is assumed as opposed to the predicted temperature profile in the reference. Immersed boundary models within INCA were build for an adiabatic or isothermal wall boundary condition. With the addition of the GSI module from Mutation^{++}, these were extended with surface reactions. For this campaign, the surface temperature distribution based on the experimental measurements has been implemented. This distribution defined the surface temperature for cut-cell interfaces and for ghost point extrapolation. However, results with this varying surface temperature were suffering from large oscillations. Hence, an average isothermal temperature of 3250 K was used instead. This average temperature is achieved approximately at and around 1.5 cm along the cylinder, which is hereby referred to as the middle section. Close to the stagnation point temperatures reached around 3500 K and at the shoulder they dropped to around 2800 K. Although discrepancies are expected at these regions, this also allows examining the impact of surface temperature on heterogeneous reactions.

The flow field is shown in Fig. (4.21) with Mach number, pressure, and temperature contours for INCA-M^{++} simulations. None of the references have presented these contours so a visual comparison was not possible. These contours with the current development display a well defined shock and a stagnation region towards the body. Shock standoff distance is around 0.021 m and the peak temperature at the shock is 10 300 K. In Fig. (4.22), contour plots for the main ablation reactants and products are also provided. It can be seen that the freestream already contained a large quantity of dissociated oxygen. This atomic oxygen is depleted at the surface due to catalytic recombination and oxidation. Consequently CO is formed, and even sublimation product C_3 is produced due to the hot wall. These products are convected downstream and they also diffuse into the flow, creating this mixing layer towards the shoulder of the cylinder. Since the surface is at a very high temperature, even for common conventions, surface reactions occur very rapidly. Then, the reaction rates become sufficient enough to consume all the diffusing reactants at the surface, making the mixture approach a state of equilibrium between the gas and solid mediums. At such an instance, the ablation process, oxidation in this case, is said to be diffusion limited. That is, the reaction rates have reached a point where further speed-up does not alter the production rates, as the reactions are limited by the amount of reactants made available through diffusion. This threshold varies according to the surface temperature. Surface reaction rates might again become the limiting factor if they possibly slow down over a cooler surface. Near equilibrium behavior is most clearly observed from surface profiles.

Comparison with the reference results are presented as surface profiles. Variation of surface pressures, mass blowing rates and surface heat fluxes are plotted with respect to the radial distance along the cylinder, starting with zero at the stagnation point. Considering wall pressure first in Fig. (4.23), it could be seen that all codes are in a good agreement and match the measurement at the stagnation point. Marginally higher pressures are calculated with INCA-M^{++} towards the shoulder of the cylinder. As the mixture state that predicts the pressure is a function of many variables, this difference could be attributed to the dissimilarities in flow, surface temperatures and physicochemical models for the solvers.

Consider now Fig. (4.24) for mass blowing rates and Fig. (4.25) for total surface heat fluxes. The impact of the initial assumption of an isothermal wall could be clearly seen in these figures. At the stagnation point, a lower temperature has resulted in slower reaction rates, and consequently less surface blowing. Near the shoulder, the wall temperature is higher than anticipated so it yields larger mass blowing rates compared to the other results. Similarly, heat flux prediction at the stagnation point is much higher than the other simulations as the relatively colder surface amounts to a larger gradient. Whereas towards the shoulder the opposite is true and the heat flux is less than the other simulations. It is at the middle section, in the vicinity of around 1.5 cm, that an applicable agreement is found as this is the region where wall temperature of INCA-M^{++} is aligned with the other simulations. For the mass blowing rates, INCA-M^{++} results match the middle section measurement point (at 45°) better than the other simulations. For the heat fluxes, INCA-M^{++} results behave similar to Zhluktov and Abe, although the overall surface profile is not captured well, as the heat flux is very sensitive to the temperature distribution. It is interesting to note that this sensitivity is less effective for the mass blowing rates. This argument is supported by the similar profile shape of the mass blowing rates

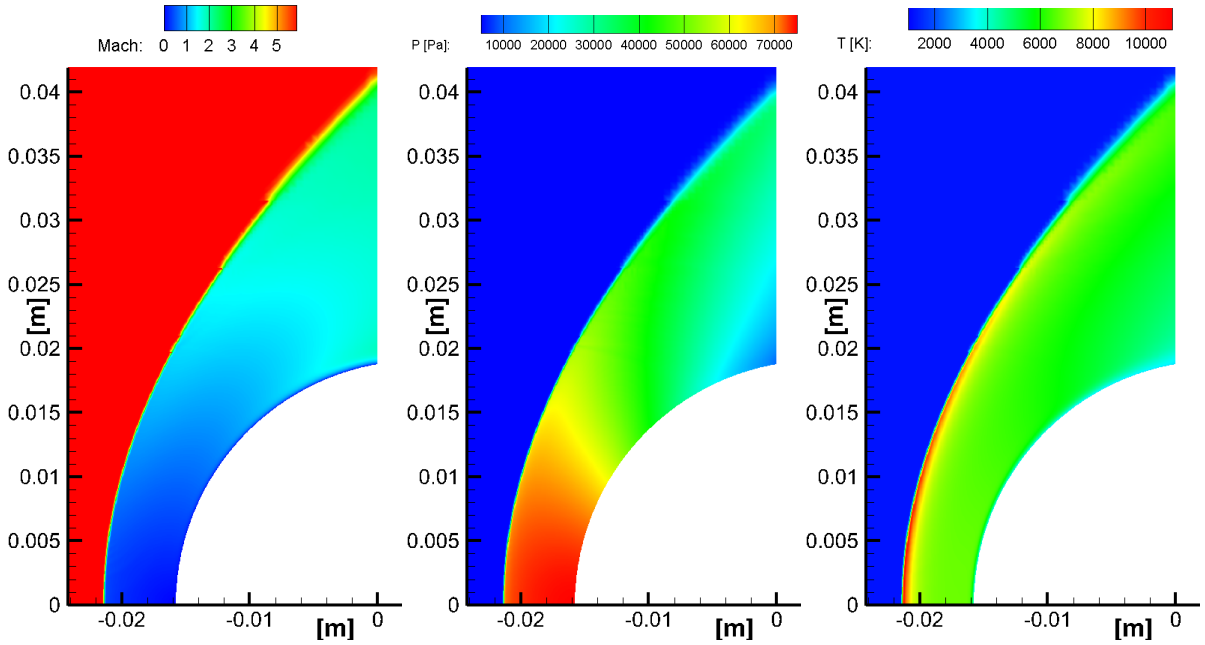

Figure 4.21: Contours of (a) Mach number, (b) pressure, and (c) temperature obtained with INCA-M^{++} for the case from Chen and Milos.

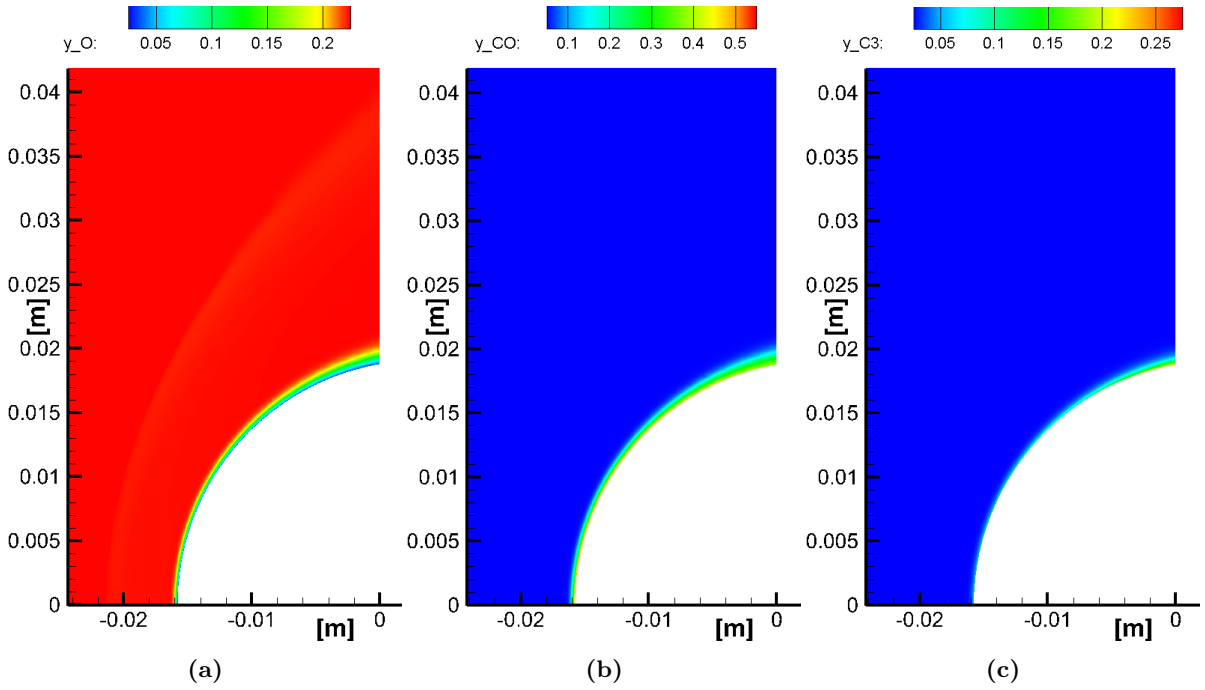

Figure 4.22: Contours for mass fractions of (a) O, (b) CO, and (c) C_3 computed with INCA-M^{++} for the case from Chen and Milos.

obtained by the current development compared to the other simulations. This could be explained by the heat flux having a more direct dependence on the surface temperature.

Based on the middle section results, it could be hypothesized that the INCA results with the Mutation^{++} implementation would behave similar to the results of Mortensen and Zhong, which are similar to the surface equilibrium assumption results of Chen and Milos. As already discussed, the sufficiently hot wall is indeed forcing a diffusion limited ablation process. Adopting the equilibrium

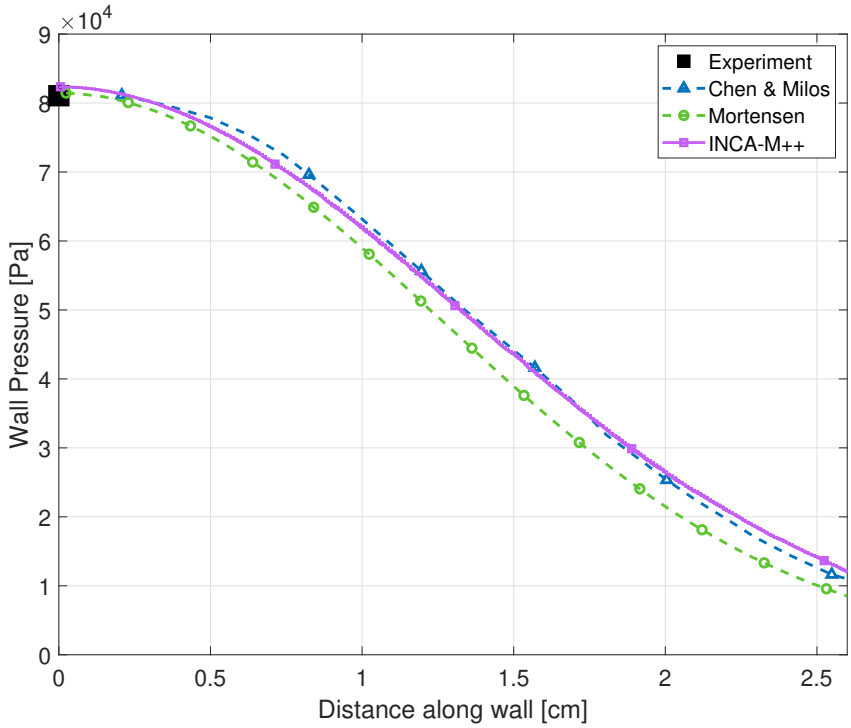

Figure 4.23: Comparison of pressures around the wall with the reference results and the results with the ablative boundary condition in INCA-M^{++} for the case from Chen and Milos.

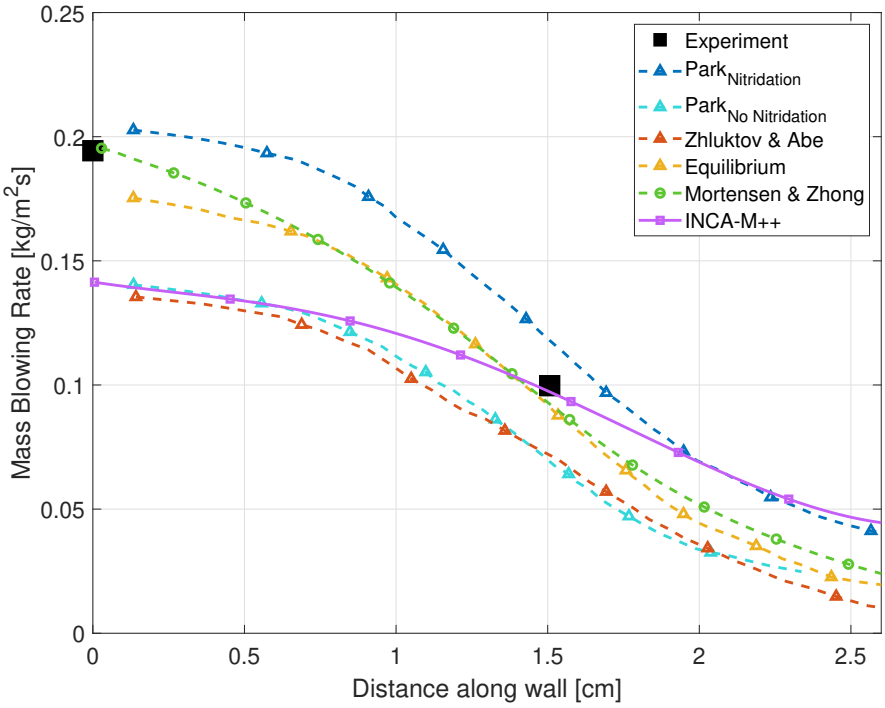

Figure 4.24: Comparison of mass blowing rate around the wall with the reference results and the results with the ablative boundary condition in INCA-M^{++} for the case from Chen and Milos.

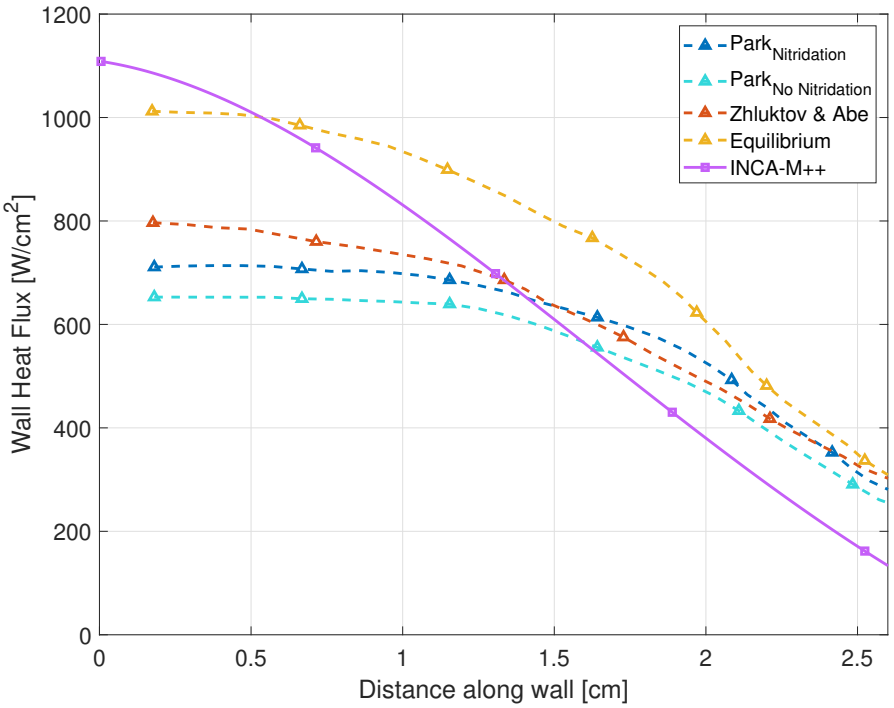

Figure 4.25: Comparison of heat fluxes around the wall with the reference results and the results with the ablative boundary condition in INCA-M^{++} for the case from Chen and Milos.

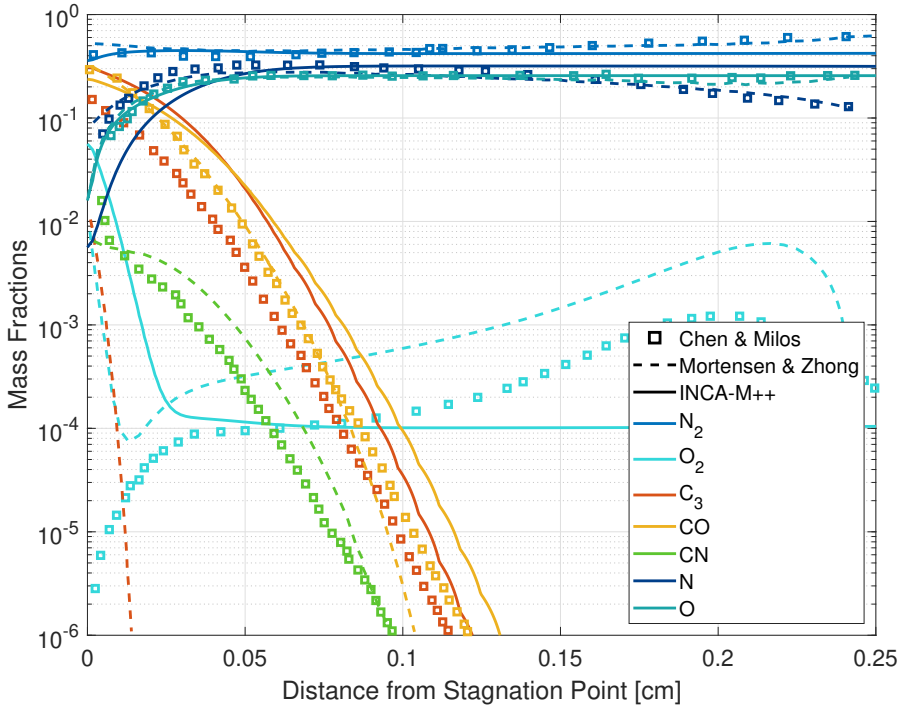

Figure 4.26: Comparison of species mass fractions around the wall with the reference results and the results with the ablative boundary condition in INCA-M^{++} for the case from Chen and Milos.

assumption and disregarding the chemical reactions could be reasoned as a more efficient approach for this case. However, discrepancies could not be avoided and anticipated with such an assumption, when chemical equilibrium is no longer maintained. Even for this unconventionally hot wall case, this could be highlighted by the differences between the results of Mortensen & Zhong and the equilibrium case at the stagnation point and at the shoulder. Mortensen and Zhong does not present their heat flux results and no measurement is available on the body to assess the accuracy of finite-rate surface reactions compared to the equilibrium assumption.

Lastly, mass fractions along the stagnation line are presented in Fig. (4.26). Since surface recombination is not included in the surface chemistry model of Chen and Milos, the steep rise in the fraction of O_2 is only present for INCA-M^{++} and Mortensen & Zhong. For INCA-M^{++}, including oxygen recombination at surface has lead to less atomic oxygen available for oxidation reactions. Which meant that the surface was more severely limited by diffusion, and consequently the mass blowing rate was lower. Sublimation reaction was unaffected by this limitation, yet the lower temperature around the stagnation region meant slower reaction rates and less blowing as well. The absence of CN and the variations away from the surface for the INCA-M^{++} results is expected to be due to a convergence error in the chemical reactions, which should be further investigated. Considering the two major ablation products, CO and C_3, similar magnitudes and behavior is seen between all codes. Here, the sublimation model considered for INCA-M^{++} was the same for Chen and Milos, which could be seen from the agreement between them and the disparity with Mortensen and Zhong.

In conclusion to this campaign, it was observed that the newly developed immersed interface gas-surface interactions implementation with Mutation^{++} performs well compared to reference results. Locally good agreement is obtained, but a better agreement should be obtained with an appropriate temperature distribution and possibly with a reduced surface recombination probability. Taking into account how all the reference codes are vastly different from the current development in terms of numerical and physicochemical modeling approaches, the agreement in these results is indeed promising.

4.4. Computational Cost Analysis

The preceding sections have demonstrated the capabilities of the developments made in this study. This section compiles statistics from previously presented test cases and various other trial cases simulated throughout the span of this project to assess the computational cost of these new implementations from Mutation^{++}. The implementations are categorized under three branches. First one includes the baseline implementations for simulating chemical nonequilibrium with the coupled thermodynamics, transport properties and chemical kinetics modules. The second category considers the thermal nonequilibrium implementation with the vibrational energy conservation equation. The third group considers gas-surface interaction implementations with the additional immersed boundary modifications. In line with the nomenclature of this thesis, these are referred to as CNE, TTV and GSI categories. The collection of these categories include 50 relevant simulations once the outliers are eliminated. Among these, 35 simulations are with CNE, 3 are with TTV, and 12 are with GSI.

The computational cost assessment will consider the required processor times of each simulation to solve for a set amount of simulation time. This duration is taken to be 2.5 ms for the current cases. These processing times will be compared to the number of cells in the solution domain and the selected thermochemical flow model. Then, the percentage of computational overhead is calculated by taking the standalone INCA solution statistics of the same simulation as the reference state, and comparing it to the different implementation categories. Note that in this comparison, solutions restarted from a previously established simulation are not included. Such a way of practice is often more efficient and is frequently employed, but it might be misleading in terms of cost assessment.

The total processor times are presented in Fig. (4.27) and the percentage of overhead is given in Fig. (4.28). Each point in these graphs represent the average of various different simulations with that same grid and flow model. As expected, more complex physicochemical models have lead to higher processing times compared to reference standalone simulations. However, a large spread of results could be observed from the graphs. An increase in the number of grid cells does not necessarily lead to an increase in the processing times. These large variations are most probably due to differences in different processor types and quantities used for some of these simulations. Some of the partitions in TU Delft's HPC12 cluster use standard Ethernet for connections between nodes, while others use the significantly faster InfiniBand connection. Unfortunately, the waiting times on the job queue are much

longer for these faster partitions. The performance of a simulation also depends on the scalability of that problem to a certain number of processors. For some of these grids, a poor scalability might have resulted in performance losses due to excessive processor communication. Another crucial aspect in this variation is that throughout this project, both the main development code and the interface written for the implementations continued progressing and evolving. The new Mutation^{++} implementations were continuously adapted to the most recent developments in the main distribution. Most of these changes either directly or indirectly influenced the efficiency of the solver, often leading to a more optimized performance. Comparing solutions of different versions of the solver could have lead to these large differences in the processing times of the simulations.

For a more representative comparison, it is better to compare the simulations performed with the latest development, with the same number of identical processors, on the same grid. This set of solutions corresponds to the simulations for the grid with 720 000 cells on the plots. The exact overhead values of these simulations with the corresponding processor times are given in Table 4.2. Similarly, identical parameters are compared for the same grid size with non-catalytic, catalytic and ablative boundary conditions in Table 4.3.

Table 4.2: Processor times and overhead percentages for CNE and TTV implementations based on the reference standalone values from the grid with 720 000 cells.

	CNE	**TTV**
CPU time [s]	6.169×10^{6}	7.892×10^{6}
Overhead	64%	110%

Table 4.3: Processor times and overhead percentages for CNE, catalytic GSI, and ablative GSI implementations based on the reference standalone values from the grid with 145 600 cells.

	CNE	**GSI$_{\text{catalytic}}$**	**GSI$_{\text{ablative}}$**
CPU time [s]	5.739×10^{6}	6.437×10^{6}	2.612×10^{7}
Overhead	60%	198%	1018%

Both simulations presented in these tables are performed on a single node with 32 AMD Opteron 6136 processors having relatively slow 2.4 GHz clock speeds. Main sources of higher computational demand are due to the calls to the external library, evaluation of multicomponent transport systems, addition of a secondary energy conservation equation for the vibrational thermal bath, and the surface balances at the gas-surface interface. Further improvement is foreseen by optimizing the parameters for the chemical source term solver. In a standard simulation with CNE, approximately 26% of all computational time was spent on the calculation of the transport properties. This is an expected amount considering the rigorous transport system calculations. In CFD simulations with accurate modeling of thermodynamic state and transport properties, it is not unusual that a major part of the computational resources have to be allocated for these calculations. In an example with INCA, vapor-liquid flash calculations near the coexistence line consumed about 75% of the CPU time in the LES of transcritical jets [81]. These overhead percentages are comparable to the coupling of Mutation^{++} with the US3D solver. In fact, more efficient processing times are reported by the current development for chemical nonequilibrium calculations. This is mainly attributed to having direct access to the source code of the flow solver and an efficient implementation procedure.

Including GSI is seen to be an exceptionally costly addition. It can be seen that a catalytic condition does not necessarily increase the cost remarkably, but with the additional ablative reactions, the cost drastically goes up. This is largely due to the increase in the number of species considered. Instead of the 5-species mixture considered throughout this study, ablative reactions considered 11 species. There is no denying that the surface balance computations discussed in Section 2.6.2 entail high processing times. This is partly due to solving the balance itself, but largely attributed to computing diffusive fluxes with the Stefan-Maxwell approach as in Eq. (2.52), which is known to be a rigorous method. Additionally, the GSI implementation discussed in Section 3.4.2, made it necessary to call the library for the ghost-cell

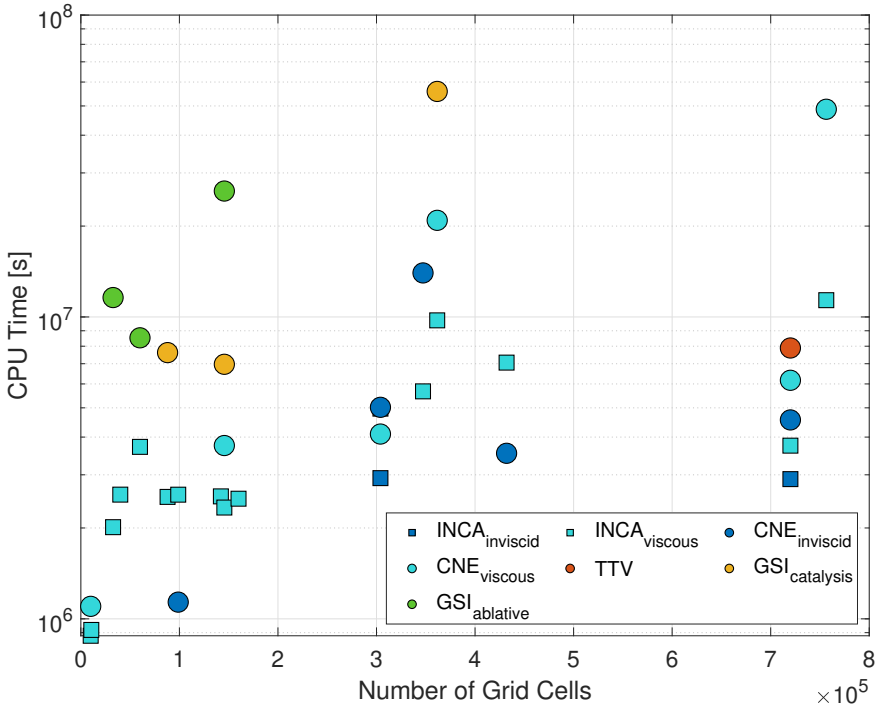

Figure 4.27: Comparison of processor times of various simulations. Each point represents the mean of all the simulations with that same grid size.

evaluation and also for the interface fluxes to be compatible with the immersed interface methodology. Moreover, as these cut-cells require significantly more computational time compared to the surrounding fluid cells, within the same partition block, they limit the progression of the solution. These aspects are the main causes of the drastic cost increase for ablative simulations. Suggested optimizations to alleviate these include saving the cut-element solution to avoid the GSI call in the ghost-cell extrapolation, and a more efficient load balancing strategy to avoid a limiting cut-cell for a given grid block.

Another major increase in the costs was due to the exponential rise in the number of cells, when smaller minimum cell sizes were specified at the surface. Since it is inherently more difficult to capture the shape of an object with Cartesian grids, significantly more cells in total are usually required to achieve the requested surface resolution. For example, for the same problem, when a minimum cell size of 10^{-4} m corresponds to 145 600 total cells, for 10^{-5} m it goes up to 756 400 cells, and for 10^{-6} it reaches 1 424 400 cells. This was an important drawback in this study, which limited the resolution of the finest cases to be considered. Further optimization efforts are required to alleviate these costs.

An important aspect to note is that the multicomponent Chapman-Enskog transport systems, which are solved with the LDL$^{\mathrm{T}}$ method in this study might be *too accurate* for the simple test cases considered for this validation study. Considering the fact that most reference results have relied on simplified mixture rules and relations to match the experimental measurements, the reader might be tempted to believe that the current level of accuracy is redundant. However, observe that the impact of this higher accuracy compared to the standalone INCA results have been clearly demonstrated in the first and second campaigns. Indeed, these cases could have been solved with a simplified mixture rule of Gupta and Yos or of Wilke's as discussed in Section 2.3.2. These models are available within Mutation^{++} and they are still of higher fidelity compared to the models in standalone INCA. They could have been used for the simple validation problems in this study for a less resource intensive approach. These simplified models become inadequate for more involved cases considering additional species due to ionization, ablation, and pyrolysis. Then, in addition to the LDL$^{\mathrm{T}}$ method, Conjugate-Gradient method could also be considered as another efficient option available in Mutation^{++}. Hence, it is important to try and assess how challenging a given problem is before selecting the physicochemical models to use. The coupling in this project enables such a selection. Since this study concerned itself with identifying the

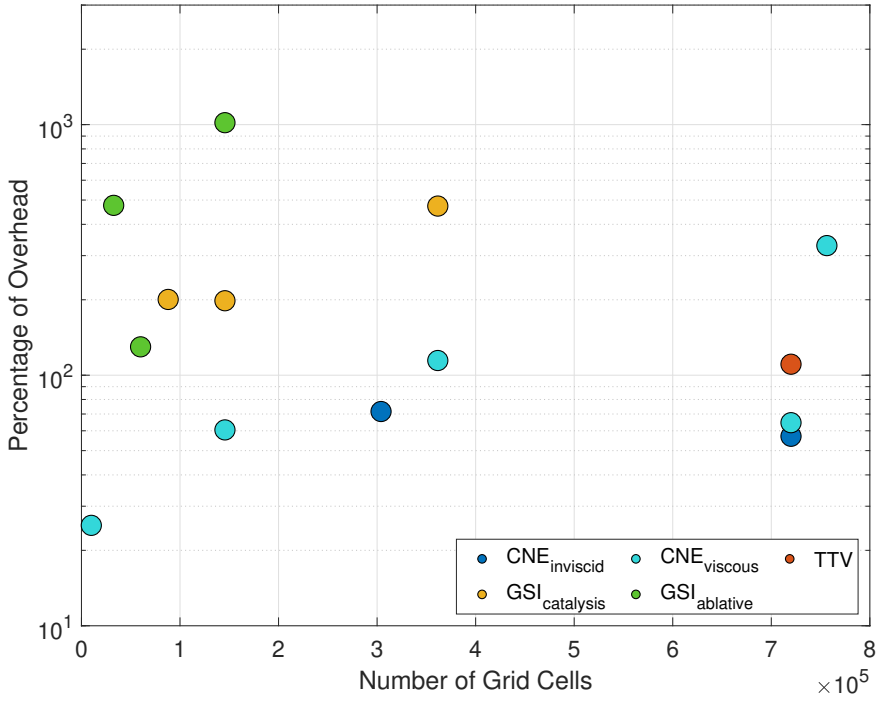

Figure 4.28: Comparison of processor time overhead based on the reference standalone values.

limiting circumstances in terms of accuracy and computational cost, the most demanding options were selected.

To recapitulate, considering the calls from the main solver to a separate library and the calculation of additional rigorous systems of equations, the computational overhead values are indeed rational. These new implementations have often enabled the solver to perform simulations, which it was not capable of in its standalone form. Based on the success of the previous campaigns, the cost is deemed acceptable under the projection that future developments regarding the implementations will continue optimizing the overall computational architecture.

5

Conclusions and Perspectives

This thesis considered the development of a novel aerothermodynamic flow analysis tool for better thermal protection system design, by coupling the high-fidelity flow solver, INCA with an accurate aerothermodynamic library, Mutation^{++}. The governing equations, outstanding features and implementation strategies of thermodynamics, transport properties, chemical kinetics, and gas-surface interactions modules included in the coupling have been discussed in the preceding chapters. To recapitulate per implementation:

- Thermodynamics module extended the combustion-oriented database of INCA to conditions relevant for atmospheric entry applications. Incorporation of the RRHO database enabled a continuous representation with analytical expressions of species properties for internal energy modes.
- Transport properties are rigorously calculated from multicomponent Chapman-Enskog formulations, instead of resorting to simplified mixture rules. A comprehensive collisional database is utilized as opposed to approximate methods.
- Chemical kinetics module provided finite-rate reactions and supplied the analytical Jacobian of the species production rates, instead of internally generating it with finite differences, for the solution of the chemical source term.
- Thermal nonequilibrium with Park's two-temperature model is implemented to simultaneously solve two energy conservation equations for the translational-rotational and vibrational-electronic thermal baths.
- Gas-surface interactions module added a brand new capability to INCA's arsenal by allowing the consideration of surface reactions and mass blowing through a dedicated immersed boundary condition.

Furthermore, since Mutation^{++} is independently available, updates to the model parameters and database values are carried out seamlessly, and collaboration with other users of the library enables directly assessing the capabilities of the flow solver by eliminating the differences in physicochemical models. These implementations are made compatible with the flow solver, which utilizes the Cartesian grid immersed boundary approach, capable of handling complex geometries and employing adaptive grid generation. An immersed interface method hosting catalytic and ablative boundary conditions is uniquely realized within this development.

Three major campaigns have been selected for the verification and validation of each of these implementations. First campaign focused on the general flow field predictions under thermal nonequilibrium. Second campaign aimed at accurately predicting the surface heat fluxes and the influence of catalysis. The third campaign considered an ablative surface boundary condition and investigated the capabilities of the current framework in predicting mass blowing due to ablation. In addition to the different physicochemical flow models, inviscid and viscous cases, low to moderately high Mach number, pressure, freestream temperature and wall temperature ranges are studied. All three campaigns have shown

excellent agreement with reference results from literature, which are selected from a wide array of well-established state-of-the-art aerothermodynamic CFD codes and experiments. These test cases have demonstrated the performance of INCA with the Mutation^{++} implementations. General outcomes with reference results included comparisons of flow field contours, stagnation line temperature and mass fraction distributions, and surface pressure, heat flux, and mass blowing rate profiles. Observations included the impact of thermal nonequilibrium on the flow field features, the influence of accurate transport properties and surface catalysis on wall heat fluxes, and the effect of surface temperature on mass blowing and ablation.

Based on the agreement of the current results with literature and the computational cost of achieving such accuracy, the research questions proposed in Section 1.4 can now be answered. For the first question regarding the accuracy of the simulations, it was seen that the standalone solver was providing inaccurate results presumably due to its approximate collisional data and simplified mixture rules, which neglect the multicomponent interactions between species. Most significantly, it was seen that the standalone solver estimated a thinner boundary layer and the corresponding surface heat flux values were considerably underpredicted with differences as large as 60% at the stagnation point. The newly developed distribution brought this agreement with the reference values to as low as 1.4%, with the addition of specialized physicochemical models and the catalytic wall boundary condition. It was observed that even though the surface resolution was not entirely adequate for accurately estimating the conductive heat flux, the diffusive heat flux component had a dominating impact on the results. In addition to these differences, standalone INCA solver lacked the necessary means to accurately describe the high temperature flow field, namely thermal nonequilibrium and gas-surface interactions. Even though good agreement was obtained in a strictly aerodynamic sense based on the pressure distribution around the object, the differences in the surface heat fluxes or the negligence of surface blowing were sources of significant discrepancies. Since these surface quantities are crucial in estimating the survival of an object during atmospheric entry, the standalone solver is deemed unsuitable for accurately predicting these flow regimes. On the other hand, considering the second part of the first research question, the accuracy of the solver is improved significantly with the current developments. Unlike many well-established codes in the aerothermodynamics community, the current solver was not build from the ground up for these flight regimes. Nevertheless, all test campaigns have shown results on a par with these credible codes. Hence, to conclude the answer for the first research question, the general-purpose INCA flow solver is now able to accurately predict atmospheric entry environments through the coupling with the Mutation^{++} implementations.

As for the second question, regarding the computational cost associated with these implementations, various test cases have been investigated. A notable drawback identified in this study was the increase in the number of grid cells to reach the required surface resolution. This stemmed from the inherent difficulty of Cartesian grids in resolving the surface geometry. Although, the general flow features and pressure distributions are predicted very well even with a coarser grid, finer grids are needed for estimating the surface heat flux correctly. Future developments should focus on a more optimized wall treatment. Theoretically, the external calls to the library, the solution of multicomponent transport systems instead of simplified mixture rules, calculation of an additional conservation equation for vibrational energy, and the evaluation of surface reactions entail significantly more processing time. The computational overhead with respect to the standalone solver without the implementations were reported for a number of cases with different flow models. It was seen that for a chemical nonequilibrium solution, the computational overhead is approximately 60%. Values around this range are regarded as acceptable considering the significant improvement remarked in the results. Bear in mind that more efficient models, which are still of higher fidelity than those of the standalone solver could also be selected within Mutation^{++}. As more involved physicochemical models are included, the cost naturally becomes higher. Addition of thermal nonequilibrium increases the amount of overhead to around 110%. For a catalytic or ablative surface this goes up to 198% and 1018%, respectively. The significant increase in computational cost is anticipated, especially with gas-surface interactions due to the way the boundary condition had to be implemented in the immersed interface method, necessitating calls for not only ghost-cells, but additionally for the interface fluxes. A more optimized method to avoid these separate calls to the library might be devised by reusing some information in both instances. A more efficient processor load balancing could also avoid limiting the surrounding fluid cells with the cut-cell solutions. Nevertheless, one of the most important aspects to take into account in this assessment is the novelty of these additions. A potential perspective should compare the current development operating

on a complex geometry, which would either be highly costly or even improbable with a body-conformal approach. Hence, regarding the second research question, it is concluded that the computational cost is justified for the gain in accuracy, although further optimization is required for more efficient usage.

This thesis established an extensible framework, where future development regarding aerothermodynamic flow analysis can be performed. The main contribution of this project is that it has enabled the analysis of a vast selection of scientific and engineering problems in a unique platform, which provides state-of-the-art numerical fidelity and physicochemical modeling within a Cartesian grid immersed interface approach. Investigating the influence of shape change is seen as the immediate next step for this development, as now a sufficient level of confidence in the solver's current implementations are established with this study. Having these capabilities under a single tool most notably allows for the time-accurate simulation of a complex geometry undergoing ablation induced recession. This problem definition describes the most aerothermodynamicly crucial stage of the atmospheric entry trajectory of a spacecraft, a meteor or a satellite's demise at the end of its life-cycle. High-fidelity simulations, LES and DNS, can be performed to study turbulence in these flow environments. Influence of transport models, ablation, and blowing on flow stability and the onset of turbulent flow can be investigated. This work could also be extended by introducing material response inside the solid domain to benefit from the immersed interface approach. Other possible extensions of this thesis work include the investigation of ionized mixtures, effect of radiation, detailed analysis of thermochemical nonequilibrium for surface reactions, and impact of shock wave-boundary layer interactions on ablation. Ultimately, the aerothermodynamic flow solver developed in this thesis has performed exceptionally well under the conditions investigated within this study, and it holds great potential for becoming an invaluable tool in future efforts on developing a better understanding of atmospheric entry phenomena.

A

Developer's Guide

This appendix provides details on the modifications made within the INCA solver during the coupling with the Mutation^{++} library. The general coding conventions and structure of INCA is preserved for efficiency, consistency and readability. The changes are divided into two categories: coupling interface developments and main solver implementations. Generally, the interface links the external library to the main solver by providing the new subroutines to be called instead of the standalone distribution. As a convention, functions called from Mutation^{++} begin with the tag "`mpp_`", subroutines which contain these in the interface include "`MUTATIONPP_`", and main INCA modules start with "`inca_`". Inside the code, all baseline implementations are marked with 'Mutation++ implementation' comment, all thermal nonequilibrium implementations are marked with a "TTV implementation" comment, and all gas-surface interactions implementations are marked with a "GSI implementation" comment.

A.1. Coupling Interface

All the interface subroutines are stored in the file `lib_mutationpp_interface.f`. This interface uses the `mutationpp` module to call for the functions in the Mutation^{++} Fortran wrapper. These functions are called within their respective subroutines in the interface, which are mostly created according to the main pillars of the coupling: thermodynamics, transport properties, chemical kinetics, thermal nonequilibrium and gas-surface interactions. The 12 subroutines that form this interface are explained in this section. Although the internal structures of these subroutines may vary depending on the main code, their purposes should be analogous between other coupling interfaces for Mutation^{++}. Hence, this section also aims to provide a preliminary overview for researchers to benefit from, while embarking on a similar task of coupling Mutation^{++} with another flow solver.

`MUTATIONPP_INITIALIZE`

Mutation^{++} is initialized through `mpp_initialize` with the `MPP_MIXNAME` and `MPP_STATE_MODEL` variables specified by the input files to determine the Mutation^{++} mixture file name, and the thermochemical flow model as equilibrium (`Equil`), chemical nonequilibrium (`ChemNonEq1T`), or thermochemical nonequilibrium (`ChemNonEqTTv`). Checks are made to ensure that the inputs are valid, and the number and order of species are consistent between input files of INCA and Mutation^{++}. Basic arrays are allocated and common parameters are defined.

Functions called from Mutation^{++}: `mpp_initialize`, `mpp_nspecies`, `mpp_species_name`, `mpp_species_mw`.

`MUTATIONPP_FINALIZE`

Simply cleans up after the allocated arrays are no longer needed.

`MUTATIONPP_MARCHING`

This is the main subroutine, which loops over all the cells in the given domain. Depending on the given input parameters, different set of subroutines are called. The choice differs for the permutations of a viscous or inviscid; single or two temperature; single or multispecies flow conditions. The subroutines

called for each cell in the most general case are GET_MUTATIONPP_SSCONS, GET_MUTATIONPP_THERMO, and GET_MUTATIONPP_TRANSP. The call to GET_MUTATIONPP_SSCONS is necessary to set the current state before requesting any type of information from the other physicochemistry functions of Mutation^{++}. For efficiency, instead of calling it twice within GET_MUTATIONPP_THERMO and GET_MUTATIONPP_TRANSP, the call is made only once for a single loop over a cell.

GET_MUTATIONPP_SSCONS

Provides the information of the thermochemical state of the current mixture of interest to the Mutation^{++} library, using conservative variables. The state of the mixture is set with mpp_set_state by providing the appropriate state vector. For almost all of the interface subroutines, this state vector dictates the necessary inputs. This state vector varies depending on the state model selected in the input file:

- For equilibrium (Equil):
  - Case 0: Conserved variables (mixture density, static energy density)
  - Case 1: Primitive set 1 (pressure, temperature)
  - Case 2: Primitive set 2 (elemental mole fractions, [pressure, temperature] array)
- For chemical nonequilibrium (ChemNonEq1T):
  - Case 0: Conserved variables (species densities, total energy density)
  - Case 1: Primitive set 1 (species densities, mixture temperature)
  - Case 2: Primitive set 2 (species mass fractions, [pressure, temperature] array)
- For thermochemical nonequilibrium (ChemNonEqTTv):
  - Case 0: Conserved variables (species densities, [total energy density, vibrational energy density] array)
  - Case 1: Primitive variables (species densities and [translational temperature, vibrational temperature] array)

Type "0" is selected within this subroutine to solve an energy equation for determining the mixture temperature. Accordingly, species densities and the kinetic energy is computed to yield the specific internal energy for a given mixture. Note that in case of thermal nonequilibrium, the conserved vibrational energy corresponds to the internal energy, and does not include kinetic energy. Once the state of the mixture is communicated to the library, a state_check flag is enabled, which is checked whenever another subroutine requests the information of a state. This check helps to avoid using erroneous state information between calls.

Functions called from Mutation^{++}: mpp_set_state.

GET_MUTATIONPP_SSPRIM

Also provides the information of the thermochemical state of the current mixture of interest to the Mutation^{++} library, but with primitive variables. Similar to GET_MUTATIONPP_SSCONS, mpp_set_state is invoked, this time with the type "2" option. Unlike GET_MUTATIONPP_SSCONS, this subroutine directly prescribes the state according to the given parameters. Consequently, it is called to impose the initial and boundary conditions in the main solver for the known primitive variables. Optionally, mixture density, specific energy, ratio of specific heats, specific heats at constant pressure, and specific vibrational energy could be outputted.

Functions called from Mutation^{++}: mpp_convert_ys_to_ye, mpp_convert_ye_to_xe, mpp_set_state, mpp_density, mpp_mixture_e_mass, mpp_mixture_frozen_gamma, mpp_mixture_frozen_cp_mass, mpp_species_e_mass.

GET_MUTATIONPP_THERMO

Once the state of the mixture is set, thermodynamic properties of species and mixtures are called: namely, species specific heats, species total and vibrational enthalpies, mixture specific heats, mixture translational and vibrational temperatures, mixture pressure, and mixture speed of sound. The equations for these variables were provided in Section 2.2.

Functions called from Mutation^{++}: mpp_species_cp_mass, mpp_species_h_mass, mpp_mixture_frozen_cp_mass, mpp_get_temperatures.

GET_MUTATIONPP_TRANSP
For viscous flows, computes the average diffusion coefficient per species, mixture viscosity and mixture translational and vibrational thermal conductivity, according to the current state. All or some of these variables could be requested depending on the input specification. The mathematical expressions for these variables were provided in Section 2.3.

Functions called from Mutation^{++}: `mpp_average_diffusion_coeffs`, `mpp_viscosity`, `mpp_frozen_thermal_conductivity`.

GET_MUTATIONPP_CHPROD
Computes the chemical production rates of species. Also requires setting the state according to the given primitive inputs for the type "1" option of `mpp_set_state`. Ensures that the resultant mass fractions sum to one. The equations for these variables were provided in Section 2.4.

Functions called from Mutation^{++}: `mpp_set_state`, `mpp_net_production_rates`.

GET_MUTATIONPP_CHJACO
Computes production rate Jacobians with respect to species densities, as in Eq. (2.69).

Functions called from Mutation^{++}: `mpp_species_jacobian_rho`.

GET_MUTATIONPP_TTVSRC
Computes the total energy transfer source term due to the exchange between the translational-rotational and vibrational-electronic modes as in Eq. (2.72), and due to chemical reactions for thermal nonequilibrium as in Eq. (2.73). Requires setting the state according to the given primitive inputs for the type "1" option of `mpp_set_state`.

Functions called from Mutation^{++}: `mpp_set_state`, `mpp_source_energy_transfer`.

GET_MUTATIONPP_GSIISO
Calculates the surface mass balance for imposing the isothermal gas-surface interaction boundary condition. As discussed in Section 3.4.2, species mole fractions at an image point are provided to describe the diffusion model. Surface state is defined by these concentrations and the prescribed wall temperature. Surface mass balance is solved and new wall state is found. Surface production rate of each species is calculated depending on the surface models specified in the GSI input file. Mass blowing velocity is calculated according to Eq. (2.83).

Functions called from Mutation^{++}: `mpp_convert_rho_to_x`, `mpp_set_diffusion_model`, `mpp_set_surface_state`, `mpp_solve_surface_balance`, `mpp_get_surface_state`, `mpp_surface_production_rates`.

GET_MUTATIONPP_GSIENB
Same as `GET_MUTATIONPP_GSIISO` with the addition of the conductive heat flux model for the energy balance calculation.

Functions called from Mutation^{++}: `mpp_convert_rho_to_x`, `mpp_set_diffusion_model`, `mpp_set_cond_heat_flux`, `mpp_set_surface_state`, `mpp_solve_surface_balance`, `mpp_get_surface_state`, `mpp_surface_production_rates`.

A.2. Main Code Implementations

Implementations to the INCA code are listed here to aid in future optimization efforts to keep track of all the changes. File names are given instead of separate subroutines, and related implementations are grouped for the sake of brevity.

inca_boundaries.f
Imposes the regular boundary conditions at the edges of the domain. Density and internal energy for the boundary state is called from the interface. Vibrational temperature and energy are also defined, when requested.

Functions called from the library interface: `GET_MUTATIONPP_SSPRIM`.

inca_comp_visc_flux_2.f, inca_rhs_comp.f
Alternative subroutines to calculate the viscous flux are introduced, which include the vibrational heat flux in Eq. (2.71) for the total and vibrational energy conservation equations.

`inca_fsi.f`
This module deals with the immersed boundary models and the ghost-point boundary conditions. Interface viscosity and thermal conductivity for the available models are supplied by the interface. Ghost-point thermochemical state is solved. Temperature is clamped to half the wall temperature for stability. Vibrational temperature is extrapolated consistently to the ghost point by taking into account this clamped wall temperature, when it occurs. Wall state modification according to gas-surface interactions is included. Blowing velocity and updated species fractions are extrapolated to the ghost-point.

Implemented a new immersed boundary subroutine called `GSI_INTERFACE_MODEL` for the method developed in Section 3.4.2. Surface reactions are computed through the library interface. Although not used in the current study, interface recession speed according to Eq. (2.84) is computed through a solid density input. A zero solid density assumes a fixed interface and it is the default behavior. These contributions are used to construct the interface exchange terms.

Instead of an isothermal wall temperature, a simple surface temperature distribution is implemented to assign the wall temperature at different angles along the surface.

Functions called from the library interface: `GET_MUTATIONPP_SSPRIM`, `GET_MUTATIONPP_TRANSP`, `GET_MUTATIONPP_THERMO`, `GET_MUTATIONPP_GSIISO`, `GET_MUTATIONPP_GSIENB`.

`inca_grids.f`, `inca_ib.f`, `inca_init.f`, `inca_namelists.f`, `inca_parameters.f`, `inca_varnames.f`
Required variables and parameters for Mutation^{++} inputs, thermal nonequilibrium and gas-surface interactions implementations are defined.

`inca_incon.f`, `inca_inflow.f`
Mixture states based on the initial conditions and prescribed freestream conditions are computed. Modifications for thermal nonequilibrium are taken into account.

Functions called from the library interface: `GET_MUTATIONPP_SSPRIM`.

`inca_marching_rk.f`
Includes the main call to solve for the conserved quantities over the domain. Also includes the conditional statement to select the immersed interface model to be employed.

Functions called from the library interface: `MUTATIONPP_MARCHING`.

`inca_material.f`
This module hosts the physicochemical models for the standalone INCA. None of the subroutines here are called when Mutation^{++} is operational. The only modification here is the addition of Wilke's mixing rule for viscosity. It was not used in this study, but it could be selected for other less severe applications with the standalone distribution.

`inca_marching.f`, `inca_ordnung.f`, `inca_tecplot_bin.f`
Added a post-processing subroutine called `TECPLOT_QW` for outputting immersed interface surface properties at the end of a simulation. Initially build to extract conductive and diffusive heat fluxes, pressures, blowing velocities, and mass blowing rates at the immersed interface. Provides instantaneous values for each cut-element and cut-cell along the surface.

`inca_reaction.f`, `inca_sourceterms.f`, `lib_dvode.f90`
Reaction rates are calculated through a separate subroutine called `REACT_RATE_ARR_MPP`. This subroutine calls the DVODE solver to solve the ODE for the chemical source term, as explained in Section 3.2. DVODE options are adjusted to allow for the mass production rates and their analytical Jacobians with respect to species densities to be provided by Mutation^{++}. Vibrational temperature input is implemented in the DVODE interface. Calculated source terms are added to the conservative species fractions and energy variables.

Functions called from the library interface: `GET_MUTATIONPP_CHPROD`, `GET_MUTATIONPP_CHJACO`, `GET_MUTATIONPP_TTVSRC`.

`inca_readwrite.f`, `inca_output.f`
Necessary changes are made to enable writing the thermal nonequilibrium results and also to enable restarting from an initial solution.

A.3. INCA Algorithm

Radically simplified algorithm of the INCA solver highlighting the major physicochemical calls to the Mutation^{++} interface is given below.

Algorithm 1: INCA flow solver

Run simulation

assign blocks and setup partitioning

initialize domain, edge boundary conditions, immersed boundaries

while *stopping criteria not reached* **do**

  compute timestep

  while *last Runge-Kutta step not reached* **do**

    compute interface exchange terms (with `GET_MUTATIONPP_SSPRIM`, `GET_MUTATIONPP_TRANSP`, `GET_MUTATIONPP_GSIISO`, `GET_MUTATIONPP_GSIENB`)

    compute physical fluxes, add exchange terms

    compute RHS of Navier-Stokes

    advance solution in time

    repeat *for 2 Strang steps*

      update thermodynamics and transport (with `MUTATIONPP_MARCHING`)

      calculate reaction rates (with `GET_MUTATIONPP_CHPROD`, `GET_MUTATIONPP_CHJACO`, `GET_MUTATIONPP_TTVSRC`)

    end

    set boundary conditions and extend to ghost-points (with `GET_MUTATIONPP_SSPRIM`)

  end

  output results and statistics

end

B

Mixtures and Mechanisms

The mixtures and the reaction mechanisms used for the simulations in Chapter 4 are given in this appendix. For the first and second campaigns in Section 4.1 and Section 4.2, the 5-species air model include

$$N_2,\ O_2,\ NO,\ N,\ O\,.$$

For the third campaign, the addition of ablation products increased the number of species to 11 with

$$\ldots\ CO_2,\ CO,\ CN,\ C_3,\ C_2,\ C\,.$$

As explained in Section 2.4, each reaction r is governed by a forward reaction rate coefficient, which is calculated according to a modified Arrhenius rate law expression repeated here as

$$k_{f,r} = A_r T^{\beta_r} \exp\left(-\frac{(E_a)_r}{\mathcal{R}T}\right)\,. \tag{2.67}$$

This could be rewritten in a more common way by defining $\theta_r = (E_a)_r/\mathcal{R}$, to obtain

$$k_{f,r} = A_r T^{\beta_r} \exp\left(-\frac{\theta_r}{T}\right)\,. \tag{B.1}$$

The coefficients in this equation are assigned to each reaction being considered. For the reactions considered in this thesis, they are given in Table B.1 and Table B.2. Consistent with the reference simulations, for the first campaign these mechanisms are taken from Park's work in 1993 [101], and for the second campaign they are taken from Park's work in 2001 [104]. For the third campaign, mechanisms with carbon are retrieved from the work of Olynick [94]. For the dissociation reactions, the associated temperature for the forward reaction rate coefficient is taken to be the geometric average temperature $\sqrt{T^{\mathrm{T}}T^{\mathrm{V}}}$. These correspond to reactions 1-6 in Table B.1 and 1-13 in Table B.2. The remaining reactions are termed exchange reactions, and they consider the translational temperature. Note that the backward reaction rate is found by $k_{b,r} = k_{f,r}/K_{eq,r}$ as in Eq. (2.65) through the equilibrium constant $K_{eq,r}$. For this calculation, the associated temperature is selected to be the translational temperature as well.

Table B.1: Reaction mechanisms for the first and second campaigns in Section 4.1 and Section 4.2. First campaign uses reactions 7 and 8, while the second campaign uses reactions 9 and 10.

#	Reaction	A	β	θ	From
1	$N_2 + M \rightleftharpoons N + N + M$	7.0×10^{21}	-1.6	113200	[104]
2	$N_2 + M \rightleftharpoons N + N + M$	3.0×10^{22}	-1.6	113200	[104]
	M: N, O				
3	$O_2 + M \rightleftharpoons O + O + M$	2.0×10^{21}	-1.5	59360	[104]
4	$N_2 + M \rightleftharpoons N + N + M$	1.0×10^{22}	-1.5	59360	[104]
	M: N, O				
5	$NO + M \rightleftharpoons N + O + M$	5.0×10^{15}	0.0	75500	[101]
6	$NO + M \rightleftharpoons N + O + M$	1.1×10^{17}	0.0	75500	[101]
	M: NO, N, O				
7	$N_2 + O \rightleftharpoons NO + N$	6.4×10^{13}	-1.0	38400	[101]
8	$NO + O \rightleftharpoons O_2 + N$	8.4×10^{9}	1.0	19450	[101]
9	$N_2 + O \rightleftharpoons NO + N$	5.7×10^{12}	0.42	42938	[104]
10	$NO + O \rightleftharpoons O_2 + N$	8.4×10^{12}	0.0	19400	[104]

Table B.2: Reaction mechanisms for the third campaign in Section 4.3.

#	Reaction	A	β	θ	From
1	$N_2 + M \rightleftharpoons N + N + M$	7.0×10^{21}	-1.6	113200	[94]
2	$N_2 + M \rightleftharpoons N + N + M$	3.0×10^{22}	-1.6	113200	[94]
	M: C, N, O				
3	$O_2 + M \rightleftharpoons O + O + M$	2.0×10^{21}	-1.5	59750	[94]
4	$O_2 + M \rightleftharpoons O + O + M$	1.0×10^{22}	-1.5	59750	[94]
	M: C, N, O				
5	$C_2 + M \rightleftharpoons C + C + M$	3.7×10^{14}	0.0	69000	[94]
6	$CN + M \rightleftharpoons C + N + M$	2.5×10^{14}	0.0	71000	[94]
7	$NO + M \rightleftharpoons N + O + M$	5.0×10^{15}	0.0	75500	[94]
8	$NO + M \rightleftharpoons N + O + M$	1.1×10^{17}	0.0	75500	[94]
	M: C, N, O				
9	$CO_2 + M \rightleftharpoons CO + O + M$	6.9×10^{21}	-1.5	63275	[94]
10	$CO_2 + M \rightleftharpoons CO + O + M$	1.4×10^{22}	-1.5	63275	[94]
	M: C, N, O				
11	$CO + M \rightleftharpoons C + O + M$	2.3×10^{20}	-1.0	129000	[94]
12	$CO + M \rightleftharpoons C + O + M$	3.4×10^{20}	-1.0	129000	[94]
	M: C, N, O				
13	$C_3 + M \rightleftharpoons C_2 + C + M$	6.3×10^{16}	-0.5	101200	[94]
14	$N_2 + O \rightleftharpoons NO + N$	6.4×10^{17}	-1.0	38370	[94]
15	$NO + O \rightleftharpoons N + O_2$	8.4×10^{12}	0.0	19450	[94]
16	$CO + C \rightleftharpoons C_2 + O$	6.3×10^{17}	-1.0	58000	[94]
17	$CO + O \rightleftharpoons O_2 + C$	3.9×10^{13}	-0.18	69200	[94]
18	$CO + N \rightleftharpoons CN + O$	1.0×10^{14}	0.0	38600	[94]
19	$N_2 + C \rightleftharpoons CN + N$	1.1×10^{14}	-0.11	23200	[94]
20	$CN + O \rightleftharpoons NO + C$	1.6×10^{13}	0.1	14600	[94]
21	$CN + C \rightleftharpoons C_2 + N$	5.0×10^{13}	0.0	13000	[94]
22	$CO_2 + O \rightleftharpoons O_2 + CO$	2.1×10^{13}	0.0	27800	[94]

Bibliography

[1] Hicham Alkandry, Iain Boyd, and Alexandre Martin. Comparison of models for mixture transport properties for numerical simulations of ablative heat-shields. In *51st AIAA Aerospace Sciences Meeting including the New Horizons Forum and Aerospace Exposition*, page 303, 2013. 21, 22, 23

[2] Hicham Alkandry, Iain D Boyd, and Alexandre Martin. Coupled flow field simulations of charring ablators with nonequilibrium surface chemistry. In *44th AIAA Thermophysics Conference*, page 2634, 2013. 5, 8, 29, 30

[3] John D. Anderson Jr. *Hypersonic and high-temperature gas dynamics*. American Institute of Aeronautics and Astronautics, 2006. 1, 3, 13, 17, 25, 33

[4] Paolo Francesco Barbante. *Accurate and efficient modelling of high temperature nonequilibrium air flows*. Von Karman Institute for Fluid Dynamics, 2001. 16, 28

[5] Georgios Bellas-Chatzigeorgis. *Development of advanced gas-surface interaction models for chemically reacting flows for re-entry conditions*. PhD thesis, 2018. 29, 64

[6] Georgios Bellas-Chatzigeorgis, PAOLO FRANCESCO Barbante, TE Magin, et al. Development of detailed chemistry models for boundary layer catalytic recombination. In *8th European Symposium on Aerothermodynamics for Space Vehicle*, pages 1–8, 2015. 28, 30

[7] Georgios Bellas Chatzigeorgis, Alessandro Turchi, Alan Viladegut, Olivier Chazot, Paolo Francesco Barbante, and Thierry Magin. Development of catalytic and ablative gas-surface interaction models for the simulation of reacting gas mixtures. In *23rd AIAA Computational Fluid Dynamics Conference*, page 4499, 2017. 11, 28, 30

[8] Georgios Bellas-Chatzigeorgis, Paolo F Barbante, and Thierry E Magin. Energy accommodation coefficient calculation methodology using state-to-state catalysis applied to hypersonic flows. *AIAA Journal*, 58(1):278–290, 2020. 30

[9] John J Bertin and Russell M Cummings. Critical hypersonic aerothermodynamic phenomena. *Annu. Rev. Fluid Mech.*, 38:129–157, 2006. 7, 10

[10] Daniele Bianchi. *Modeling of ablation phenomena in space applications*. PhD thesis, 2008. 30

[11] Daniele Bianchi, Francesco Nasuti, and Emanuele Martelli. Coupled analysis of flow and surface ablation in carbon-carbon rocket nozzles. *Journal of Spacecraft and Rockets*, 46(3):492–500, 2009. 30

[12] Frederick Gwynn Blottner, Margaret Johnson, and Molly Ellis. Chemically reacting viscous flow program for multi-component gas mixtures. Technical report, Sandia Labs., Albuquerque, N. Mex., 1971. 23, 54, 63

[13] Deepak Bose, Michael Olson, Bernard Laub, Todd White, Jay Feldman, Jose Santos, Milad Mahzari, Matthew MacLean, Aaron Dufrene, and Michael Holden. Initial assessment of Mars science laboratory heatshield instrumentation and flight data. In *51st AIAA Aerospace Sciences Meeting including the New Horizons Forum and Aerospace Exposition*, page 908, 2013. xiii, 6, 7

[14] Joseph M Brock, Pramod K Subbareddy, and Graham V Candler. Detached-eddy simulations of hypersonic capsule wake flow. *AIAA Journal*, 53(1):70–80, 2015. 10

[15] Peter N Brown, George D Byrne, and Alan C Hindmarsh. Vode: A variable-coefficient ode solver. *SIAM journal on scientific and statistical computing*, 10(5):1038–1051, 1989. 34

[16] Olivier Cabrit and Franck Nicoud. Direct numerical simulation of a reacting turbulent channel flow with thermochemical ablation. *Journal of Turbulence*, (11):N44, 2010. 9, 30

[17] Graham Candler. Nonequilibrium processes in hypervelocity flows: an analysis of carbon ablation models. In *50th AIAA Aerospace Sciences Meeting including the New Horizons Forum and Aerospace Exposition*, page 724, 2012. 21, 29

[18] Graham V Candler. Rate effects in hypersonic flows. *Annual Review of Fluid Mechanics*, 51: 379–402, 2019. 3, 6

[19] Graham V Candler, Heath B Johnson, Ioannis Nompelis, Vladimyr M Gidzak, Pramod K Subbareddy, and Michael Barnhardt. Development of the US3D code for advanced compressible and reacting flow simulations. In *53rd AIAA Aerospace Sciences Meeting*, page 1893, 2015. 8

[20] Graham V Candler, Pramod K Subbareddy, and Joseph M Brock. Advances in computational fluid dynamics methods for hypersonic flows. *Journal of Spacecraft and Rockets*, 52(1):17–28, 2015. 7, 8

[21] Graham V Candler, Christopher R Alba, and Robert B Greendyke. Characterization of carbon ablation models including effects of gas-phase chemical kinetics. *Journal of Thermophysics and Heat Transfer*, 31(3):512–526, 2017. 8, 29

[22] Valerio Carandente, Gennaro Zuppardi, and Raffaele Savino. Aerothermodynamic and stability analyses of a deployable re-entry capsule. *Acta Astronautica*, 93:291–303, 2014. 2

[23] Y-K Chen and Frank S Milos. Ablation and thermal response program for spacecraft heatshield analysis. *Journal of Spacecraft and Rockets*, 36(3):475–483, 1999. 28

[24] Yih-Kanq Chen and Frank Milos. Finite-rate ablation boundary conditions for a carbon-phenolic heat-shield. In *37th AIAA Thermophysics Conference*, page 2270, 2004. 29

[25] Yih-Kanq Chen and Frank S Milos. Navier-Stokes solutions with finite rate ablation for planetary mission earth reentries. *Journal of Spacecraft and Rockets*, 42(6):961–970, 2005. 21, 29, 30, 44, 63

[26] Yih-Kanq Chen and Frank S Milos. Multidimensional finite volume fully implicit ablation and thermal response code. *Journal of Spacecraft and Rockets*, 55(4):914–927, 2018. 29

[27] Yoann Cheny and Olivier Botella. The ls-stag method: A new immersed boundary/level-set method for the computation of incompressible viscous flows in complex moving geometries with good conservation properties. *Journal of Computational Physics*, 229(4):1043–1076, 2010. 35

[28] Ting Horng Chung, Mohammad Ajlan, Lloyd L Lee, and Kenneth E Starling. Generalized multiparameter correlation for nonpolar and polar fluid transport properties. *Industrial & engineering chemistry research*, 27(4):671–679, 1988. 24

[29] Donald Keith Clarke, HA Hassan, and MD Salas. Euler calculations for multi-element airfoils using Cartesian grids. *AIAA journal*, 24(3):353–358, 1986. 35

[30] Phillip Colella, Daniel T Graves, Benjamin J Keen, and David Modiano. A Cartesian grid embedded boundary method for hyperbolic conservation laws. *Journal of Computational Physics*, 51(LBNL-56420), 2004. 36

[31] Ryan Campbell Crocker. *Direct Numerical Simulation Of Ablative Boundaries In Turbulent And Laminar Flows*. PhD thesis, 2015. 9

[32] Carol Davies and Marla Arcadi. Planetary mission entry vehicles quick reference guide. version 3.0. 2006. xiii, 4

[33] Joseph Del Corso, F Cheatwood, Walter Bruce, Stephen Hughes, and Anthony Calomino. Advanced high-temperature flexible TPS for inflatable aerodynamic decelerators. In *21st AIAA Aerodynamic Decelerator Systems Technology Conference and Seminar*, page 2510, 2011. 2

[34] Felix Diegelmann, Stefan Hickel, and Nikolaus A Adams. Three-dimensional reacting shock–bubble interaction. *Combustion and Flame*, 181:300–314, 2017. 34

[35] Yves Dubief, Juergen Uhl, and Ryan Crocker. Direct numerical simulation of ablation from an internally heated turbulent flow. In *19th AIAA Computational Fluid Dynamics*, page 4149. 2009. 9

[36] Georges Duffa. *Ablative thermal protection systems modeling*. American Institute of Aeronautics and Astronautics, Inc., 2013. 1, 6

[37] Michael G Dunn and S Kang. Theoretical and experimental studies of reentry plasmas. 1973. 54

[38] Sebastian Eberhardt. *Large-eddy simulations of supersonic mixing with application to scramjets*. PhD thesis, Technische Universität München, 2017. 21

[39] Karl T Edquist, Brian R Hollis, Christopher O Johnston, Deepak Bose, Todd R White, and Milad Mahzari. Mars science laboratory heat shield aerothermodynamics: Design and reconstruction. *Journal of Spacecraft and Rockets*, 51(4):1106–1124, 2014. xiii, 4

[40] Alexandre Ern and Vincent Giovangigli. Fast and accurate multicomponent transport property evaluation. *Journal of Computational Physics*, 120(1):105–116, 1995. 23

[41] Francesca Ferri, Özgür Karatekin, Stephen R Lewis, François Forget, Alessio Aboudan, Giacomo Colombatti, Carlo Bettanini, Stefano Debei, Bart Van Hove, Veronique Dehant, et al. ExoMars atmospheric Mars entry and landing investigations and analysis (AMELIA). *Space Science Reviews*, 215(1):8, 2019. 2

[42] JP Fleurial, T Caillat, BJ Nesmith, RC Ewell, DF Woerner, GC Carr, and LE JonesJet. Thermoelectrics: from space power systems to terrestrial waste heat recovery applications. In *2nd Thermoelectrics Applications Workshop*, 2011. xiii, 4

[43] Keisuke Fujii and Hans G Hornung. A procedure to estimate absorption rate of sound propagating through high temperature gas. 2001. 6

[44] Jesse A Fulton, Jack R Edwards, Hassan A Hassan, James C McDaniel, Christopher P Goyne, Robert D Rockwell, Andrew D Cutler, Craig T Johansen, and Paul M Danehy. Large-eddy/Reynolds-averaged Navier-Stokes simulations of reactive flow in dual-mode scramjet combustor. *Journal of Propulsion and Power*, 30(3):558–575, 2014. 10

[45] Harold W Gehman Jr, John L Barry, Duane W Deal, James N Hallock, Kenneth W Hess, G Scott Hubbard, John M Logsdon, Douglas D Osheroff, Sally K Ride, and Roger E Tetrault. Columbia accident investigation board report. volume 1. 2003. 7

[46] Peter A Gnoffo. Planetary-entry gas dynamics. *Annual Review of Fluid Mechanics*, 31(1):459–494, 1999. 3

[47] Peter A Gnoffo, K James Weilmuenster, Robert D Braun, and Christopher I Cruz. Influence of sonic-line location on Mars Pathfinder probe aerothermodynamics. *Journal of Spacecraft and Rockets*, 33(2):169–177, 1996. 3

[48] Peter A Gnoffo, K James Weilmuenster, H Harris Hamilton, David R Olynick, and Ethiraj Venkatapathy. Computational aerothermodynamic design issues for hypersonic vehicles. *Journal of Spacecraft and Rockets*, 36(1):21–43, 1999. 10

[49] Sigal Gottlieb and Chi-Wang Shu. Total variation diminishing runge-kutta schemes. *Mathematics of computation*, 67(221):73–85, 1998. 34

[50] R Goulard. On catalytic recombination rates in hypersonic stagnation heat transfer. *Journal of Jet Propulsion*, 28(11):737–745, 1958. 28

[51] G Groskopf, MJ Kloker, KA Stephani, O Marxen, and G Iaccarino. Hypersonic flows with discrete oblique surface roughness and their stability properties. *Proceedings of the 2010 Summer Program*, pages 405–422, 2010. 9

[52] Roop N Gupta, Jerrold M Yos, Richard A Thompson, and Kam-Pui Lee. A review of reaction rates and thermodynamic and transport properties for an 11-species air model for chemical and thermal nonequilibrium calculations to 30000 K. 1990. 23, 63

[53] Bernd Helber, Olivier Chazot, Annick Hubin, and Thierry E Magin. Emission spectroscopic boundary layer investigation during ablative material testing in plasmatron. *JoVE (Journal of Visualized Experiments)*, (112):e53742, 2016. 30

[54] F Herning and L Zipperer. Calculation of the viscosity of technical gas mixtures from the viscosity of the individual gases. *Gas u. Wasserfach*, 79:69, 1936. 23, 24

[55] Joseph O Hirschfelder, Charles F Curtiss, Robert Byron Bird, and Maria Goeppert Mayer. *Molecular theory of gases and liquids*, volume 165. Wiley New York, 1964. 13, 17, 19, 20, 23, 24

[56] Michael E Holloway, Kyle M Hanquist, and Iain D Boyd. Effect of thermochemistry modeling on hypersonic flow over a double cone. In *AIAA Scitech 2019 Forum*, page 2281, 2019. 9

[57] Xiangyu Y Hu, BC Khoo, Nikolaus A Adams, and FL Huang. A conservative interface method for compressible flows. *Journal of Computational Physics*, 219(2):553–578, 2006. 36

[58] Stephen Hughes, F Cheatwood, Robert Dillman, Anthony Calomino, Henry Wright, Joseph DelCorso, and Anthony Calomino. Hypersonic inflatable aerodynamic decelerator (HIAD) technology development overview. In *21st AIAA Aerodynamic Decelerator Systems Technology Conference and Seminar*, page 2524, 2011. 2

[59] Guang-Shan Jiang and Chi-Wang Shu. Efficient implementation of weighted eno schemes. *Journal of computational physics*, 126(1):202–228, 1996. 34

[60] Seongwon Kang, Gianluca Iaccarino, and Parviz Moin. Accurate immersed-boundary reconstructions for viscous flow simulations. *AIAA journal*, 47(7):1750–1760, 2009. 35

[61] RM Kendall, EP Bartlett, RA Rindal, and CB Moyer. An analysis of the coupled chemically reacting boundary layer and charring ablator. part I: Summary report. *NASA CR-1060, June*, 1968. 27, 32

[62] MP Kirkpatrick, SW Armfield, and JH Kent. A representation of curved boundaries for the solution of the Navier-Stokes equations on a staggered three-dimensional Cartesian grid. *Journal of Computational Physics*, 184(1):1–36, 2003. 36

[63] Doyle Knight, José Longo, Dimitris Drikakis, Datta Gaitonde, Andrea Lani, Ioannis Nompelis, Bodo Reimann, and Louis Walpot. Assessment of CFD capability for prediction of hypersonic shock interactions. *Progress in Aerospace Sciences*, 48:8–26, 2012. 44, 54, 60

[64] Carleton P Knisely and Xiaolin Zhong. Supersonic modes in hot-wall hypersonic boundary layers with thermochemical nonequilibrium effects. In *2018 AIAA Aerospace Sciences Meeting*, page 2085, 2018. 6

[65] David W Kuntz, Basil Hassan, and Donald L Potter. Predictions of ablating hypersonic vehicles using an iterative coupled fluid/thermal approach. *Journal of thermophysics and Heat Transfer*, 15(2):129–139, 2001. 29

[66] Jean Lachaud, T. Magin, Ioana Cozmuta, and Nagi Mansour. A short review of ablative-material response models and simulation tools. pages 90–, 08 2011. 27

[67] Jean Lachaud, Tom van Eekelen, James B Scoggins, Thierry E Magin, and Nagi N Mansour. Detailed chemical equilibrium model for porous ablative materials. *International Journal of Heat and Mass Transfer*, 90:1034–1045, 2015. 30

[68] Bernard Laub and Ethiraj Venkatapathy. Thermal protection system technology and facility needs for demanding future planetary missions. In *Planetary Probe Atmospheric Entry and Descent Trajectory Analysis and Science*, volume 544, pages 239–247, 2004. 2

[69] Ivett Leyva. The relentless pursuit of hypersonic flight. *Physics today*, 70(11):30–36, 2017. 3

[70] Leslie M Mack. Boundary-layer linear stability theory. Technical report, California Inst of Tech Pasadena Jet Propulsion Lab, 1984. 6

[71] Matthew MacLean, Jochen Marschall, and David Driver. Finite-rate surface chemistry model, ii: Coupling to viscous Navier-Stokes code. In *42nd AIAA Thermophysics Conference*, page 3784, 2011. 8

[72] Thierry E Magin and Gérard Degrez. Transport algorithms for partially ionized and unmagnetized plasmas. *Journal of Computational Physics*, 198(2):424–449, 2004. 22, 23

[73] Thierry E Magin, Lise Caillault, Anne Bourdon, and CO Laux. Nonequilibrium radiative heat flux modeling for the Huygens entry probe. *Journal of Geophysical Research: Planets*, 111(E7), 2006. 7

[74] Thierry E Magin, Marco Panesi, Anne Bourdon, Richard L Jaffe, and David W Schwenke. Coarse-grain model for internal energy excitation and dissociation of molecular nitrogen. *Chemical Physics*, 398:90–95, 2012. 27

[75] Brian Maicke and Joseph Majdalani. Evaluation of CFD codes for hypersonic flow modeling. In *46th AIAA/ASME/SAE/ASEE Joint Propulsion Conference & Exhibit*, page 7184, 2010. 7

[76] Paul V Marrone and Charles E Treanor. Chemical relaxation with preferential dissociation from excited vibrational levels. *The Physics of Fluids*, 6(9):1215–1221, 1963. 27

[77] Alexandre Martin and Iain Boyd. Strongly coupled computation of material response and nonequilibrium flow for hypersonic ablation. In *41st AIAA Thermophysics Conference*, page 3597, 2009. 8, 29

[78] Alexandre Martin and Iain D Boyd. Strongly coupled computation of material response and nonequilibrium flow for hypersonic ablation. *Journal of Spacecraft and Rockets*, 52(1):89–104, 2014. 29

[79] Alexandre Martin and Iain D Boyd. Modeling of heat transfer attenuation by ablative gases during the Stardust reentry. *Journal of Thermophysics and Heat Transfer*, 29(3):450–466, 2015. 8

[80] Alexandre Martin, Leonardo C Scalabrin, and Iain D Boyd. High performance modeling of atmospheric re-entry vehicles. In *Journal of Physics: Conference Series*, volume 341, page 012002. IOP Publishing, 2012. 7, 8

[81] Jan Matheis and Stefan Hickel. Multi-component vapor-liquid equilibrium model for LES of high-pressure fuel injection and application to ECN spray A. *International Journal of Multiphase Flow*, 99:294–311, 2018. 34, 69

[82] Bonnie J McBride, Michael J Zehe, and Sanford Gordon. Nasa glenn coefficients for calculating thermodynamic properties of individual species. 2002. 19

[83] Michael Meyer, A Devesa, Stefan Hickel, XY Hu, and Nikolaus A Adams. A conservative immersed interface method for large-eddy simulation of incompressible flows. *Journal of Computational Physics*, 229(18):6300–6317, 2010. 36

[84] Frank S Milos and Yih-Kanq Chen. Ablation and thermal response property model validation for phenolic impregnated carbon ablator. *Journal of Spacecraft and Rockets*, 47(5):786–805, 2010. 29

[85] Frank S Milos and Daniel J Rasky. Review of numerical procedures for computational surface thermochemistry. *Journal of thermophysics and heat transfer*, 8(1):24–34, 1994. 28, 31

[86] Fernando Miró-Miró, Ethan S Beyak, Daniel Mullen, Fabio Pinna, and Helen L Reed. Ionization and dissociation effects on hypersonic boundary-layer stability. In *31st Congress of the International Council of the Aeronautical Sciences, Belo Horizonte, Brazil*, 2018. 6

[87] Fernando Miró-Miró, Ethan S Beyak, Fabio Pinna, and Helen L Reed. High-enthalpy models for boundary-layer stability and transition. *Physics of Fluids*, 31(4):044101, 2019. 6, 21, 22, 23

[88] Rajat Mittal and Gianluca Iaccarino. Immersed boundary methods. *Annu. Rev. Fluid Mech.*, 37: 239–261, 2005. 35

[89] Rajat Mittal, Haibo Dong, Meliha Bozkurttas, FM Najjar, Abel Vargas, and Alfred Von Loebbecke. A versatile sharp interface immersed boundary method for incompressible flows with complex boundaries. *Journal of computational physics*, 227(10):4825–4852, 2008. 38

[90] Clifton H Mortensen and Xiaolin Zhong. Simulation of second-mode instability in a real-gas hypersonic flow with graphite ablation. *AIAA journal*, 52(8):1632–1652, 2014. 6, 9, 63

[91] Clifton H Mortensen and Xiaolin Zhong. Real-gas and surface-ablation effects on hypersonic boundary-layer instability over a blunt cone. *AIAA Journal*, 54(3):980–998, 2016. 9, 29

[92] H Müller, CA Niedermeier, M Jarczyk, M Pfitzner, S Hickel, and NA Adams. Large-eddy simulation of trans-and supercritical injection. *Progress in Propulsion Physics*, 8:5–24, 2016. 34

[93] A Munafo, Y Liu, and Marco Panesi. Modeling of dissociation and energy transfer in shock-heated nitrogen flows. *Physics of Fluids*, 27(12):127101, 2015. 27

[94] David Olynick, Y-K Chen, and Michael E Tauber. Aerothermodynamics of the Stardust sample return capsule. *Journal of Spacecraft and Rockets*, 36(3):442–462, 1999. 83, 85

[95] Felix Örley. *Numerical Simulation of Cavitating Flows in Diesel Injection Systems*. PhD thesis, Technische Universität München, 2016. xiii, 37

[96] Felix Örley, Vito Pasquariello, Stefan Hickel, and Nikolaus A Adams. Cut-element based immersed boundary method for moving geometries in compressible liquid flows with cavitation. *Journal of Computational Physics*, 283:1–22, 2015. 35, 37, 41

[97] Grant E Palmer and Michael J Wright. Comparison of methods to compute high-temperature gas viscosity. *Journal of Thermophysics and Heat Transfer*, 17(2):232–239, 2003. 23

[98] Marco Panesi, A Munafò, TE Magin, and RL Jaffe. Nonequilibrium shock-heated nitrogen flows using a rovibrational state-to-state method. *Physical Review E*, 90(1):013009, 2014. 27

[99] Chul Park. Effects of atomic oxygen on graphite ablation. *AIAA journal*, 14(11):1640–1642, 1976. 29

[100] Chul Park. *Nonequilibrium hypersonic aerothermodynamics*. 1989. 7, 8, 9, 26, 45, 64

[101] Chul Park. Review of chemical-kinetic problems of future nasa missions. i-earth entries. *Journal of Thermophysics and Heat transfer*, 7(3):385–398, 1993. 45, 54, 57, 83, 84

[102] Chul Park. Calculation of stagnation-point heating rates associated with stardust vehicle. *Journal of Spacecraft and Rockets*, 44(1):24–32, 2007. 63

[103] Chul Park. The limits of two-temperature kinetic model in air. In *48th AIAA Aerospace Sciences Meeting Including the New Horizons Forum and Aerospace Exposition*, page 911, 2010. 27

[104] Chul Park, Richard L Jaffe, and Harry Partridge. Chemical-kinetic parameters of hyperbolic earth entry. *Journal of Thermophysics and Heat transfer*, 15(1):76–90, 2001. 83, 84

[105] Vito Pasquariello, Georg Hammerl, Felix Örley, Stefan Hickel, Caroline Danowski, Alexander Popp, Wolfgang A Wall, and Nikolaus A Adams. A cut-cell finite volume–finite element coupling approach for fluid–structure interaction in compressible flow. *Journal of Computational Physics*, 307:670–695, 2016. 37, 38, 41

[106] Vito Pasquariello, Stefan Hickel, and Nikolaus A Adams. Unsteady effects of strong shock-wave/boundary-layer interaction at high reynolds number. *J. Fluid Mech*, 823(617):014602–19, 2017. 34

[107] Charles S Peskin. Flow patterns around heart valves: a numerical method. *Journal of computational physics*, 10(2):252–271, 1972. 35

[108] G Pinaud, AJ Van Eekelen, and JM Bouilly. Aerofast: development of cork TPS material and a 3d comparative thermal/ablation analysis of an Apollo & a biconic sled shape for an aerocapture mission. *IPPWC8, June*, 2011. 5

[109] G Pinaud et al. ExoMars 2016: A preliminary post-flight study of the entry module heat shield interactions with the Martian atmosphere. In *15th IPPW conference, Boulder, Colorado, US*, 2018. xiii, 4

[110] Daniel Potter. Modelling of radiating shock layers for atmospheric entry at earth and mars. *Scientaa AC Abore, s4029188 phD Thesis*, pages 48–82, 2011. xiii, 5

[111] Christopher J Roy and Frederick G Blottner. Review and assessment of turbulence models for hypersonic flows. *Progress in Aerospace Sciences*, 42(7-8):469–530, 2006. 7, 9

[112] Isil Sakraker, Ertan Umit, Thorsten Scholz, Paride Testani, Gilles Baillet, and Vincent Van der Haegen. Qarman: An atmospheric entry experiment on cubesat platform. In *8th European Conference on Aerothermodynamics for Space Vehicles*, pages 2–5, 2015. 2, 5

[113] Giovanni Salazar, Jack R Edwards, and Adam J Amar. Large eddy/Reynolds-averaged Navier-Stokes simulations of CUBRC base heating experiments. 2012. 10

[114] Leonardo Scalabrin and Iain Boyd. Development of an unstructured Navier-Stokes solver for hypersonic nonequilibrium aerothermodynamics. In *38th AIAA Thermophysics Conference*, page 5203, 2005. 8, 23

[115] Steven P Schneider. Laminar-turbulent transition on reentry capsules and planetary probes. *Journal of Spacecraft and Rockets*, 43(6):1153–1173, 2006. 6

[116] Pierre Schrooyen. *Numerical simulation of aerothermal flows through ablative thermal protection systems*. PhD thesis, Université Catholique de Louvain, 2015. 10, 11, 22, 29

[117] James B Scoggins. *Development of numerical methods and study of coupled flow, radiation, and ablation phenomena for atmospheric entry*. PhD thesis, Université Paris-Saclay and VKI, 2017. xiii, 2, 3, 4, 19, 21, 22, 23, 25, 26, 27, 28

[118] James B Scoggins and Thierry E Magin. Development of Mutation++: Multicomponent thermodynamic and transport properties for ionized plasmas written in C++. In *11th AIAA/ASME joint thermophysics and heat transfer conference*, page 2966, 2014. 11

[119] James B Scoggins, Jason Rabinovitch, Benjamin Barros-Fernandez, Alexandre Martin, Jean Lachaud, Richard L Jaffe, Nagi N Mansour, Guillaume Blanquart, and Thierry E Magin. Thermodynamic properties of carbon–phenolic gas mixtures. *Aerospace Science and Technology*, 66: 177–192, 2017. 19

[120] James B Scoggins, Vincent Leroy, Georgios Bellas-Chatzigeorgis, Bruno Dias, and Thierry E Magin. Mutation++: Multicomponent thermodynamic and transport properties for ionized gases in C++. *arXiv preprint arXiv:2002.01783*, 2020. 11, 40

[121] Susheel Kumar Sekhar. *Viscous hypersonic flow physics predictions using unstructured Cartesian grid techniques*. PhD thesis, Georgia Institute of Technology, 2012. 39, 43, 44, 50

[122] Susheel Kumar Sekhar and Stephen M Ruffin. Predictions of convective heat transfer rates using a Cartesian grid solver for hypersonic flows. In *44th AIAA Thermophysics Conference*, page 2645, 2013. 45, 50

[123] Chi-Wang Shu. High order weighted essentially nonoscillatory schemes for convection dominated problems. *SIAM review*, 51(1):82–126, 2009. 34

[124] Philippe R Spalart. Detached-eddy simulation. *Annual review of fluid mechanics*, 41:181–202, 2009. 10

[125] Gilbert Strang. On the construction and comparison of difference schemes. *SIAM journal on numerical analysis*, 5(3):506–517, 1968. 34

[126] Kenneth Sutton and Peter Gnoffo. Multi-component diffusion with application to computational aerothermodynamics. In *7th AIAA/ASME Joint Thermophysics and Heat Transfer Conference*, page 2575, 1998. 21, 22

[127] Eleuterio F Toro. *Riemann solvers and numerical methods for fluid dynamics: a practical introduction*. Springer Science & Business Media, 2013. 34

[128] Yu-Heng Tseng and Joel H Ferziger. A ghost-cell immersed boundary method for flow in complex geometry. *Journal of computational physics*, 192(2):593–623, 2003. 35

[129] Alessandro Turchi. *A gas-surface interaction model for the numerical study of rocket nozzle flows over pyrolyzing ablative materials*. PhD thesis, Von Karman Institute for Fluid Dynamics, 2013. xiii, 30, 31, 32

[130] HS Udaykumar, R Mittal, P Rampunggoon, and A Khanna. A sharp interface Cartesian grid method for simulating flows with complex moving boundaries. *Journal of Computational Physics*, 174(1):345–380, 2001. 35

[131] Ethiraj Venkatapathy, Kenneth Hamm, Ian Fernandez, James Arnold, David Kinney, Bernard Laub, Alberto Makino, Mary McGuire, Keith Peterson, Dinesh Prabhu, et al. Adaptive deployable entry and placement technology (ADEPT): a feasibility study for human missions to Mars. In *21st AIAA Aerodynamic Decelerator Systems Technology Conference and Seminar*, page 2608, 2011. 2

[132] Gerard L Vignoles, Jean Lachaud, Yvan Aspa, and Jean-Marc Goyhénèche. Ablation of carbon-based materials: multiscale roughness modelling. *Composites Science and Technology*, 69(9): 1470–1477, 2009. 6

[133] WG Vincenti and Ch H Kruger. Introduction to physical gas dynamics. *John Wlley & Sons*, 1965. 18, 19, 25

[134] CR Wilke. A viscosity equation for gas mixtures. *The journal of chemical physics*, 18(4):517–519, 1950. 23, 54, 63

[135] Adam Wise, Dinesh K Prabhu, Christopher O Johnston, David A Saunders, and Karl T Edquist. Computational aerothermodynamic environments for the Mars 2020 entry capsule. In *2018 Joint Thermophysics and Heat Transfer Conference*, page 3116, 2018. 8

[136] MR Wool. Passive nosetip technology (PANT) program. Technical report, Acurex corp/Aerotherm Mountain View CA, 1975. 6

[137] Michael J Wright, Graham V Candler, and Deepak Bose. Data-parallel line relaxation method for the Navier-Stokes equations. *AIAA journal*, 36(9):1603–1609, 1998. 7

[138] Michael J Wright, Todd White, and Nancy Mangini. Data parallel line relaxation (DPLR) code user manual: Acadia-version 4.01. 1. 2009. 7

[139] Tao Ye, Rajat Mittal, HS Udaykumar, and Wei Shyy. An accurate Cartesian grid method for viscous incompressible flows with complex immersed boundaries. *Journal of computational physics*, 156(2):209–240, 1999. 35

[140] Sergey V Zhluktov and Takashi Abe. Viscous shock-layer simulation of airflow past ablating blunt body with carbon surface. *Journal of Thermophysics and Heat Transfer*, 13(1):50–59, 1999. 8, 29, 63

[141] Xiaolin Zhong and Xiaowen Wang. Direct numerical simulation on the receptivity, instability, and transition of hypersonic boundary layers. *Annual Review of Fluid Mechanics*, 44:527–561, 2012. 9